DETERMINATION OF BIOPHYSICAL AND CHEMICAL PROPERTIES OF SHORT-CHAIN MOLECULES AND BIOLOGICAL NANOPARTICLES

by

Vasiliy Sergeyevich Chernyshev

A dissertation submitted to the faculty of
The University of Utah
in partial fulfillment of the requirements for the degree of

Doctor of Philosophy

Department of Chemical Engineering

The University of Utah

August 2015

The University of Utah Graduate School

STATEMENT OF DISSERTATION APPROVAL

The dissertation of **Vasiliy Sergeyevich Chernyshev**

has been approved by the following supervisory committee members:

Mikhail Skliar	, Chair	**5/18/15** Date Approved
Marc Porter	, Member	**5/14/15** Date Approved
Jules Magda	, Member	**5/14/15** Date Approved
Jennifer Shumaker-Parry	, Member	**5/14/15** Date Approved
Agnes Ostafin	, Member	**5/14/15** Date Approved

and by **Milind Deo** , Chair/Dean of

the Department/College/School of **Chemical Engineering**

and by David B. Kieda, Dean of The Graduate School.

ABSTRACT

Knowledge of physical and chemical properties such as size, diffusivity, concentration and stability of an analyte in a sample is critical in science and engineering. When working in a small size range (0.1-100 nm), which includes short-chain molecules (e.g., ethanol) and nanoparticles, the number of methods that can be used for their characterization becomes sparse and each one has its limitation such as accuracy, resolution, cost of instrumentation and time needed for sample preparation and analysis which introduces more complexity to the problem being solved. This became the motivation and focus of the presented work.

The goal of the conducted research was to explore the available methods as well as develop new methods that can be used for characterization of different analytes. The first half of the dissertation introduces the use of interfacial tension for estimating stability of nanobubbles that can be applied as contrast agents for ultrasound imaging or as vehicles for drug delivery. Use of interfacial tension is then shown to be applicable in a new setup and conditions to determine the diffusion coefficient and concentration of an analyte in any given location. Adsorption of perfluorocarbon vapor to the water surface is then explored.

The second half of the dissertation focuses on characterization of endogenous nanovesicles called exosomes. This section continues the first section by presenting a novel finding of surface activity of exosomes which provides a potential mechanism of

their adsorption to the cell membrane as well as application of dynamic interfacial tension for measuring exosome concentration in a sample. This section continues by comparing techniques that were previously used by others to determine size and shape of exosomes but were not compared to each other either due to unavailability of instrumentation or focus of the study being unrelated to size and shape. This study not only allowed examining the advantages and disadvantages of each technique but also lead to new findings about the biophysical properties of exosomes. This section ends with an application of quartz crystal microbalance method for measuring average mass and concentration of exosomes in a sample.

TABLE OF CONTENTS

LIST OF TABLES

NOMENCLATURE

22Rv1 = Human prostate cancer cell line

AFM = Atomic force microscopy

ATP = Adenosine triphosphate

CBC = Complete blood count

CD = Cluster of differentiation

CD63 = Human protein encoded by CD63 gene

cryoTEM = Cryogenic transmission electron microscopy

CT = Computed tomography

CTC = Circulating tumor cells

D = Diffusion coefficient

DI water = Deionized water

DLS = Dynamic light scattering

DMA = Differential mobility analyzer

DNA = Deoxyribonucleic acid

DNA = Deoxyribonucleic acid

DST = Dynamic surface tension

E_{ads} = Adsorption energy

$E_{barrier}$ = Adsorption potential barrier

ELISA = Enzyme-linked immunosorbent assay

EM = Electron microscopy

ESEM = Environmental scanning electron microscopy

EV = Extracellular vesicles

FasL = Fas ligand

FFF = Field flow fractionation

FT-IR = Fourier transform infrared spectrometer

HER2 = Human epidermal growth factor receptor 2

Hsp = Heat shock proteins

ICAM-1 = Intercellular adhesion molecule 1

IgG = Immunoglobulin G

k_a = Adsorption constant

k_B = Boltzmann's constant

LAMP1/2 = Lysosomal-associated membrane protein 1 and 2

LBPA = Lysobisphosphatidic acid

LNCap = Human prostate cancer cell line

MCF10a = Human breast cancer cell line

MCF7 = Human breast cancer cell line

MDA-MB-231 = Human breast cancer cell line

MHC = Major histocompatibility complex

microRNA = Small non-coding RNA molecule

miRNA = MicroRNA

MRI = Magnetic resonance imaging

mRNA = Messenger ribonucleic acid

MV = Microvesicles

MVB = Multivesicular bodies

N_A = Avogadro's number

NTA = Nanoparticle tracking analysis

PBS = Phosphate buffered saline

PC3 = Human prostate cancer cell line

PCR = Polymerase chain reaction

PCS = Human prostate cancer cell line

PD-1L = Programmed cell death 1 ligand

PDCD6IP = Programmed cell death 6 interacting protein

PFC = Perfluorocarbon

PFH = Perfluorohexane

PFP = Perfluoropentane

QCM = Quartz crystal microbalance

r = Radius of a spherical particle

RNA = Ribonucleic acid

SD = Standard deviation

SEC = Size exclusion chromatography

SEM = Scanning electron microscopy

SLNs = Surface-active lipid nanoparticles

T = Temperature

t = Time

TEM = Transmission electron microscopy

TRPS = Tunable resistive pulse sensing

Tsg101 = Tumor susceptibility gene 101

αvβ6 = Epithelial-specific integrin

Γ = Surface concentration

η = Dynamic viscosity

γ = Surface tension

θ = Surface coverage

ACKNOWLEDGEMENTS

Five years have passed since I started the Ph.D. program in chemical engineering at the University of Utah. This program was not an easy journey and required a lot of energy and patience. In addition to education I was involved in community work in Salt Lake City by volunteering for the Big Brothers Big Sisters organization, St. Marks hospital and University of Utah hospital. This experience along with great support from my family and friends allowed me to overcome the obstacles I faced throughout these five years.

Most importantly, I would like to thank my adviser, Professor Mikhail Skliar, for all his ideas, advice and support throughout the program and I hope I have met his expectations. I really hope to collaborate with him and Dr. Bernard in the future. I would like to thank Dr. Jules Magda for his support and advice on projects I worked on and greatly thank Dr. Marc Porter for allowing me to use his laboratory and instrumentation for my research as well as his recommendations on what I need to focus on the most. Last but not least, I thank Dr. Shumaker-Parry and Dr. Ostafin for being involved in my committee, giving their advice and letting me use their instruments.

I would also like to thank my friends and coworkers, Dr. Seunghey Cho, Yunlu Jia, Rakesh Rachamadugu, Inge Stijleman, Samer Hakami, Soheyl Tadjiki, Kyle Branch, China Ye-Ling Lim, Jooneon Park and Jason Beck, for their help and support.

CHAPTER 1

INTRODUCTION

1.1 Motivation

The motivation for the research presented is the limited amount of available methods that can be used to characterize analytes with small size range, more specifically nanoparticles and short-chain molecules. This initiated the study of advantages and disadvantages of existing methods and development of new methods.

Merriam-Webster dictionary defines analyte as a "chemical substance that is the subject of chemical analysis." This definition includes analytes that start with the smallest 0.074 nm bond length molecule of diatomic hydrogen and continue with particles in a broad size range. Analyte characterization involves determination of its specific feature or property. Properties of an analyte are usually divided into physical and chemical. Physical properties include density, viscosity, volume, area, hardness, elasticity, absorption – process of atoms, molecules or particles entering the bulk phase which can be gas, liquid or solid; and adsorption – adhesion of atoms, molecules or particles from a gas, liquid or dissolved solid to a surface. Chemical properties include chemical stability in a given environment, toxicity, heat of combustion, enthalpy of formation and others. Such properties are of high importance in all areas of science and engineering. For example, mass density of proteins is a useful input parameter for determination of their

three-dimensional structure using protein crystallography and studies of protein oligomers in solution.[1] Another example is the importance of knowing polymeric drug-loaded nanoparticle size for enhancing the ability of the nanoparticle to reach the target and the difficulties in determination of particle size distribution in such small scale.[2] Ability to measure indoor turbulent diffusion coefficient of air polluting emissions is useful for determining exposures in a closed environment such as naturally ventilated residences.[3] Colloidal stability is an example of a chemical property that is critical to prevent particle aggregation and for instance to ensure optimal drug release.[4] More examples can be easily provided to show the high importance of knowing physical and chemical properties of the analyte in question.

This dissertation is focused on the characterization of short-chain molecules, nanobubbles and biological nanoparticles. More specifically, introduction of developed methods for measuring nanobubble stability, measurement of diffusion coefficient of short-chain molecules followed by determination of size, concentration and mass of endogenous nanovesicles called exosomes will be covered. The methods introduced here can potentially be applied for not only the studied analytes but also expanded to a broader range of applications. The background and literature review will be focused on cancer, potential application of exosomes for screening and showing limitations of their characterization.

1.2 Background and Literature Review

1.2.1 Current Methods for Cancer Diagnosis

Cancer is defined as a disease where some of the cells in the body begin to divide without stopping, causing tumor formation (leukemia being an exception), and spread

into other tissues leading to formation of solid tumors in a location away from the original tumor.[5] These types of tumors that invade nearby tissues are called malignant. Tumors that do not spread into or invade nearby tissues are called benign and although most of these tumors can be removed and are not considered to be life threating, benign brain tumor is a clear exception.[5] Cancer that has spread from the location where it started to another location in the body is called metastatic cancer. Metastasis usually involves numerous steps such as local invasion, intravasation – invasion of cancer cells through walls of nearby lymph vessels or blood vessels, circulation – movement through lymphatic system and bloodstream, arrest and extravasation, proliferation and angiogenesis – growth of new blood vessels. Such metastasis eventually leads to severe damage of tissues and organ function and is often fatal. Cancer is a leading cause of deaths in the United States (574,743 deaths in 2010), only slightly surpassed by heart disease (597,689 deaths in 2010).[6] Cancer can arise in many different forms, afflicting all types of tissues and organ systems. It is a progressive disease, diagnosed in stages 1-4. Stage 4 is the most life-threatening with multiple organ systems infiltrated by cancerous cells commonly referred to as "metastasis." Once this state is reached treatment is less effective and the disease is usually terminal. Due to the complexity of metastasis, diagnosing a patient at the earliest stage of their cancer is the best solution, but remains an elusive challenge. Modern cancer research prioritizes early detection above all other mechanisms to fight this disease. Figure 1.1 depicts the trends of cancer incidence and mortality rates by gender over the past thirty-five years.[7] While the incidence of cancer in both male and female continue to grow, there is a clear decrease in mortality rates which can be attributed to advances in medicine and technology. These rates will soon plateau

without more sensitive and accurate early diagnostic techniques. There are more than 100 types of cancer but in this dissertation the focus will only be on two types: breast and prostate cancer.

Breast cancer is currently one of the most studied, contributing 14% of all new cancer cases and 6.8% of all cancer deaths.[8] Figure 1.2 shows the number of breast cancer cases and deaths in the United States collected since 1975. Although there is a noticeable decline from 1990 to 2011, the slope of this decline is clearly small. Mammography is currently the main imaging technique used for breast cancer screening and it is likely the cause of decreasing breast cancer mortality. However, this technique was recently found to cause overdiagnosis (i.e., cancer that is asymptomatic and poses no threat to a woman's life) leading to unnecessary treatment also called "overtreatment" and bringing adverse effects associated with cancer therapy.[9] This technique also can lead to false-positive results where mammograms are found to be abnormal while no cancer is present and similarly to overdiagnosis leading to overtreatment. Adding ultrasound with potential application of nanobubbles for higher resolution and magnetic resonance imaging (MRI) in the hope to improve screening was also found to result in more false-positive findings.[10] Finally, a false negative result is the case where breast cancer is present but mammograms appear normal. Another disadvantage of mammography can also be a potential cause of cancer due to repeated x-ray exposure. Thermography is another method that was considered as an alternative to mammography but was concluded to be unreliable.[11,12]

Prostate cancer is another form of cancer that affects males and contributes 14% of all new cancer cases and 5% of all cancer deaths. Figure 1.3 shows the number of

prostate cancer cases and deaths in the United States since 1975. Prostate-specific antigen (PSA) and digital rectal examination (DRE) are the only two options that were considered to be used for diagnosis. Currently there is no sufficient evidence that such screening methods reduce prostate cancer mortality. Overtreatment due to these two techniques is common and leads to side effects such as erectile dysfunction due to urinary incontinence.[13,14] Such overtreatment includes aggressive procedures in older men considered to be at low risk for progression of the disease.[15] There are current developments of new methods such as examination of DNA in circulating tumor cells (CTCs) in the blood in hope to improve cancer diagnosis and detection of cancer recurrence, but it is unlikely to be important in early cancer detection.

1.2.2 Introduction to Exosomes

An ideal cancer screening should be low cost, routine, minimally invasive and able to diagnose a patient in the earliest stage where no symptoms are present and progression does not take place. The analysis of secretome, totality of secreted organic molecules or particles and inorganic elements, in biological fluids has a potential to enable such screening. Nanoscale extracellular vesicles commonly referred to as exosomes, shedding vesicles, endogenous nanoparticles or extracellular vesicles (EV), is a component of cell secretome with significant diagnostic and drug delivery potential. They are a type of stable nanovesicle (20-120 nm) that transports molecules and other cellular constituents through the bloodstream. They are formed in the late endosomal compartment and generated by inward budding of the limiting membrane of multivesicular bodies (MVBs). This ensures that membrane-bound proteins originally being part of the cell membrane preserve the same orientation and folding on the

exosomal membrane as those on the plasma membrane (Figure 1.4).[16,17] The composition of exosomes includes a plasma membrane that encapsulates cargo material (including nucleic acids and proteins) as well as mRNA, microRNA and DNA originating from the parent cell.[18–21] Figure 1.5 shows a schematic of an exosome and provides examples of its contents.

Many cell types are known to release exosomes, including epithelial cells, mesenchymal cells, lymphocytes, and tumor cells.[22,23] They can be isolated from body fluids (including blood, urine, and saliva) and cell culture supernatant by several methods, including ultracentrifugation,[24] solvent precipitation kits such as ExoQuick,[25] size exclusion chromatography,[26] immunoaffinity isolation (e.g., magnetic Dynabeads and affinity chromatography), "salting-out" procedure and microfluidic techniques.[27–29] The exosomes can be differentiated from other circulating particles (such as small vesicles budded directly from the cell surface) by their formation during the MVB excretion pathway and the range of their sizes (see Figure 1.4). Because of their unique characteristics including their surface decoration and content which is a signature of the mother cell, exosomes have the potential to be perfect cancer markers.

Although our understanding of physiological functions of exosomes is incomplete, they have been shown to be important in modulating immune response and play a role in short and long-range intercellular signaling.[30–32] It has been also shown that exosomes carry small noncoding RNAs and the majority of microRNAs (miRNAs) in circulation are exosome-bound.[33] Therefore, one likely mechanism for cell communication is through exosomes fusing with recipient cells and releasing small RNA and other molecular content inherited from the cell of origin.[34]

Abundance and composition of exosomal miRNA differ with cell types[35,36] and between healthy individuals and those with cancer.[37–39] Other molecular content inherited from a parent, and thus variable with the cell type, includes membrane phospholipids, various proteins[40] (such as tetraspanins and phospholipases), and saccharide groups found on membrane surfaces. For example, it was reported that exosomes released by a HER2-positive breast cancer cells express a full-length HER2 transmembrane protein molecules.[41] The relative abundance of different compounds in exosomes may not be proportional to the cells that produced them. For example, the exosomes of T, B and dendritic immune cells contain only a subset of parent miRNAs.[42]

There is evidence that exosomes are actively secreted in response to environmental conditions (such as hypoxia and lower pH) and other factors, rather than passively shed by cells.[43,44] Cargo selectivity that changes the relative abundance of molecular compounds in exosomes in response to different factors is another manifestation of active secretion. For example, the exosomes of cisplatin-resistant ovarian carcinoma cells[45] have been shown to contain 2.6-fold more platinum in the presence of this drug than cisplatin-sensitive cells. This suggests that drug resistance in this case is associated with the selective ability to actively expel cisplatin in exosomes by cells that possess this defensive mechanism. Another example of a defensive function of exosomes is their contribution to protecting tumor cells by playing a role of decoys for monoclonal antibody therapeutics. Specifically, it was suggested that HER2-positive exosomes may become targets for Trastuzumab treatment thus limiting the availability of this monoclonal antibody to interfere with the HER2/neu receptors of HER2-positive breast cells.[41] The active secretion may also have an offensive function by which the

uptake of tumor exosomes by normal cells leads to a cancerous change in their phenotype[46] and metastases at distant sites. The exosomal mechanism of intercellular signaling may also play a role in modulating immune response by allowing tumor cells to evade immune detection and in tumor dormancy. To disrupt offensive functions of tumor exosomes, it was suggested that extracorporeal hemofiltration of exosomes out of circulation may be an effective adjuvant strategy.[47]

The summarized evidence suggests that the molecular cargo of exosomes is parent-cell dependent and actively modulated in response to different factors. It is not known if biophysical properties of exosomes are equally variable with the origin, environmental, and other factors. Specifically, little is known about the exosome size, density, concentration and content as a function of their origin, though preliminary data indicate that size is a possible differentiator of tumor exosomes from normal exosomes,[48] an observation similar to one reported by Sharma et al.[49] So far there are no reports using the size difference of normal and tumor exosomes to fractionate and enrich the sample in the exosome population of interest.

1.3 Current Exosome Sizing Methods

Unlike molecular analysis that can rely on established molecular and immunolabeling techniques, the characterization of biophysical properties of exosomes, such as their density[50] and elasticity,[51,52] are often carried out on unique instruments or require specialized analytical expertise that is not widely available. Even the measurement of the most basic biophysical property, the exosome size distribution, is a difficult task.[53,54] There are relatively few applicable characterization techniques that can be used to size these nanoscale particles. The exosome sizes overlap with other biological

particles (e.g., lipoprotein and protein agglomerates at the lower range of sizes and larger extracellular microvesicles (MV) and cell debris at the high end of the exosome size distribution), which interfere with the exosome sizing[55] and produce the results that depend on the sample preparation steps. Different techniques estimate sizes based on dissimilar physical principles and thus provide method-dependent sizing.

The hydrodynamic size of a particle is obtained by first estimating its diffusivity in the solution and then calculating its diameter using the Einstein's theory of diffusion to match the observed value. Viscosity and temperature of the solution influence the calculations and must be known or measured. If we ignore the contribution of solvation layer formed around particles due to changes in hydrogen bonding of water molecules at the particle-solvent interface,[56,57] the hydrodynamic and geometric sizes will be equal for smooth, hard, electrically neutral, spherical particles with zero surface charges. Several of these assumptions fail in the case of exosomes, which are elastic particles known to have a strongly negatively charge[58] and molecularly decorated surface. In an aqueous medium, any particle with a surface charge is surrounded by an electrical double layer, sometime referred to as ionic atmosphere.[59] As the particle moves, the ionic atmosphere moves with it, making an apparent particle's size larger than its physical size. The thickness of the ionic atmosphere is approximately equal to the Debye length, which depends on two additional properties of the solution – its ionic strength and the dielectric permittivity.

The molecular decoration of the particle surface is yet another factor with strong influence on the diffusivity. Molecular decoration can impede the motion of particles, decreasing the apparent diffusivity, thus increasing the estimated hydrodynamic size. To

complicate matters further, the surface brush configuration may change with the surface concentration of the decorating molecules, the ionic strength of the solution and its pH.[59]

In view of the discussed factors, it is clear that the hydrodynamic size of particles will always be larger than their geometric size, though the degree of the deviation has not yet been explored. The specifics of different analytical techniques may further contribute to size differences. The following brief discussion of analytical techniques gives an overview of the methods that can be used to estimate the size of exosomes.

1.3.1 Hydrodynamic Size Measurement

Nanoparticle tracking analysis (NTA)[21,60] has emerged as the most widely used method for characterizing the size distribution of exosomes. NTA estimates hydrodynamic size individually for each particle in the field of view of the instrument. The measured particle displacement over time is used to calculate its diffusivity and the hydrodynamic particle size that matches the observed mobility is calculated from the Stokes-Einstein equation:

$$D = \frac{k_B T}{6\pi\eta r} \tag{1}$$

where k_B is the Boltzmann's constant, D is the diffusion coefficient, T is temperature, η is dynamic viscosity and r is the radius of the spherical particle. However, NTA fits a model and produces a size distribution based on only 30-100 particle data providing only estimations. NTA can also produce an inaccurate size distribution when particles such as exosomes, with refractive index close to water or phosphate buffered saline (PBS) are being analyzed.[61]

The dynamic light scattering (DLS) is another commonly used method for estimating the size distribution of exosomes based on their mobility in the solution. Unlike, the NTA that calculates diffusivity individually of each particle, the DLS[62] (also known as photon correlation spectroscopy) is an ensemble technique that estimates the hydrodynamic size distribution of the entire particle population by analyzing the temporal variation in the intensity of the scattered light measured at a fixed scattering angle. Briefly, because the Brownian motion of larger particles in the solution is relatively slow, the corresponding temporal change in the measured intensity of the scattered laser light is also slow. On this basis, the particle diffusivity can be estimated and the corresponding hydrodynamic diameter found from Stokes-Einstein equation. However, for samples with a broad particle size distribution (polydispersed mixture) and mixtures of multiple narrowly distributed fractions (multimodal distribution), the interpretation of temporal fluctuations in intensity becomes difficult and does not produce accurately resolved size histograms. Furthermore, in this situation the DLS results tend to be biased towards larger particle sizes because the scattered intensity changes as sixth power of the particle diameter.

Finally, flow cytometry is another laser-based method to determine size where particles are carried to the laser intercept in a fluid stream. When particles pass through such intercept, they scatter laser light. After collection of the scattered light using lenses, a combination of beam splitters and filters direct scattered light to the appropriate detector. Scattered light data are then converted to size data. However, it was estimated that the minimum detectable exosome size using flow cytometry is 150-190 nm showing that this method is not suitable for exosomes sample analysis.[63]

1.3.2 Volumetric Size Measurement

Exosomes are too small to be characterized by the traditional Coulter counters which size particles based on the measurements of ionic current in electrolyte solution flowing through a microchannel. With recent advances in fabrication of nanopores,[64] however, the sizing of the exosomes[65] and other nanoparticles[66] using this technique becomes possible. The fluid flow created by ionic current driven by a voltage applied across the nanopore (perhaps with the contribution of the pressure driven flow) entrains the particles and carries them through the nanopore. The each passing particle partially obstructs the pore, causing the decrease in the measured ionic current (thus an alternative name of the technique – the resistive pulse measurements, RPM). The magnitude of the current reduction depends on the volume of the solution containing freely moving ions displaced in the pore by the passing particle. For smooth, hard, electrically neutral spheres with undecorated surfaces, the displaced solution is proportion to the 3rd power of the particle diameter, *d*. Several of these conditions might not hold for exosomes. For example, the ions within exosome ionic atmosphere are not moving freely, thus increasing the exclusion volume of freely moving ions. The molecular decoration of exosome surfaces is another factor that may impede ions from freely moving in the proximity of exosomes. So far it has been shown that RPM give size distribution close to that obtained from NTA.[67] This similarity should be carefully judged since the current commercially available RPM have the smallest limit to be ~70 nm so it the similarity of RPM and NTA can be deceiving. According to qNano training guide, RPM measures the geometric size of particles and not hydrodynamic. In addition to its minimum particle diameter limit (~70 nm) another limitation of RPM is its small dynamic range. Particles

larger than the pore size cannot be sized, while particles smaller than ~1/4 of the pore diameter may not create significant reduction in ionic current to be detected. To overcome this limitation, multiple nanopores of different sizes may be used after an initially broad particle population is first fractionated into appropriately narrow size fractions. A recently introduced alternative is to use a tunable pore in an elastic membrane, with the size adjustable by stretching.[68] However, due to the lowest detectable diameter of RPM being 70nm, it is still uncertain if RPM provides the complete spectrum of size distribution. This brings a question whether RPM is reliable due to the possibility of not including exosomes with size being below the limit of detection.

1.3.3 Geometric Size Measurement of Exosomes

1.3.3.1 Desiccated Samples

Too small for light microscopy, the direct imaging of exosomes is achieved with electron microscopy (EM). The traditional implementations of the EM (scanning electron microscopy (SEM) and transmission electron microscopy (TEM)) image samples in vacuum and therefore produce images of desiccated exosomes. Prior to imaging, the sample must be prepared and handled in a way that avoids crystal formation during desiccation, for example, by using an aqueous buffer of a volatile salt (such as ammonium acetate). In TEM, electrons transmitted through a thin sample create a two-dimension projection of 3D samples. If needed, TEM can also be done in tomographic mode to obtain a 3D image. The sample area imaged with high-resolution TEM is small. Therefore, a large number of TEM images are often needed to robustly characterize the exosome size distribution, which makes this technique time consuming and expensive.

Perhaps, this is the reason it is not common to see the size distribution of exosomes obtained by the TEM, often only a range of particle sizes being reported.

Unlike the TEM that captures the cross-sectional projections, the scanning microscopy characterizes the surface of the sample by imaging backscattered and secondary electrons produced by the interaction of an electron beam with the surface. By scanning the beam, a large area of the sample can be imaged, but with a lower resolution than achievable with the transmission microscopy. Once acquired, the TEM or SEM images may be used to obtain the size distribution of exosomes by manual sizing of the visualized nanovesicles or by automated image analysis using software tools, such as ImageJ.[69]

1.3.3.2 Hydrated Samples

Desiccation of biological samples introduces severe environmental transformations, while a change in interfacial forces during desiccation likely alters the geometric sizes of exosomes enveloped with an elastic membrane.[52] Very few methods exist that can be used to characterize geometric sizes of hydrated exosomes, of which the cryoTEM[70] is the gold standard. Prior to imaging, a thin sample of hydrated exosomes, obtained by blotting off the excess solution pipetted on the TEM grid, is plunged into liquid ethane. The rapid cooling is needed to obtain the vitrified (amorphous) form of ice, which has properties similar to liquid water. The exosomes preserved in their native hydrated state are then imaged in high vacuum. The verification increases the tolerance of the samples to high-energy electron irradiation needed for high resolution imaging. With higher radiation tolerance, the sample can be imaged multiple times at different tilt angles and its three-dimensional topography reconstructed using computer tomography.[71] A

notable disadvantage of the cryoTEM imaging, other than the complexity of the sample preparation, is a relatively small number of exosomes in each acquired image. Consequently, a larger number of images must be acquired and analyzed to obtain statistically significant characterization of the exosome size distribution. Image analysis, manual or using software tools, depends on the particle edge detection. The soft membrane of the exosome appears as a diffused boundary in cryoTEM images, which requires a subjective judgment on the edge location during manual sizing or algorithm tuning (e.g., threshold selection) when an automated image analysis is used.

Another microscope that can be used to image hydrated samples is the atomic force microscope (AFM) mainly consisting of a cantilever with a tip, laser, photodiode and detector with feedback electronics. When the cantilever tip is brought close to the sample surface, the forces between the tip and the sample cause deflection of the cantilever according to Hook's law.[72] Such forces can be due to van der Waals forces, chemical bonding, capillary forces, electrostatic forces and others. A laser is used to measure the deflection by tracking the reflected laser from the cantilever using an array of photodiodes. There are numerous variations of AFM that can be adjusted to the sample in question. AFM can be used to image immobilized particles in liquid. Although exosomes were previously imaged using AFM, it was mostly done in dry state.[73,74] Up to now there was only one attempt to characterize exosomes in the liquid by using AFM.[75]

1.4 Concentration Measurement of Exosomes

Only a few techniques are currently available for measuring exosome concentration. We found that available ELISA assays often give inconsistent results because the expression of markers, such as CD63, CD9 and CD81, differs greatly

between patient samples. NTA is currently the most widely used approach for measuring concentration of exosomes in a given sample. However, a narrow field of view implemented in NTA instruments and specific range of particles in that area (only 30 to 100 particles) recommended by the manufacturer make the NTA concentration measurements dependent on the sample preparation steps and the concentration reports being based on a relatively small number of particles. In contrast when compared to ELISA assay, NTA may overestimate the concentration of exosomes due to presence of background particles. Solvent (water or PBS) itself may contain particles that may skew the results obtained by the NTA. Use of the Coulter counter, described previously as a technique for size measurements, is also a method that can be used to measure particle concentration. This technique is based on particle-by-particle counting and makes a concentration estimate based on a larger number of particles when compared to NTA (500 vs 100). However, the Coulter counter can produce misleading results due to aggregates or other large particles inhibiting continuous flow of the exosomes through the nanopore. Similar to the NTA method, Coulter is not specific and may include particles that are not exosomes in the calculation. The experience with Coulter counter, NTA and ELISA exosome concentration measurements done by numerous groups is consistent with observations by Duijvesz et al. that counting exosomes in a sample still remains a challenge.[76] Furthermore, there are currently no verified protocols for standardization of serum and other biofluid samples. Without such standardization concentration of exosomes from the same individual would change with such factors as hydration level.

1.5 Mass/Density Measurement of Exosomes

Consistent with the view that exosomes play a role in long-range intercellular signaling, the exosome weight/density should reflect the amount of encapsulated biomolecular cargo that is likely to be different in cancer and normal exosomes. Although the density has been shown to be an important biophysical property of cells, essentially nothing is known about the difference in densities of normal and tumor exosomes.[77] Only a few general reports about density of exosomes and exosome-like vesicles can be found.[50,78,79] The most common method used to estimate exosome density is the sucrose gradient method where exosomes are layered on top of a sucrose gradient with density ranging 1.12-1.25 and centrifuged for a period of time. Fractions are then collected and the sucrose content is measured with a refractometer providing the relative density.[80] Such method requires high gravitation forces and centrifugation time longer than 12 hours. Since exosomes were shown to be highly time-sensitive, the sucrose gradient method can introduce a substantial error that can affect the conclusions obtained from the results.[81]

1.6 Dissertation Overview and Novelty

It can be seen that characterization on nanoscale is limited to only a few techniques which became the motivation of the presented research. The main goal was to explore available methods and develop novel methods that can be used to characterize short-chain molecules and nanoparticles. More specifically, the dissertation first concentrates on expanding the application of the dynamic interfacial tension method for characterization of short-chain molecules, nanobubbles and biological nanoparticles. The study then continues by comparing the available methods for size and shape

determination on nanoscale and presentation of a new method to measure mass and concentration of biological nanoparticles.

First, application of dynamic interfacial tension will be covered in Chapter 2 through Chapter 5. Surface tension or interfacial tension of a gas/liquid or liquid/liquid system is defined as the excess stress of the surface that is integrated over the interfacial zone.[83] Surfactants, amphiphiles, lipids and proteins are known to cause a decrease in the equilibrium surface tension usually due to minimization of Gibbs free energy with the molecular mechanisms including hydrophobic effect, electrostatic attraction and stereospecific or other binding.[84] This portion of the dissertation focuses on expanding the applications of dynamic interfacial tension method. Up to this day surface tension was mostly applied to characterize surfactants that are present in the liquid phase. This classical problem was first presented by Dr. Milner at the beginning of the 1900s who hypothesized that surface tension changes with time due to migration of the surfactant to the interface.[85] However, to our knowledge there are no studies that look at the effect of vapor of one compound on the surface tension of another. Chapter 2 presents the application of dynamic surface tension to estimate stability of nanobubbles by exposing water and methanol to perfluorocarbon vapors. This study finds a linear relation between concentration of perfluorocarbon in the vapor and surface tension of water and methanol liquid which was not shown before. Chapter 3 shows application of this relation for development of a new method for determination of the diffusion coefficient of short-chain molecules in the vapor phase. The algorithm of this method can be generalized and applied not only to vapor/liquid but also for liquid/liquid systems where diffusion coefficients of short-chain molecules, nanobubbles and nanoparticles can be determined.

Chapter 4 explores adsorption of perfluorocarbon vapor on the water surface which causes a change in surface tension in more detail.

As previously discussed, exosome composition includes lipids and proteins that are known to be surface active which may cause a change in interfacial tension. Chapter 5 becomes a continuation of Chapters 2-4 by presenting the finding that exosomes are surface active and proposes application of the dynamic interfacial tension technique for determination of exosome concentration in a sample. It also provides an insight on the mechanism of exosome adsorption to the cell membrane.

Characterization of exosomes becomes a challenge due to their size (20-120 nm), elasticity and time-sensitivity. The amount of available methods for size measurements is sparse and no detailed comparison of these methods is available up to this day. It is critical to know the advantages and disadvantages of each method as well as what useful information each method is able to provide in order to make reliable and useful conclusions from experimental data. Chapter 6 compares methods available today that can be used to determine the size and/or shape of exosomes and introduces a new protocol for exosome analysis when using atomic force microscopy.

In addition to the limited number of methods available for size and shape determination of exosomes, there are only a handful of methods able to determine mass of exosomes and other nanoparticles which may allow discriminate different populations. Quartz crystal microbalance (QCM) is a method that can be used to measure the change in mass per unit area by using frequency change of a quartz crystal resonator. The field of QCM gained momentum in 1950s when the sensitivity of this method was found to be substantial. This method later became a common sensor for mass and viscosity change.[82]

Up to now, to our knowledge, there is no application of this method for determination of exosome mass. Chapter 7 will introduce the QCM method and its application for exosome characterization. Finally, conclusions and direction of future research will be discussed in Chapter 8.

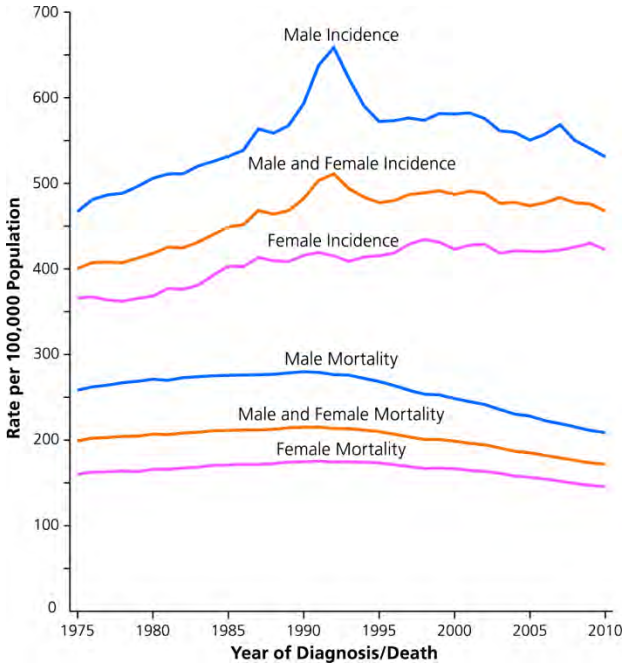

Figure 1.1: Cancer incidence and mortality from 1975 to 2010. Figure adapted from.[7]

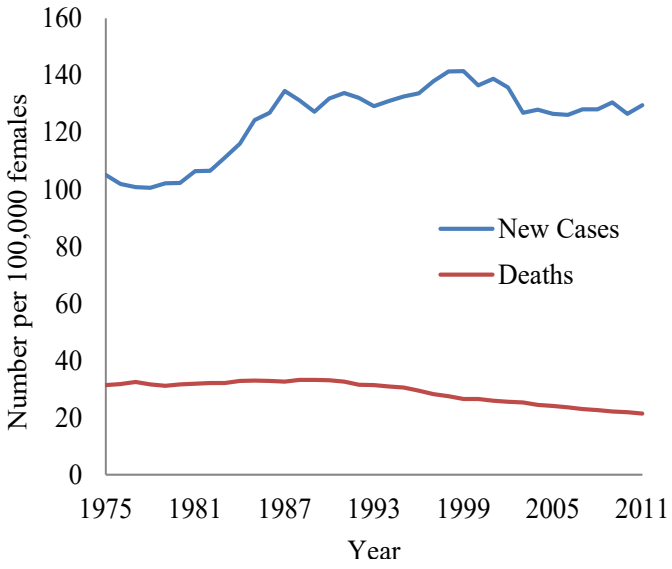

Figure 1.2: Breast cancer new cases and deaths from 1975 to 2011. Data adapted from.[8]

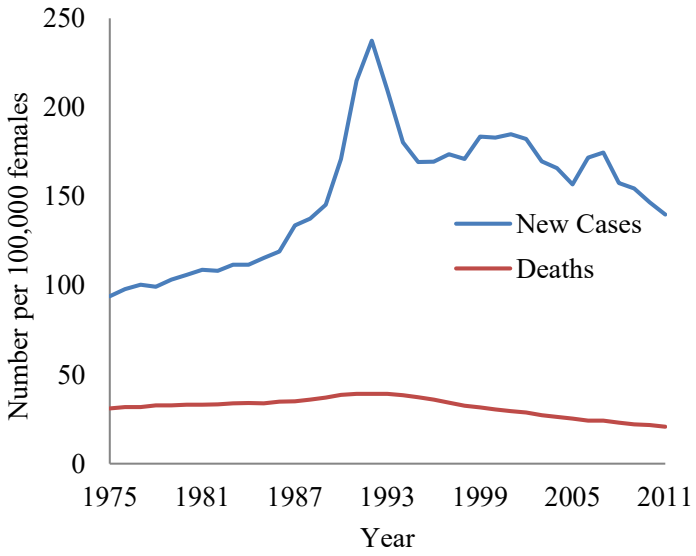

Figure 1.3: Prostate cancer new cases and deaths from 1975 to 2011. Data adapted from.[8]

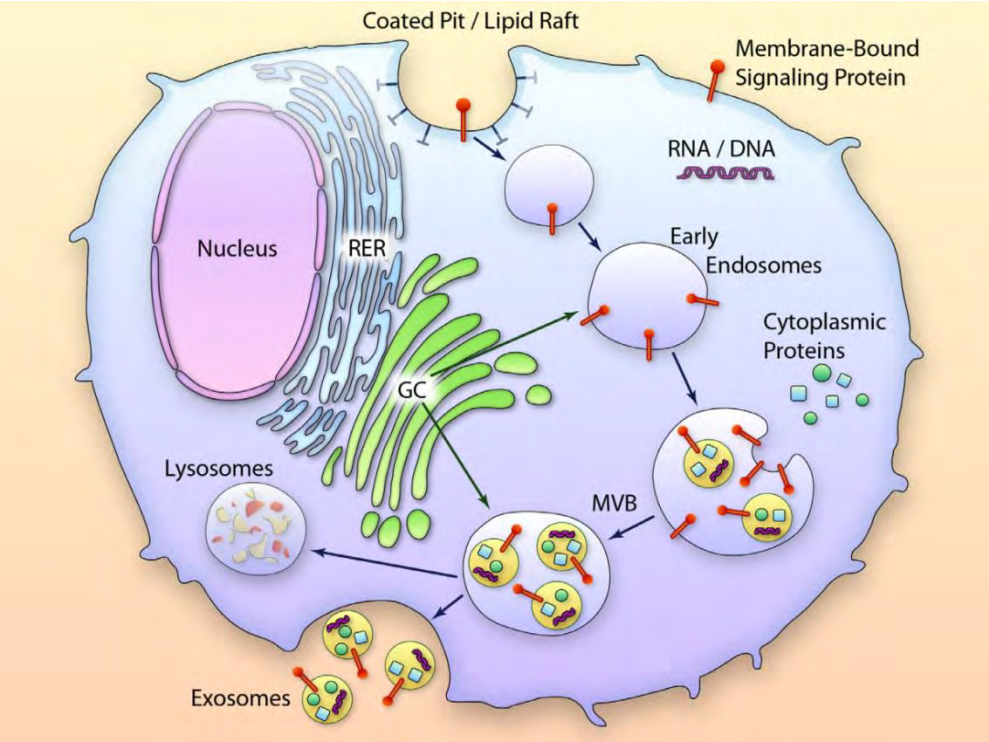

Figure 1.4: Schematic shows the hypothesized development of exosomes in a cell an excretion to the extracellular space. Figure adapted from.[16]

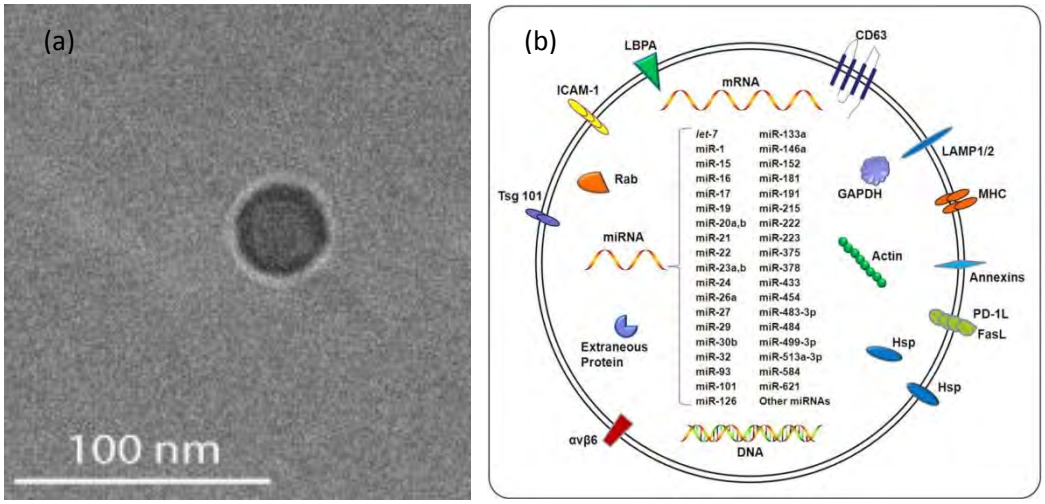

Figure 1.5: Shape, size and composition of exosomes (a) Cryo-TEM image of an exosome. (b) Schematic of an exosome. The circular lines forming the circle represent an exosome membrane that is adapted from the cell of origin. Adapted from.[16]

1.7 References

1. Fischer, H., Polikarpov, I. & Craievich, A. F. Average protein density is a molecular-weight-dependent function. *Protein Sci.* **13,** 2825–2828 (2004).

2. Gaumet, M., Vargas, A., Gurny, R. & Delie, F. Nanoparticles for drug delivery: the need for precision in reporting particle size parameters. *Eur. J. Pharm. Biopharm.* **69,** 1–9 (2008).

3. Cheng, K. C. *et al.* Modeling exposure close to air pollution sources in naturally ventilated residences: association of turbulent diffusion coefficient with air change rate. *Environ. Sci. Technol.* **45,** 4016–4022 (2011).

4. Dakwar, G. R. *et al.* Colloidal stability of nano-sized particles in the peritoneal fluid: towards optimizing drug delivery systems for intraperitoneal therapy. *Acta Biomater.* **10,** 2965–2975 (2014).

5. National Cancer Institute at the National Institute of Health. What Is Cancer? Available at: http://www.cancer.gov/cancertopics/what-is-cancer [Accessed March 25, 2015]

6. Center of Disease Control and Prevention. Deaths and Mortality. Available at: http://www.cdc.gov/nchs/fastats/deaths.htm [Accessed March 25, 2015]

7. Siegel, R., Ma, J., Zou, Z. & Jemal, A. Cancer Statistics, 2014. *CA. A Cancer Journal for Clinicians*. **64,** 9–29 (2014).

8. National Cancer Institute at the National Institute of Health. Surveillance, Epidemiology, and End Results Program. Cancer Stat Fact Sheets. Available at: http://seer.cancer.gov/statfacts [Accessed March 25, 2015]

9. National Cancer Institute at the National Institute of Health. Norwegian Study Estimates Overdiagnosis of Breast Cancer from Screening, NCI Cancer Bulletin. Available at: http://www.cancer.gov/cancertopics/pdq/screening/breast/healthprofessional/page8 [Accessed March 25, 2015]

10. National Cancer Institute at the National Institute of Health. Drawbacks of Adding MRI to Mammography Plus Ultrasound May Outweigh Benefits, NCI Cancer Bulletin. Available at: http://www.cancer.gov/cancertopics/pdq/screening/breast/healthprofessional/page1 [Accessed Martch 25, 2015]

11. U.S. Food and Drug Administration. Breast Cancer Screening - Thermograpy Is Not an Alternative to Mammography: FDA Safety Communication Available at:

www.fda.gov/MedicalDevices/Safety/AlertsandNotices/ucm257259.htm [Accessed March 25, 2015].

12. National Cancer Institute at the National Institute of Health. Mammograms. Available at: http://www.cancer.gov/cancertopics/types/breast/mammograms-fact-sheet [Accessed March 25, 2015]

13. Harris, R. & Lohr, K. N. Screening for prostate cancer: an update of the evidence for the U.S. Preventive Services Task Force. *Ann. Intern. Med.* **137,** 917–929 (2002).

14. Steineck Gunnar, Helgesen Fred, Adolfsson Jan, Dickman Paul W., Johansson Jan-Erik, Norlén Bo Johan, H. L. Quality of life after radical prostatectomy or watchful waiting. *N. Engl. J. Med.* **169,** 790–796 (2002).

15. National Cancer Institute at the National Institute of Health. PSA Screening Leads to Aggressive Treatment, Even in Older Men at Low Risk, NCI Cancer Bulletin. Available at: http://www.cancer.gov/cancertopics/treatment/prostate/overtreatment0710 [Accessed March 25, 2015]

16. Waldenström, A. & Ronquist, G. Role of exosomes in myocardial remodeling. *Circ. Res.* **114,** 315–324 (2014).

17. Thery, C., Zitvogel, L. & Amigorena, S. Exosomes: composition, biogenesis and function. *Nat. Rev. Immunol.* **2,** 569–579 (2002).

18. Kharaziha, P., Ceder, S., Li, Q. & Panaretakis, T. Tumor cell-derived exosomes: a message in a bottle. *Biochim. Biophys. Acta.* **1826,** 103–111 (2012).

19. Raposo, G. & Stoorvogel, W. Extracellular vesicles: exosomes, microvesicles, and friends. *J. Cell. Biol.* **200,** 373–383 (2013).

20. Simons, M. & Raposo, G. Exosomes--vesicular carriers for intercellular communication. *Curr. Opin. Cell Biol.* **21,** 575–81 (2009).

21. Vlassov, A. V., Magdaleno, S., Setterquist, R. & Conrad, R. Exosomes: current knowledge of their composition, biological functions, and diagnostic and therapeutic potentials. *Biochim. Biophys. Acta.* **1820,** 940–8 (2012).

22. Trams, E. G., Lauter, C. J., Salem Jr., N. & Heine, U. Exfoliation of membrane ecto-enzymes in the form of micro-vesicles. *Biochim. Biophys. Acta.* **645,** 63–70 (1981).

23. Palma, J. *et al.* MicroRNAs are exported from malignant cells in customized particles. *Nucleic Acids Res.* **40,** 9125–38 (2012).

24. Théry, C., Amigorena, S., Raposo, G. & Clayton, A. Isolation and characterization of exosomes from cell culture supernatants and biological fluids. *Curr. Protoc. Cell Biol.* **Chapter 3,** Unit 3.22 (2006).

25. Taylor, D. D., Zacharias, W. & Gercel-Taylor, C. Exosome isolation for proteomic analyses and RNA profiling. *Methods Mol. Biol.* **728,** 235–46 (2011).

26. Witwer, K. W. *et al.* Standardization of sample collection, isolation and analysis methods in extracellular vesicle research. *J. Extracell. Vesicles* **2,** 20360 (2013)

27. Chen, C. *et al.* Microfluidic isolation and transcriptome analysis of serum microvesicles. *Lab Chip* **10,** 505–11 (2010).

28. Petersen, K. *et al.* A review of exosome separation techniques and characterization of B16-F10 mouse melanoma exosomes with AF4-UV-MALS-QELS-DLS-TEM. *Anal. Bioanal. Chem.* **406,** 7855-66 (2014).

29. Brownlee, Z., Lynn, K. D., Thorpe, P. E. & Schroit, A. J. A novel 'salting-out' procedure for the isolation of tumor-derived exosomes. *J. Immunol. Methods* **407,** 120-6 (2014).

30. Pucci, F. & Pittet, M. J. Molecular pathways: tumor-derived microvesicles and their interactions with immune cells in vivo. *Clin. Cancer Res.* **19,** 2598–604 (2013).

31. Ge, R., Tan, E., Sharghi-Namini, S. & Asada, H. H. Exosomes in cancer microenvironment and beyond: have we overlooked these extracellular messengers? *Cancer Microenviron.* **5,** 323–332 (2012).

32. Zhang, Y. *et al.* Secreted monocytic miR-150 enhances targeted endothelial cell migration. *Mol. Cell* **39,** 133–44 (2010).

33. Gallo, A., Tandon, M., Alevizos, I. & Illei, G. G. The majority of microRNAs detectable in serum and saliva is concentrated in exosomes. *PLoS One* **7,** e30679 (2012).

34. Regev-Rudzki, N. *et al.* Cell-cell communication between malaria-infected red blood cells via exosome-like vesicles. *Cell* **153,** 1120–33 (2013).

35. Mathivanan, S., Fahner, C. J., Reid, G. E. & Simpson, R. J. ExoCarta 2012: database of exosomal proteins, RNA and lipids. *Nucleic Acids Res.* **40,** D1241–4 (2012).

36. Kalra, H. *et al.* Vesiclepedia: a compendium for extracellular vesicles with continuous community annotation. *PLoS Biol.* **10,** e1001450 (2012).

37. Chen, X. *et al.* Characterization of microRNAs in serum: a novel class of biomarkers for diagnosis of cancer and other diseases. *Cell Res.* **18,** 997–1006 (2008).

38. Taylor, D. D. & Gercel-Taylor, C. MicroRNA signatures of tumor-derived exosomes as diagnostic biomarkers of ovarian cancer. *Gynecol. Oncol.* **110,** 13–21 (2008).

39. Lee, Y. S. & Dutta, A. MicroRNAs in cancer. *Annu. Rev. Pathol.* **4,** 199–227 (2009).

40. Conde-vancells, J., Rodriguez-suarez, E., Embade, N. & Gil, D. Characterization and comprehensive proteome profiling of exosomes secreted by hepatocytes. *J. Proteome Res.* **7,** 5157–5166 (2009).

41. Ciravolo, V. *et al.* Potential role of HER2-overexpressing exosomes in countering trastuzumab-based therapy. *J. Cell. Physiol.* **227,** 658–67 (2012).

42. Mittelbrunn, M. *et al.* Unidirectional transfer of microRNA-loaded exosomes from T cells to antigen-presenting cells. *Nat. Commun.* **2,** 282 (2011).

43. King, H. W., Michael, M. Z. & Gleadle, J. M. Hypoxic enhancement of exosome release by breast cancer cells. *BMC Cancer* **12,** 421 (2012).

44. Kucharzewska, P. & Belting, M. Emerging roles of extracellular vesicles in the adaptive response of tumour cells to microenvironmental stress. *J. Extracell. Vesicles* **2,** 20304 (2013).

45. Safaei, R. *et al.* Abnormal lysosomal trafficking and enhanced exosomal export of cisplatin in drug-resistant human ovarian carcinoma cells. *Mol. Cancer Ther.* **4,** 1595–604 (2005).

46. Ogorevc, E., Kralj-Iglic, V. & Veranic, P. The role of extracellular vesicles in phenotypic cancer transformation. *Radiol. Oncol.* **47,** 197–205 (2013).

47. Marleau, A. M., Chen, C.-S., Joyce, J. A. & Tullis, R. H. Exosome removal as a therapeutic adjuvant in cancer. *J. Transl. Med.* **10,** 134 (2012).

48. Chernyshev, V. *et al.*Size and shape characterization of hydrated and desiccated exosomes. *Anal. Bioanal. Chem.* **407,** 3285-301 (2015).

49. Sharma, S., Gillespie, B. M., Palanisamy, V. & Gimzewski, J. K. Quantitative nanostructural and single-molecule force spectroscopy biomolecular analysis of human-saliva-derived exosomes. *Langmuir* **27,** 14394–400 (2011).

50. Olcum, S. *et al.* Weighing nanoparticles in solution at the attogram scale. *Proc. Natl. Acad. Sci.* **111,** 1310-1315 (2014).

51. Byun, S. *et al.* Characterizing deformability and surface friction of cancer cells. *Proc. Natl. Acad. Sci. U. S. A.* **110,** 7580-7585 (2013).

52. Sharma, S. *et al.* Structural-mechanical characterization of nanoparticle exosomes in human saliva, using correlative AFM, FESEM, and force spectroscopy. *ACS Nano* **4,** 1921–6 (2010).

53. Van der Pol, E., Coumans, F., Varga, Z., Krumrey, M. & Nieuwland, R. Innovation in detection of microparticles and exosomes. *J. Thromb. Haemost.* **11 Suppl 1,** 36–45 (2013).

54. Van der Pol, E. *et al.* Optical and non-optical methods for detection and characterization of microparticles and exosomes. *J. Thromb. Haemost.* **8,** 2596–607 (2010).

55. György, B. *et al.* Detection and isolation of cell-derived microparticles are compromised by protein complexes resulting from shared biophysical parameters. *Blood* **117,** e39–48 (2011).

56. Besseling, N. A. M. Theory of hydration forces between surfaces. *Langmuir* **13,** 2113–2122 (1997).

57. He, L., Hu, Y., Wang, M. & Yin, Y. Determination of solvation layer thickness by a magnetophotonic approach. *ACS Nano* **6,** 4196–202 (2012).

58. Sokolova, V. *et al.* Characterisation of exosomes derived from human cells by nanoparticle tracking analysis and scanning electron microscopy. *Colloids Surf. B. Biointerfaces* **87,** 146–50 (2011).

59. Tathireddy, P., Choi, Y.-H. & Skliar, M. Particle AC electrokinetics in planar interdigitated microelectrode geometry. *J. Electrostat.* **66,** 609–619 (2008).

60. Momen-Heravi, F. *et al.* Impact of biofluid viscosity on size and sedimentation efficiency of the isolated microvesicles. *Front. Physiol.* **3,** 162 (2012).

61. Van der Pol, E., Coumans, F. A. W., Sturk, A., Nieuwland, R. & van Leeuwen, T. G. Refractive index determination of nanoparticles in suspension using nanoparticle tracking analysis. *Nano Lett.* **14,** 6195–201 (2014).

62. Tscharnuter, W. T. in *Encycl. Anal. Chem.* (Meyers, R. A.) 1–16 John Wiley & Sons, Ltd, 2006. doi:10.1002/9780470027318.a1512

63. Van der Pol, E. *et al.* Particle size distribution of exosomes and microvesicles by transmission electron microscopy, flow cytometry, nanoparticle tracking analysis, and resistive pulse sensing. *J. Thromb. Haemost.***12,** 1182-1192 (2014).

64. Li, Y.-Q., Zheng, Y.-B. & Zare, R. N. Electrical, optical, and docking properties of conical nanopores. *ACS Nano* **6,** 993–7 (2012).

65. Ng, Y. H. *et al.* Endometrial exosomes/microvesicles in the uterine microenvironment: a new paradigm for embryo-endometrial cross talk at implantation. *PLoS One* **8,** e58502 (2013).

66. Holden, D. A., Watkins, J. J. & White, H. S. Resistive-pulse detection of multilamellar liposomes. *Langmuir* **28,** 7572–7 (2012).

67. Varga, Z. *et al.* Towards traceable size determination of extracellular vesicles. *J. Extracell. Vesicles* **3,** 23298 (2014).

68. Vogel, R. *et al.* Quantitative sizing of nano/microparticles with a tunable elastomeric pore sensor. *Anal. Chem.* **83,** 3499–506 (2011).

69. Schneider, C. A., Rasband, W. S. & Eliceiri, K. W. NIH Image to ImageJ: 25 years of image analysis. *Nat. Methods* **9,** 671–675 (2012).

70. Frank, J. Single-particle imaging of macromolecules by cryo-electron microscopy. *Annu. Rev. Biophys. Biomol. Struct.* **31,** 303–19 (2002).

71. Nudelman, F., de With, G. & Sommerdijk, N. A. J. M. Cryo-electron tomography: 3-dimensional imaging of soft matter. *Soft Matter* **7,** 17 (2011).

72. Cappella, B. & Dietler, G. Force-distance curves by atomic force microscopy. *Surf. Sci. Rep.* **34,** 1–104 (1999).

73. Sharma, S., Das, K., Woo, J. & Gimzewski, J. K. Nanofilaments on glioblastoma exosomes revealed by peak force microscopy. *J. R. Soc. Interface* **11,** 20131150 (2014).

74. Palanisamy, V. *et al.* Nanostructural and transcriptomic analyses of human saliva derived exosomes. *PLoS One* **5,** e8577 (2010).

75. Hardij, J. *et al.* Characterisation of tissue factor-bearing extracellular vesicles with AFM: comparison of air-tapping-mode AFM and liquid Peak Force AFM. *J. Extracell. Vesicles* **2,** 1–9 (2013).

76. Duijvesz, D., Luider, T., Bangma, C. H. & Jenster, G. Exosomes as biomarker treasure chests for prostate cancer. *Eur. Urol.* **59,** 823–31 (2011).

77. Grover, W. H. *et al.* Measuring single-cell density. *Proc. Natl. Acad. Sci. U. S. A.* **108,** 10992–10996 (2011).

78. Tauro, B. J. *et al.* Comparison of ultracentrifugation, density gradient separation, and immunoaffinity capture methods for isolating human colon cancer cell line LIM1863-derived exosomes. *Methods* **56,** 293–304 (2012).

79. Raposo, G. *et al.* B lymphocytes secrete antigen-presenting vesicles. *J. Exp. Med.* **183,** 1161–72 (1996).

80. Skogberg, G. *et al.* Characterization of human thymic exosomes. *PLoS One* **8,** e67554 (2013).

81. Oosthuyzen, W. *et al.* Quantification of human urinary exosomes by nanoparticle tracking analysis. *J. Physiol.* **591,** 5833–42 (2013).

82. Johannsmann, D. Viscoelastic, mechanical, and dielectric measurements on complex samples with the quartz crystal microbalance. *Phys. Chem. Chem. Phys.* **10,** 4516–4534 (2008).

83. Defay, R., Prigogine, I., Bellemans, A. & Everette, D. H. *Surface Tension and Adsorption* (Longmans, 1966).

84. Franses, E. I., Basaran, O. A. & Chang, C.-H. Techniques to measure dynamic surface tension. *Curr. Opin. Colloid Interface Sci.* **1,** 296–303 (1996).

85. Milner, S. R. On surface concentration, and the formation of liquid films. *Philos. Mag. Ser. 6* **13,** 96–110 (1907).

CHAPTER 2

SURFACE TENSION OF WATER IN THE PRESENCE OF PERFLUOROCARBON VAPORS

[Chernyshev, V.S., Skliar, M. Surface tension of water in the presence of perfluorocarbon vapors. *Soft Matter.* **10**, 1937-1943 (2014)] - Reproduced by permission of The Royal Society of Chemistry
http://pubs.rsc.org/en/Content/ArticleLanding/2014/SM/c3sm52289j#!divAbstract

Soft Matter

PAPER

View Article Online
View Journal | View Issue

Surface tension of water in the presence of perfluorocarbon vapors

Cite this: Soft Matter, 2014, 10, 1937

Vasiliy S. Chernyshev and Mikhail Skliar*

Fluorocarbons are highly hydrophobic, biocompatible compounds with a variety of medical applications. Despite significant interest, the study of interfacial properties of fluorocarbons in aqueous systems has received limited attention. In this study, we investigate the influence of perfluoropentane and perfluorohexane vapors on the surface tension of water at room temperature. The results show a substantial decrease in the surface tension of water in the presence of perfluorocarbon vapors. In the investigated range of partial pressures up to the saturation value, a linear correlation between the surface tension and the partial pressure was found. This suggests that an adsorbed perfluorocarbon layer is formed on the surface of water. For comparison, the effect of the perfluorocarbon vapor on the surface tension of methanol was also investigated and a similar dependence was observed. Our results indicate that the stability and dynamic transitions of fluorocarbon colloids, which may be dispersed under physiological conditions as microdroplets, bubbles, or their combination, are likely affected by the composition of liquid and gas phases.

Received 29th August 2013
Accepted 12th December 2013

DOI: 10.1039/c3sm52289j

www.rsc.org/softmatter

Introduction

Perfluorocarbons (PFCs) have unique properties that have proved to be useful in biomedical applications.[1–3] These compounds are chemically inert[4] and non-toxic.[2,5] Their intermolecular interactions are weak. For example, the surface tension of perfluoropentane (PFP, C_5F_{12}) at 25 °C is only 9.5 mN m^{-1}. When compared to hydrocarbons with the same number of carbon atoms, PFCs are denser and more hydrophobic.[6] A very high gas solubility in perfluorocarbons motivated efforts to design PFC-based blood substitutes for emergency tissue oxygenation.[7,8] Oxygen solubility in PFCs at 37 °C and 1 atm is typically in the range of 40–50% (v/v) depending on the number of carbon atoms[9] compared to 2.5% in water. The solubility of carbon dioxide in different perfluorocarbons varies from 140 to 200% (v/v).[10] For perfluorohexane (PFH, C_6F_{14}), the solubility of oxygen and nitrogen at 25 °C and 1 atm was found to be 65% and 43% (v/v), respectively.[11] The surface tension of PFH at 20 °C is 11.91 mN m^{-1}; only slightly larger than that of PFPs.

Perfluoropentane shares many desirable biocompatibility features with other molecules in the PFC family and is distinguished by having a boiling point slightly above room temperature (~29 °C at sea level). As a result, the dispersed PFP phase at physiological temperature may be present as liquid droplets or bubbles, depending on the particle size and surfactants or other means used to stabilize the suspension.[2] The PFP applications that utilize this combination of properties include the use of perfluoropentane as an ultrasound and MRI contrast agent,[1] blood substitute[5,6] (solubility of oxygen in PFP has been reported to be 80% (v/v) at 25 °C), liquid ventilation,[12] and as a propellant in inhalation drug delivery.[13] Dispersed perfluorocarbon droplets and bubbles have been investigated in drug and gene delivery applications[14,15] and as a means to enhance cavitation during ultrasound tissue ablation.[16,17]

Despite significant interest in PFCs, the investigation of aqueous perfluorocarbon colloids has received limited attention. For PFP aqueous colloids, which under physiological conditions may be dispersed as vapor, liquid, or the combination of the two phases, only the effect of several surfactants on the interfacial tension in the liquid–liquid system was previously studied.[2] In gas–liquid systems, the composition of bubbles formed by phase transition of PFC droplets is uncertain and influenced by the composition of gases originally dissolved into liquid PFC prior to phase transition. The gas composition of liquid PFC droplets itself depends on the composition of gases in the suspending phase which, under physiological conditions in blood and other body fluids, is particularly uncertain, subject-specific, and time-varying.

Water solubility also has an effect on the composition of perfluorocarbon microbubbles. Kabalnov *et al.*[18] reported a very low (4.0×10^{-6} mol l^{-1} or 0.707×10^{-6} mol ml^{-1}) solubility of PFP in water, while Wüstneck *et al.*[19] stated that C_5F_{12} did not show any water solubility. Unlike other gases and vapors investigated by Wüstneck *et al.*, the volume of the PFP bubble grew with time, which was explained by a net transport of gases dissolved in water into the bubble. Though such migration of the water-dissolved gases into the bubble changed the overall

Department of Chemical Engineering, University of Utah, Salt Lake City, UT 84112, USA. E-mail: mikhail.skliar@utah.edu

composition of the gas phase, the surface tension of the water–PFP vapor mixture system remained constant[19] in the reported experiments.

Motivated by the influence the interfacial tension has on the stability of PFC colloids in biomedical applications, this work investigates the effect that partial vapor pressures of perfluoropentane and perfluorohexane have on the interfacial tension of the water–PFC vapor mixture. The results are compared with the influence of the PFC vapor concentration has on the surface energy of methanol, which is another poor solvent of PFP and PFH.

Experimental

Setup

Research grade PFP and PFH were purchased from FluoroMed (Round Rock, TX). PFP in a sealed container was kept in a refrigerator at 1 °C. Sealed containers of PFH, deionized water, and methanol were kept at room temperature (maintained at 20 °C). A custom pendant-drop tensiometer was built to provide the capability for continuous, near real-time surface tension measurements. The apparatus consists of an air-tight cuvette in which a pendant drop of a liquid is introduced. The drop was imaged with a 1024 × 768 pixel resolution camera (Imaging Source, Charlotte, NC) fitted to an objective with an adjustable optical zoom in the range of 6–24× magnification. Typical magnification was 10×, selected to maximize the number of pixels representing the drop in the camera's field of view. The distortion-free imaging was verified by capturing images of the hemocytometer grid.

Custom software, implemented in Matlab (MathWorks, Natick, MA), was developed to capture, preprocess, and analyze images at the rate as high as 15 fps. The actual update rate of the interfacial tension measurements, droplet volume, surface area, and, in the case of sessile drop experiments, the contact angle was ~1.4 seconds, constrained by the time needed to perform the necessary calculation on a particular computer used by us (HP Z400 Workstation). At the preprocessing step, the precise boundary of the pendant droplet was determined by converting a grayscale image into a binary image (see the inset in Fig. 1) using the threshold value calculated following Otsu's method.[20] For each row of pixels, a midpoint between boundary points of the droplet was determined. The position of the vertical centerline that divides the droplet into two symmetrical halves was then obtained by averaging midpoint values obtained for each row of pixels. The end result of the image preprocessing is illustrated in Fig. 1. Here the red line shows the boundary of the droplet obtained from the binary image by connecting boundary pixels with a curve that smoothed their coordinates by averaging nine boundary points in a sliding window. The obtained boundary was then used to calculate the volume and the surface area of the droplet.

When the interfacial tension γ is known, the shape of the pendant drop can be predicted from the balance of gravity and surface tension forces. When tension is unknown, its value can be estimated by finding γ that minimizes the difference between the theoretically predicted and the imaged shape of the interface. Several methods have been developed to obtain

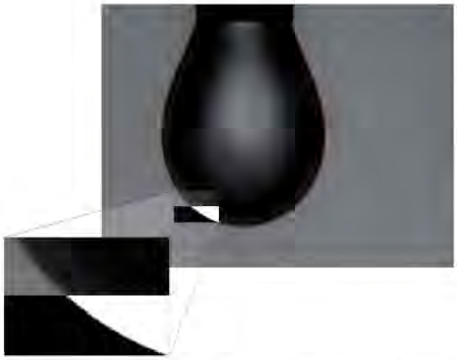

Fig. 1 Image of the water drop captured by the camera. The inset shows the conversion of the captured image into the binary form used to determine the shape of the surface (red line).

the estimate of unknown γ; see, for example, ref. 21–23. The method implemented by us uses the system identification theory[24] to find γ that minimizes the least square errors between the predicted and the imaged shapes of the interface. This new implementation of the method was motivated by the need to rapidly process the acquired images as the concentration of the PFP vapor was changing rapidly during the experiments. Precision of the method was assessed with substances of known surface tension (Table 1). The results show good agreement with the literature values.

Procedure

A pendant drop of DI water was created at the end of a stainless steel syringe needle (1.6/2.09 mm inside/outside diameter) placed inside a sealed cuvette maintained at 20 °C room temperature in the laboratory located ~1470 m above the sea level. The cuvette was saturated with water vapor by allowing time for partial evaporation of the drop, at which point the measured volume of the drop attained the steady state value. As a confirmation that the water vapor–liquid equilibrium was indeed attained, the temperature inside the cuvette was measured using an infrared camera (FLIR Model T300) focused on the drop through a KBr (IR-transparent) window.

After the drop of DI water has thermally equilibrated, we changed the composition of the gas phase inside the cuvette by injecting the liquid form of a studied compound into the cuvette, as illustrated in Fig. 2. The surface tension was

Table 1 Measured and literature values of surface tension

Sample	Measured	Literature
DI water	72.5	72.75 (ref. 21)
1 mM CTAB in DI water	36.9	37 (ref. 25)
Methanol	22.5	22.95 (ref. 26)
Ethanol	22.3	22.31 (ref. 26)

continuously measured as the PFC vapor concentration increased from zero until the PFC liquid–vapor equilibrium was reached.

The concentration of the PFC vapor at the location of the pendant drop was measured by Fourier transform infrared spectroscopy (FTIR) in separate experiments. Before injecting liquid PFC, the laser of the FTIR spectrometer (Nicolet iS10, Thermo Scientific, Waltham, MA) was positioned to traverse the sealed cuvette through two KBr windows at the location where the pendant drop was suspended during surface tension measurements. After injecting 500 μL of liquid PFC, the light absorption, A, at a selected wavenumber (530 cm^{-1}) was continuously recorded. The contribution of the air absorption was subtracted from the measured value and the Beer–Lambert law, given by the following equation,

$$A = \varepsilon l c \quad (1)$$

was applied to obtain the PFC vapor concentration, c, as a function of time at the location of the pendant drop. The coefficient εl was estimated using the measurements of A at equilibrium, for which the vapor concentration was estimated by the Antoine equation with parameters given by Crowder *et al.*[27] The measurements were consistent over three repeat runs, two of which are shown in Fig. 3 for PFP and PFH. The maximum difference between the runs in the measured PFP vapor concentration was 2 mol m^{-3} immediately after injecting the liquid; it remained below 1 mol m^{-3} at all other points. Similarly for PFH, the maximum initial error was 0.61 mol m^{-3} and below 0.5 mol m^{-3} after that. We further estimated that temperature variations within ±1 °C would contribute an error less than ±1.1 and ±0.4 mol m^{-3} to the measurements of the PFP and PFH vapor concentrations, respectively.

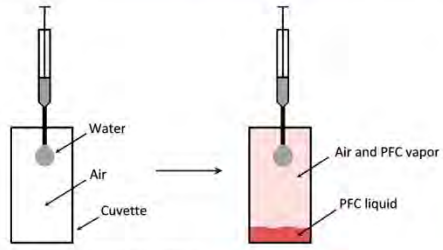

Fig. 2 Experimental procedure.

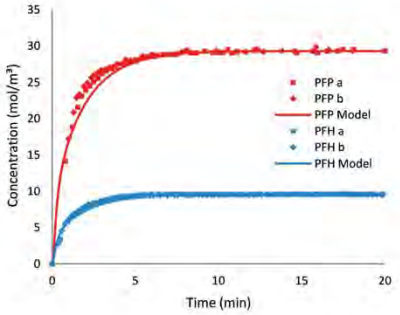

Fig. 3 Measured and model predicted changes in PFP and PFH vapor concentrations at the location of the pendant drop after the injection of the PFC liquid into the cuvette at $t = 0$. The concentration was measured by FTIR spectroscopy (two repeats shown, a & b) and compared with the model predictions (solid lines).

Results and discussion

The temperature of the pendant water drop may be substantially lower than the ambient prior to vapor–liquid equilibration. A thermal image in Fig. 4(a) shows that immediately after the pendant drop was introduced into the sealed cuvette, its surface temperature is several degrees lower than the surrounding temperature. The time needed to achieve thermal equilibrium, imaged in Fig. 4(b), closely agreed with the time needed for the volume of the drop to reach a constant value (Fig. 4(c)), indicating that evaporation is the primary mechanism responsible for temperature variations.

After the temperature and volume equilibration, 500 μL of PFP or PFH was injected into the sealed cuvette. The results of FTIR measurements of the PFC vapor concentration, obtained

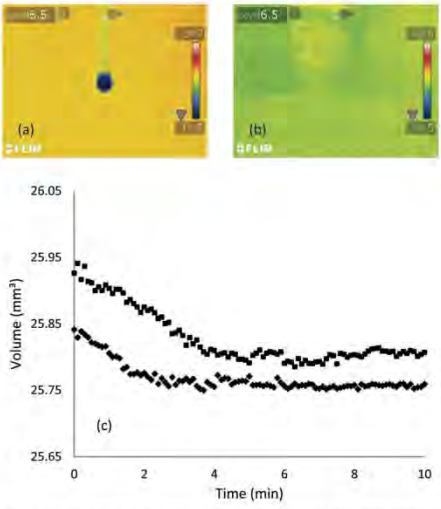

Fig. 4 Prior to achieving vapor–liquid equilibrium, the temperature of the water droplet is noticeably lower than the environment (a). After 5 minutes, the temperature becomes nearly uniform, indicating that the water–vapor equilibrium has been reached (b). The volume of the drop stabilized at a constant value at approximately the same time, as seen in (c) for two typical runs.

under the same conditions but in separate experiments, are shown in Fig. 3. The concentration measurements were compared with the predictions of the PFC concentration at the location of the pendant drop obtained by numerically solving a three-dimensional diffusive mass transport model (solid lines in Fig. 3). The computer simulations used the binary diffusion coefficients of PFC vapors in air given by the Fuller–Schettler–Giddings empirical correlation[28] and equal to 4.96×10^{-6} m^2 s^{-1} and 4.56×10^{-6} m^2 s^{-1} for PFP and PFH, respectively.

Almost immediately after injecting liquid PFC into the sealed cuvette, a steep decline in the surface tension was observed. Fig. 5a shows the measured change in the surface tension of water following the injection of PFP or PFH liquid at 10 min. Each data point in Fig. 5 represents the average of 8 runs for each perfluorocarbon. The data acquisition continued for 30 min until the measured surface tension stabilized around a constant value. The average surface tension of water in the presence of saturated PFP vapor during the last 5 min of experiments was 64.6 mN m^{-1} (10.9% decline from the initial value) with the standard deviation of 0.473 mN m^{-1}. In the case of PFH vapor, the surface tension at the end of the experiments stabilized at 66.7 mN m^{-1} (8% decline) measured with 0.965 mN m^{-1} standard deviation.

A long term behavior of the surface tension during one of the runs is shown in Fig. 6. During this experiment, at $t \approx 30$ min the cuvette was opened to the atmosphere, which allowed for a slow escape of PFP vapor and the eventual return of the surface tension of water to its initial value, γ_0. The transition to γ_0 starts at ~260 min when the last of the liquid PFP has evaporated from the bottom of the cuvette.

Similar experiments were repeated with methanol. Its surface tension at room temperature was found to be 22.5 mN m^{-1}, in agreement with the previously reported result.[36] As in the case of water, it was found that the PFC vapor leads to a considerable reduction in the surface tension of methanol. Fig. 5b shows the change in the surface tension of methanol after the injection of PFP or PFH into the cuvette. For the air saturated with PFP vapor, the surface tension stabilized at

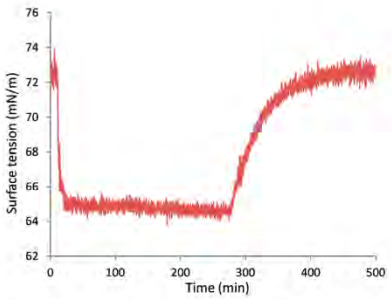

Fig. 6 Surface tension of water is decreased after the introduction of PFP. At ~30 min, the PFP vapor was allowed to slowly escape the cuvette. After the complete evaporation of liquid PFP at ~260 min, the surface tension returned to its initial value.

approximately 17.7 ± 0.390 mN m^{-1} (~21% decline). When the gas phase was saturated with the PFH vapor, the surface tension stabilized at 19.6 mN m^{-1} (12.9% decline) with 0.342 mN m^{-1} standard deviation. Interestingly, the decrease of methanol surface tension in the presence of both PFC vapors is substantially larger in relative terms than in the case of water. Table 2 provides the summary of our findings under the vapor saturation conditions.

The observation that for both water and methanol the end point reduction in surface tension is higher in the presence of

Table 2 Surface tension [mN m^{-1} ± STD] at the liquid interface in the presence of saturated perfluorocarbon vapor

	Liquid	
Vapor	DI water	Methanol
PFP	64.6 ± 0.473	17.7 ± 0.390
PFH	66.7 ± 0.965	19.6 ± 0.342

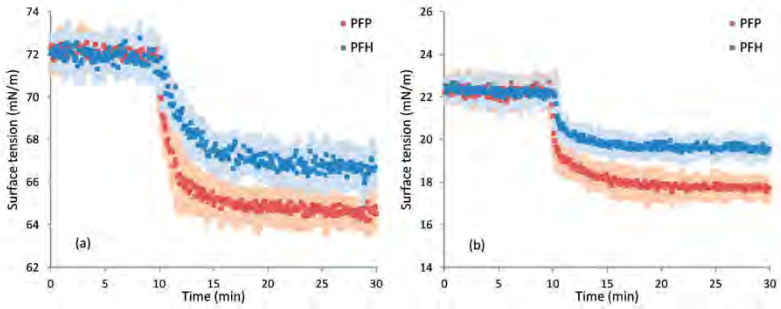

Fig. 5 Surface tension of water (a) and methanol (b) at the interface with the air–perfluorocarbon vapor mixture. The tension measurements were averaged over 8 runs aligned by the time $t = 10$ min when a perfluorocarbon liquid (PFP or PFH) was injected into the cuvette. The shaded area indicates ±standard deviation for each data point.

PFP vapor, which has a higher vapor pressure at saturation (0.863 atm at 25 °C compared to 0.266 atm for PFH), suggests that the surface tension is correlated with the vapor concentration. To investigate this further, we aligned the concentration and the surface tension series of measurements at the instant the liquid perfluorocarbon was injected into the cuvette, which is $t = 0$ in Fig. 3 and $t = 10$ min in Fig. 5. After the alignment, we used the synchronized data points to obtain the dependence of the interfacial tension on the concentration of PFC vapor, with the result shown in Fig. 7. The discrete data points in Fig. 7 (shown with the standard deviation bars) give the measured surface tension corresponding to less frequent measurements of the vapor concentration; their linear regression is shown as black lines.

A relatively slow rate of FTIR measurements limited the number of acquired data points during the rapid change in vapor concentration immediately following the introduction of liquid PFC into the cuvette. In order to take advantage of the available surface tension measurements acquired at a high sampling rate, a three-dimensional diffusive transport model was used to obtain model predictions of the PFP and PFH vapor concentrations at the location of the pendant drop. Solid red and blue curves in Fig. 7 give the measured γ_0 as a function of predicted vapor concentrations.

Fig. 7 shows that the results based on the measured and the model predicted concentrations are in good agreement. Within the range of experimental conditions, the interfacial tension was found to decrease linearly with the vapor concentration of both PFC compounds. This result is in apparent contradiction with prior observation[19] that the surface tension remained constant as gases dissolved in water migrated into the PFP vapor–air bubble, decreasing the PFP vapor concentration inside the bubble.

Table 3 gives the linear regression of the results in Fig. 7 as

$$\gamma = \gamma_0 - b[\mathrm{PFC}]_v \quad (2)$$

where γ_0 is the surface tension at zero PFC vapor concentration and b is the slope of the linear regression.

The observed reduction in the surface tension in the presence of the two considered perfluoroalkanes may be explained by the formation of a PFC layer on the surface of water formed by adsorption of PFC molecules from the gas phase. Using the obtained surface tension *vs.* concentration relationships, the excess film pressure of the adsorption layer is

$$\pi = \gamma_0 - \gamma = b[\mathrm{PFC}]_v \quad (3)$$

where γ, γ_0 and b are listed in Table 3.

The observed linear dependence of the surface tension on the bulk concentration is typical of a Gibbs adsorption monolayer with low surface excess, Γ.[29] According to the Gibbs adsorption isotherm, the excess of perfluorocarbon molecules at the interface can be expressed as

$$\Gamma = -\frac{1}{RT}\frac{\mathrm{d}\gamma}{\mathrm{d}\ln([\mathrm{PFC}]_v)} = \frac{\pi}{RT} \quad (4)$$

where the activity was approximated by the bulk concentration of the perfluorocarbon vapor, $[\mathrm{PFC}]_v$. The interfacial area occupied, on average, by a single perfluorocarbon molecule adsorbed into the PFC layer on the water surface is then simply an inverse of Γ.

The adsorption of highly hydrophobic perfluorocarbon molecules onto the water surface viewed as a mechanism behind the observed reduction in the surface tension, though counter intuitive and not yet supported by the direct measurements of the PFC adsorption layer, is indirectly supported by several studies involving other hydrophobic and water insoluble substances in the vapor phase. For example, neutron and X-ray reflectivity measurements[30] revealed that heptane and octane vapors form continuous layers on the surface of water, less than 50 Å thick. The thermodynamic properties of the *n*-alkane vapor adsorption on the water surface were obtained by Hauxwell *et al.*[31] and Dobbs,[32] and the formation of the alkane layer on the

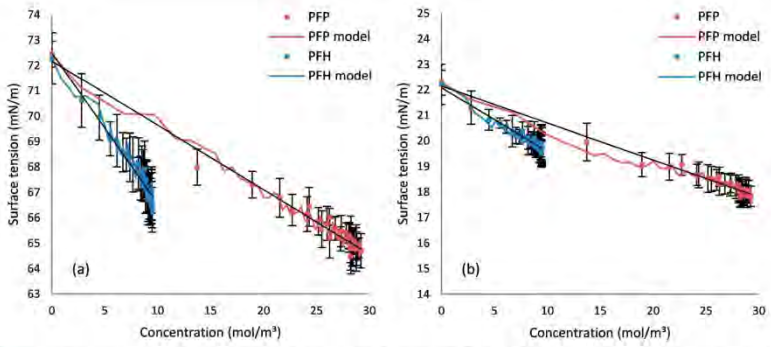

Fig. 7 Surface tension at the water (a) and methanol (b) interfaces as a function of PFP and PFH vapor concentrations. The results obtained with the measured (■ and ■ for PFP and PFH, respectively) and model predicted (solid red and blue lines) vapor concentrations are similar. The depicted linear regression lines (in black) were obtained based on the measured concentrations.

Table 3 Interfacial tension γ (in mN m^{-1}) as a function of PFC vapor concentration (in [mol m^{-3}]) that was either measured (data) or estimated using computer simulations (model)

		Liquid	
Gas		DI water	Methanol
Air–PFP vapor mixture	Data	$\gamma = 72.17 - 0.25[\mathrm{PFP}]_v$ $R^2 = 0.97$	$\gamma = 21.86 - 0.13[\mathrm{PFP}]_v$ $R^2 = 0.92$
	Model	$\gamma = 72.11 - 0.25[\mathrm{PFP}]_v$ $R^2 = 0.99$	$\gamma = 22.25 - 0.15[\mathrm{PFP}]_v$ $R^2 = 0.97$
Air–PFH vapor mixture	Data	$\gamma = 72.67 - 0.62[\mathrm{PFH}]_v$ $R^2 = 0.93$	$\gamma = 21.88 - 0.23[\mathrm{PFH}]_v$ $R^2 = 0.92$
	Model	$\gamma = 72.20 - 0.59[\mathrm{PFH}]_v$ $R^2 = 0.95$	$\gamma = 22.28 - 0.28[\mathrm{PFH}]_v$ $R^2 = 0.95$

surface of aqueous NaCl solution was analyzed[33] as a function of aqueous salinity and temperature. Conversely, an adsorbed layer of water on hydrophobic and superhydrophobic surfaces has also been observed and characterized by surface resistance measurements.[34]

Surface co-adsorption of a non-ionic surfactant from water and the hexane vapor from the gas phase was studied by Fainerman *et al.*[35] The same group has demonstrated that vapor adsorption is significantly enhanced at low surfactant concentrations.[36] It was found that hexane vapor substantially reduced the surface tension at equilibrium compared to the case when only aqueous surfactant (octaethylene glycol monododecyl ether) was used. It is reasonable to expect that the energy of PFC–water interfaces, until now separately investigated for the water–PFC vapor system in this work and previously studied for the liquid–liquid system with aqueous surfactants,[2] may also be affected by co-adsorption of the vapors and aqueous surfactants and their compositions in gas and liquid phases.

Conclusions

In biomedical applications the dispersed fluorocarbons may be suspended in aqueous medium as liquid droplets, vapor bubbles, the combination of the two, and as particles containing both phases simultaneously. Motivated by the interest in understanding the factors influencing the stability of fluorocarbon colloids, this study investigated the effect of perfluorocarbon vapors at different concentrations on the surface tension of water. Two specific perfluoroalkane compounds were considered, PFP and PFH.

Our results indicate that the surface tension of water is significantly affected by the presence and the concentration of perfluorocarbon vapors. It was found that in the range of the investigated partial pressures, the surface tension reduces linearly with the PFC vapor concentration. The likely mechanism of such reduction is the formation of a PFC layer on the water surface due to adsorption of highly hydrophobic and insoluble perfluorocarbon molecules from the gas phase. The surface tension of methanol showed a similar strong dependence on the PFC vapor concentration, suggesting the formation of an adsorbed layer in this case as well. It should be noted that for a given vapor concentration, the methanol's surface energy is lowered by a considerably higher percentage compared to water. At the same time, the adsorption of PFC vapors at the methanol surface is weaker than that at the water surface, as evident from the slopes in Fig. 7 and Table 3.

The surprisingly strong surface activity of the examined vapors must be taken into account when analyzing the stability of fluorocarbon suspensions of droplets and bubbles and their phase transition, and may be relevant to several biomedical applications. Gases dissolved in bodily fluids and migrating into the dispersed fluorocarbon phase may have an effect on the stability of fluorocarbon colloids under physiological conditions. Furthermore, the results of the prior study that examined the surface adsorption of aqueous surfactants and the current results suggest that the combined effect of co-adsorption from liquid and gas phases may be important in such systems.

Acknowledgements

The authors acknowledge support from the National Science Foundation (award number IGERT-0903715) and the U.S. Army Medical Research Grant number W81XWH-10-1-0751.

References

1 R. Díaz-López, N. Tsapis and E. Fattal, *Pharm. Res.*, 2010, **27**, 1–16.
2 M. A. Kandadai, P. Mohan, G. Lin, A. Butterfield, M. Skliar and J. J. Magda, *Langmuir*, 2010, **26**, 4655–4660.
3 J. G. Riess, *J. Fluorine Chem.*, 2002, **114**, 119–126.
4 U. Gross, S. Rüdiger and H. Reichelt, *J. Fluorine Chem.*, 1991, **53**, 155–161.
5 S. F. Flaim, Pharmacokinetics and Side Effects of Perfluorocarbon-Based Blood Substitutes, *Artif. Cells, Blood Substitutes, Immobilization Biotechnol.*, 1994, **22**, 1043–1054.
6 B. D. Spiess, *J. Appl. Physiol.*, 2009, **106**, 1444–1452.
7 V. Centis and P. Vermette, *Front. Biosci.*, 2009, **14**, 665–688.
8 R. W. Millard, *Artif. Cells, Blood Substitutes, Immobilization Biotechnol.*, 1994, **22**, 235–244.
9 K. C. Lowe, *Tissue Eng.*, 2003, **9**, 389–399.
10 J. G. Riess, *Chem. Rev.*, 2001, **101**, 2797–2920.
11 M. W. Grenfell, in *Fluoropolymers 2: Properties*, G. Hougham, P. E. Cassidy, K. Johns and T. Davidson, Kluwer Academic, New York, 2002, pp. 111–120.
12 H.-J. Lehmler, P. M. Bummer and M. Jay, *CHEMTECH*, 1999, **29**, 7–12.

13 S. P. Rocha, B. Bharatwaj, and S. Saiprasad, in *Controlled Pulmonary Drug Delivery SE - 8*, ed. H. D. C. Smyth and A. J. Hickey, Springer, New York, 2011, pp. 165–201.
14 N. Rapoport, Z. Gao and A. Kennedy, *J. Natl. Cancer Inst.*, 2007, **99**, 1095–1106.
15 T. D. Tran, S. D. Caruthers, M. Hughes, J. N. Marsh, T. Cyrus, P. M. Winter, A. M. Neubauer, S. A. Wickline and G. M. Lanza, *Int. J. Nanomed.*, 2007, **2**, 515–526.
16 H.-D. Liang, J. Tang and M. Halliwell, *Proc. Inst. Mech. Eng., Part H*, 2010, **224**, 343–361.
17 D. Arora, M. Skliar and R. B. Roemer, *IEEE Trans. Biomed. Eng.*, 2005, **52**, 191–200.
18 A. S. Kabalnov, K. N. Makarov, O. V. Shcherbakova and A. N. Nesmeyanov, *J. Fluorine Chem.*, 1990, **50**, 271–284.
19 N. Wüstneck, R. Wüstneck, U. Pison and H. Möhwald, *Langmuir*, 2007, **23**, 1815–1823.
20 N. Otsu, *IEEE Trans. Syst., Man, Cybern.*, 1979, **9**, 62–66.
21 M. Hoorfar and A. W. Neumann, *Adv. Colloid Interface Sci.*, 2006, **121**, 25–49.
22 A. F. Stalder, T. Melchior, M. Müller, D. Sage, T. Blu and M. Unser, *Colloids Surf., A*, 2010, **364**, 72–81.
23 A. F. Stalder, G. Kulik, D. Sage, L. Barbieri and P. Hoffmann, *Colloids Surf., A*, 2006, **286**, 92–103.
24 L. Ljung, *System Identification: Theory for the User*, Prentice Hall, 2nd edn, 1999.
25 M. H. Uddin, S. Y. Tan and R. R. Dagastine, *Langmuir*, 2011, **27**, 2536–2544.
26 G. Vazquez, E. Alvarez and J. M. Navaza, *J. Chem. Eng. Data*, 1995, **40**, 611–614.
27 G. A. Crowder, Z. L. Taylor, T. M. Reed and J. A. Young, *J. Chem. Eng. Data*, 1967, **12**, 481–485.
28 R. Taylor and R. Krishna, *Multicomponent Mass Transfer (Wiley Series in Chemical Engineering)*, Wiley-Interscience, 1993.
29 H.-J. Butt, K. Graf and M. Kappl, *Physics and Chemistry of Interfaces*, Wiley, 2013.
30 O.-S. Kwon, H. Jing, K. Shin, X. Wang and S. K. Satija, *Langmuir*, 2007, **23**, 12249–12253.
31 F. Hauxwell, N. R. Pallas and B. A. Pethica, *Langmuir*, 1992, **8**, 602–603.
32 H. Dobbs, *Langmuir*, 2000, **16**, 4749–4751.
33 L. Boinovich and A. Emelyanenko, *Adv. Colloid Interface Sci.*, 2009, **147–148**, 44–55.
34 A. S. Pashinin, A. M. Emel'yanenko and L. B. Boinovich, *Prot. Met. Phys. Chem. Surf.*, 2010, **46**, 734–739.
35 V. B. Fainerman, E. V. Aksenenko, V. I. Kovalchuk, A. Javadi and R. Miller, *Soft Matter*, 2011, **7**, 7860.
36 R. Miller, V. Starov, A. Javadi, N. Moradi, V. B. Fainerman, H. Möhwald and R. Miller, *Colloids Surf., A*, 2011, **391**, 19–24.

CHAPTER 3

DIFFUSIVITY MEASUREMENTS OF SOLUTES IMPACTING INTERFACIAL TENSION

I&EC research
Industrial & Engineering Chemistry Research

Article

pubs.acs.org/IECR

Diffusivity Measurements of Solutes Impacting Interfacial Tension

Vasiliy S. Chernyshev and Mikhail Skliar*

Department of Chemical Engineering, University of Utah, Salt Lake City, Utah 84112, United States

ABSTRACT: We propose a method for measuring gas and liquid diffusivities of surface active solutes based on the measurements of dynamic interfacial tension. The selection of the experimental system needed to achieve accurate diffusivity estimation and, particularly, the selection of the complementary fluid to create the interface sensitive to the solute concentration are emphasized. The method is applicable to solutes beyond traditional liquid-phase surfactants and is demonstrated by estimating diffusivities of several vapors in air. Though the method allows for surface active compounds that traverse the interface, the procedure for estimating diffusion coefficients is particularly simple in cases when the solute is insoluble in the complementary fluid and when its flux across the interface is small. It was shown that by adding surfactants to the complementary fluid, it may be possible to reduce the flux of the solute across the interface by increasing the resistance to cross-interfacial transport and to identify diffusivities with higher accuracy based on simple data analysis. The improved accuracy is also achieved when the diffusivity is identified based on models that, when appropriate, account for the absorption of the solute into the complementary fluid. The developed method is simple, rapid, suitable for many applications, and often can be implemented using only basic laboratory equipment. We discuss its advantages, limitations, and provide user guidelines for its implementation.

INTRODUCTION

Measurement of diffusion coefficient (or diffusivity) is important in characterizing, understanding, and designing mass transfer processes.[1] Currently, available methods are generally divided into theoretical[2] and experimental, with the latter category further subdivided into direct and indirect subtypes. The direct methods measure changes in composition of species with time and use this information to estimate the diffusivity. Such methods tend to be tedious, expensive, and time-consuming. This motivates the search for alternatives,[3] which are often indirect methods that infer the diffusivity from the measurements of more easily accessible properties affected by mass transfer, such as pressure,[4] interface velocity,[5] volume of the diffusing solute,[6] NMR spin echos,[7] and others.[8−10] For instance, by tracking the motion of the interface, the diffusion coefficient of carbon dioxide in crude oil can be obtained.[5] Measurement of pressure at constant volume was used to characterize gas diffusivity into bitumen.[11] Aqueous diffusion coefficients of KCl over a broad range of concentrations were estimated in ref 12 using the measurements of the electrical resistance in an open-ended capillary cell arrangement.[13] Rohling et al. developed an indirect method to determine binary diffusion coefficient of various gases using a photothermal deflection technique.[14] These and other indirect techniques, though often easier to use than direct methods, still generally require specialized instrumentation and considerable time to estimate diffusion coefficients. For example, the density measurements at time intervals of 6, 12, and 24 h were used in ref 15 to determine binary diffusion coefficients of *n*-alkane mixtures in a sliding symmetric tubes apparatus. Furthermore, indirect methods capable of measuring diffusion coefficients in multicomponent vapor and liquid phases remain sparse.

The focus of this paper is on the estimation of diffusivities, particularly in the gas phase, using measurements of dynamic interfacial tension. The idea of using interfacial tension to estimate diffusivities of surface active substances has a long history starting with Milner[16] who suggested that the diffusion of surfactants from the bulk to the interface is responsible for the observed changes in the surface tension with time. The quantitative model for surfactant adsorption at the interface was first proposed by Ward and Tordai[17] and further developed and refined by many authors (see, for example, refs 18−21 and review 22). For the case of the diffusion-controlled adsorption, it was immediately recognized by Ward and Tordai that with the model correlating the interfacial tension (and the corresponding surface concentration) to the bulk concentration of a surfactant in the immediate proximity of the interface it is possible to estimate the surfactant's diffusivity. Over the years, the basic ideas of finding diffusivity of surface active species by minimizing the difference between the measurements of the interfacial tension and the corresponding diffusion-dependent predictions has seen many variations that differ in aspects such as the assumed diffusion-limited adsorption isotherms (e.g., linear,[23] Langmuir,[24] and Freundlich[25] isotherms); the adoption of "mixed-kinetic" adsorption models[26,27] in which the assumption of the instantaneous equilibration between surface and "subsurface" concentrations is relaxed; the development of adsorption kinetics for mixtures of surfactants;[28] the employed surfactant transport models; and in techniques used to measure time-dependent tension of the interface. Almost exclusively, the approach was used to estimate liquid phase diffusivities of surfactants. The consideration of the transport of surface active compounds across the interface is rare. The work of Hansen,[29] who analyzes the impact of the evaporation of a liquid-phase surfactant, and the estimation of the diffusivity of CO_2 in crude oil by Yang and Gu[30] are a few exceptions known to us. Unlike a typical case involving

Special Issue: Scott Fogler Festschrift

Received: November 4, 2014
Revised: January 26, 2015
Accepted: January 27, 2015

DOI: 10.1021/ie504355w
Ind. Eng. Chem. Res. XXXX, XXX, XXX−XXX

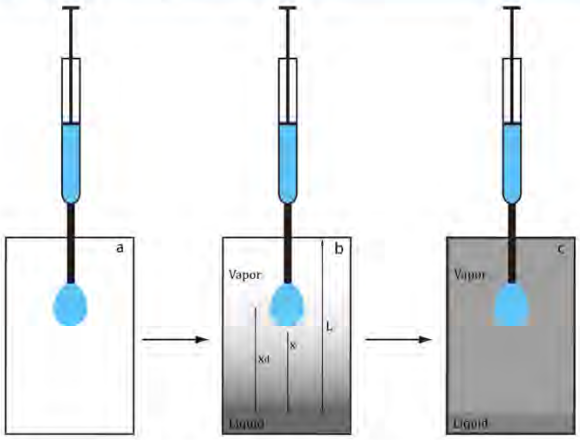

Figure 1. Experimental procedure for measuring surface tension before and after introduction of the vapor. (a) The pendant drop is formed in a sealed cuvette and the initial surface tension measurement, γ_0, is obtained. (b) The vapor is introduced by evaporation of liquid injected into the bottom of the cuvette. (c) The experiments conclude after the interfacial tension reaches constant value, γ_{eq}.

liquid surfactants,[31] the latter reference is notable in focusing on the estimation of the diffusivity of a gas dissolved in a liquid phase (crude oil) in a process that involves mass transport across the gas–liquid interface. In their work, carbon dioxide was introduced into a pendant drop of oil from the gas phase in which the CO_2 composition was maintained constant. The mass flux of the surface active compound (CO_2) is away from the concave side of the drop, which is the opposite direction to fluxes of the traditional liquid-phase surfactants adsorbing at the interface.

The current work builds on the classical concept of using the measurements of the interfacial tension to estimate diffusivities of surface active compounds but differs from prior art in two important aspects. Our approach can be used to measure diffusivities of both gas and liquid solutes impacting interfacial tension; the estimation of the diffusivities of the gas phase compounds is emphasized in this paper. Therefore, the class of species for which diffusivities can be measured is broader than the traditional surfactants.[31] The transport across the interface is allowed in our approach, which is the second differentiating aspect with the practical implication that the estimation of the diffusivities of species soluble in both phases separated by the interface is now possible.

After giving a broad outline of the method in the next section, we proceed to its detailed description for the case when the pendant drop method is used to measure the interfacial tension. We then demonstrate its application to the estimate of diffusivities of several vapors in air, some of which are soluble in the pendant drop and thus are transported across the gas–liquid interface. The paper concludes with the discussion of advantages, limitations, and user guidelines for adapting the general approach to the measurements of specific diffusivities.

METHODS

The selection of the *complementary fluid* (CF) forming the interface with the gas or liquid solvent is the key step of the method. The complementary fluid must form a stable interface with the solvent and the interfacial tension of the CF–solvent interface must measurably depend on the concentration of the solute (which can be a gas or liquid phase species). Zero or low solubility of a solute in the CF is preferred. In such a case, the mass transport of the solute across the solvent-CF interface is zero or small, and the identification of the solute's diffusivity is simplified. With an adequately selected complementary fluid, the dynamic interfacial tension becomes a reporter of the solute concentration in the solvent.

As an illustration, consider the problem of measuring diffusivity of perfluorocarbon (PFC) vapors in air. In this case, water and methanol are adequate complementary fluids because they form a stable interface with air; perfluorocarbon vapors adsorb at the water–air and methanol–air interfaces and reduce the surface tension linearly with the PFC vapor concentration;[32] and the solubility of the PFC's in water and methanol is low.[33]

For the selected complementary fluid, the interfacial tension of the solvent/CF interface as a function of solute concentration must be characterized, known from theory, or empirical correlations. The method for measuring interfacial tension must be selected from a range of well-established alternatives.[34] After a solute is introduced into a known spatial location inside a test cell (maintained at the temperature and pressure of interest), the response of the interfacial tension to the changing concentration of the diffusing solute must be recorded. An appropriate model (which may be based on Fick's, Maxwell–Stefan's, or effective diffusivity description of the mass transport) should be used to predict the solute's concentration at the solvent–CF interface. Such prediction will depend on the diffusion coefficient that we seek to estimate and, perhaps, other unknown parameters characterizing such factors as the transport of the solute across the interface. The values of the diffusion coefficient and other unknown parameters must now be estimated to give the best agreement between the model predictions and the concentration of the solvent obtained from the measurements of the interfacial tension.

In the following, the detailed elaboration of the outlined approach is given for the case when the dynamic interfacial

DOI: 10.1021/ie504355w
Ind. Eng. Chem. Res. XXXX, XXX, XXX−XXX

tension is measured by the pendant drop method. We then proceed to demonstrate its application by measuring the diffusivities of gas-phase species that impact the interfacial tension but do not possess many attributes of the traditional surfactants (for example, they do not have a critical micellar concentration). The cases with and without migration of solutes across the CF-solution interface are considered.

Pendant Drop Implementation. The procedure begins with the introduction of the complementary fluid in the form of a small droplet or a bubble into the volume of the solvent maintained inside a closed test cell at a pressure and temperature of interest. The pendant drop arrangement illustrated in Figure 1a is used with higher density complementary fluids (relative to solution); the inverted buoyant drop or bubble configuration is used otherwise. After allowing for the equilibration between the CF and solvent, the diffusive transport is initiated by introducing the solute at known concentration into predetermined region of the solvent. The illustration in Figure 1b corresponds to the diffusive transport of a vapor introduced into the gas mixture (e.g., air) by evaporation of a corresponding liquid injected into the bottom of the cuvette. The vapor concentration at the liquid surface, used in model predictions, is equal to its vapor pressure.

Diffusive transport leads to the changing vapor concentration in the vicinity of the pendant drop, which affects the measured interfacial tension. The experiment is continued until the concentration reaches a steady state and the tension measurements are stabilized at a constant value. The uniform distribution of the solute at the end of the experiment depicted in Figure 1c is observed when the vapor is insoluble in a complementary fluid.

Using an appropriately selected transport model, the solute concentration in the vicinity of the interface can be predicted. Such prediction depends on the diffusion coefficient, which must be treated as a decision variable. The unknown diffusivity is then obtained by adjusting its value to obtain the best agreement (in an appropriately selected norm) with the concentration-dependent dynamic tension measurements.

As a concrete example of the described model-based data analysis procedure, we consider the case of a CF-insoluble vapor diffusing toward the pendant drop (Figure 1b). Assume that the gas-phase diffusive transport of the solute is adequately described by a one-dimensional Fick's model:

$$\frac{\mathrm{d}c}{\mathrm{d}t} = D\frac{\mathrm{d}^2c}{\mathrm{d}x^2} \tag{1}$$

where c [mol/m^3] is the vapor concentration and D [m^2/s] is the effective or Fick's diffusion coefficient of the solute in the solvent. The initial condition

$$c(x, 0) = 0 \tag{2}$$

assumes zero vapor concentration at initial time. At $t = 0$, the liquid is injected into the cuvette, which establishes the vapor pressure concentration, c_0, at the gas–liquid interface at the bottom of the cell:

$$c(0, t) = c_0 \tag{3}$$

Assuming an enclosed container, the second boundary condition becomes

$$\frac{\mathrm{d}c(L, t)}{\mathrm{d}x} = 0 \tag{4}$$

where L is the distance between the surface of the liquid and the top of the cuvette.

The transport model (eqs 1−4) does not account for the migration of the solute into the complementary fluid and is therefore expected to be adequate only for CF-insoluble solutes. Its analytical solution expressed in the form of the scaled concentration

$$c^* = \frac{c}{c_0} \tag{5}$$

has the following form:

$$c^*(x, t) = 1 - \frac{2}{L}\sum_{k=1}^{\infty} \mathrm{e}^{-D\left(\frac{2k-1}{2L}\pi\right)^2 t} \sin\left(\frac{2k-1}{2L}\pi x\right) \times \int_0^L \sin\left(\frac{2k-1}{2L}\pi x\right)\mathrm{d}x \tag{6}$$

For the conditions of our experiments, this solution was found to be in excellent agreement (data not shown) with the predictions of the corresponding three-dimensional model of the diffusive transport inside the cuvette, which we obtained using COMSOL Multiphysics software (Version 4.4; COMSOL Inc., Burlington, MA).

The diffusion of the vapor leads to an increase in its concentration next to the pendant drop. For an appropriately selected complementary fluid, this leads to the dynamic change in the interfacial tension, γ, obtained from the shape analysis of the pendant drop imaged throughout the experiment. For an image acquired at time t_i, such analysis produces the corresponding dynamic interfacial tension $\gamma(t_i)$, $i = 1,2,3,...,N$, where $\gamma(t_1) = \gamma_0$ is the surface tension prior to the introduction of the solute and $\gamma(t_N) = \gamma_{eq}$ is the value of the tension attained at the equilibrated concentration (Figure 1c). It is convenient to represent the measured interfacial tension as scaled deviations relative to γ_0:

$$\gamma^*(t_i) = \frac{\gamma_0 - \gamma(t_i)}{\gamma_0 - \gamma_{eq}} \tag{7}$$

in which case $\gamma^*(t_1) = 0$ and $\gamma^*(t_N) = 1$.

The vapor concentration next to the surface of the pendant drop, c_{int}, may be estimated from the measurements of the interfacial tension if the functional dependence $\gamma = f(c_{int})$ is known. The experimental system selected to demonstrate the application of the method involved several vapors diffusing though the air and a pendant drop of two complementary fluids (water and methanol). Out of several alternatives (adsorption isotherms) discussed above, the linear concentration vs surface tension relationship was found to be the most appropriate in this case.[32] In the normalized and scaled form, this simply gives

$$c^*_{int}(t) = \gamma^*(t) \tag{8}$$

If the diffusivity coefficient was known, the value of the analytical solution (eq 6) at the location of the pendant drop, x_d, can be used to predict c^*_{int} as $c^*(x_d,t_i)$. Therefore, we can estimate the diffusion coefficient by finding the value of D that minimizes the difference between the measured (eq 8) and the model predicted concentrations. If we use the sum of squared errors to quantify how well the model explains the acquired measurements, then the problem is to find D that minimizes the cost function

DOI:10.1021/ie504355w
Ind. Eng. Chem. Res. XXXX, XXX, XXX−XXX

$$J = \sum_{i=1}^{N} [\gamma^s(t_i) - c^s(x_d, t_i)]^2 \quad (9)$$

Using the values of $c^s(x_d,t_i)$ given by the analytical solution (eq 6) and the necessary condition for optimality,

$$\frac{dJ}{dD} = 0$$

the following nonlinear equation that depends on unknown D is obtained:

$$\sum_{i=1}^{N}\left[\gamma^s(t_i) - 1 + \frac{2}{L}\sum_{k=1}^{\infty} e^{-D\left(\frac{2k-1}{2L}\pi\right)^2 t_i}\sin\left(\frac{2k-1}{2L}\pi x_d\right) \times \int_0^L \sin\left(\frac{2k-1}{2L}\pi x\right)dx\right]\sum_{k=1}^{\infty}\left(\frac{2k-1}{2L}\pi\right)^2 t_i\, e^{-D\left(\frac{2k-1}{2L}\pi\right)^2 t_i} \times \sin\left(\frac{2k-1}{2L}\pi x_d\right)\int_0^L \sin\left(\frac{2k-1}{2L}\pi x\right)dx = 0 \quad (10)$$

where $\gamma^s(t_i)$ is the scaled measurements of the interfacial tension. We can now find an unknown D as a numerical solution of eq 10.

DEMONSTRATION

Experiments. The developed method was used to measure the diffusivity of several vapors in air. The first group of vapors—perfluoropentane (PFP, C_5F_{12}), perfluorohexane (PFH, C_6F_{14}), hexane (C_6H_{14}), and heptane (C_7H_{16})—is comprised of compounds largely insoluble in the selected complementary fluids. In the case of PFP and PFH, as complementary fluids we used DI water and methanol. Only DI water was used with C_6H_{14} and C_7H_{16}. Vapors in the second group—methanol and ethanol—are soluble in the complementary fluids, which were either DI water or water containing a 0.25 mM solution of cetyltrimethylammonium bromide (CTAB), an ionic surfactant. Research grade PFP and PFH were purchased from FluoroMed (Round Rock, TX). Hexane and heptane were purchased from Aldrich Chemical Co. (St. Louis, MO). Methanol and ethanol were purchased from Fischer Scientific (Bridgewater, NJ). PFP in a sealed container was kept in a refrigerator at 1 °C. Sealed containers of PFH, hexane, heptane, ethanol, and methanol were kept at room temperature (maintained at 20 ± 1 °C).

A custom pendant-drop tensiometer (described and validated elsewhere[32]) was used to provide interfacial tension measurements at high sampling rates. Rapid measurements are essential as the vapor concentration changed rapidly at the beginning of each experiment. Custom software (implemented in Matlab; MathWorks, Natick, MA) was used to capture, preprocess, and analyze images at rates as high as 15 fps. In most cases, the measurements of the interfacial tension, droplet volume, and its surface area were acquired approximately every 1.4 s.

The experiments were conducted at room temperature in the laboratory located ~1470 m above the sea level. The apparatus consisted of an airtight cuvette (10 × 10 × 45 mm) in which a pendant drop of a complementary liquid (water or methanol) was introduced at the end of the stainless steel syringe needle (1.6/2.09 mm inside/outside diameter). The drop was allowed to equilibrate until its temperature, measured by a thermal camera (FLIR, Wilsonville, OR) through a KBr (IR-transparent) window, attained the ambient value. The equilibration was confirmed by measuring the volume of the drop, which reached its steady state value at approximately the same time as needed for thermal equilibration. After the equilibration, the vapor of interest was introduced by evaporation of liquid form of the studied compound injected into the bottom of the sealed cuvette. As the vapor diffused toward the drop, the interfacial tension was continuously measured until the steady state value was attained. At the steady state, the vapor concentrations of compounds insoluble in the complementary fluid are distributed uniformly and are equal to the vapor pressure. Such outcome is correctly predicted by the model (eqs 1−4). For soluble vapors (methanol and ethanol), the mass transfer across the interface of the pendant drop takes place, the vapor concentration inside the cuvette is spatially nonuniform, and a simple mass transfer model (eqs 1−4) no longer gives accurate predictions. In all cases, the interfacial tension attains a constant value, $\gamma(t_N) = \gamma_{eq}$, when a steady state vapor distribution (uniform or not) is reached. The distances shown in Figure 1 were measured from the surface of the injected liquid to the top of the cuvette, L, and the center of the pendant drop, x_d. They were obtained twice: immediately after the liquid injection ($t = t_1$) and after the equilibrium interfacial tension was attained ($t = t_N$). The average of the two measurements was used in eq 10 from which the diffusivity was calculated.

The described experimental and data analysis procedures were repeated three times for each vapor−complementary fluid combination. In the case of PFP and PFH vapors, two different complementary fluids (water and methanol) were used. The diffusivity was calculated individually for each experiment and by simultaneously using data obtained during all three repeat experiments.

Results. The measurements of changing interfacial tension in the scaled form, γ^s, for all vapor−CF combinations are shown in Figure 2, where $t = 0$ is the time when the liquid was injected into the cuvette. Each subplot shows all data points acquired during three separate repeat experiments. Each individual experiment took less than 10 min from the liquid injection to the equilibration of the surface tension. This time was less than 5 min for faster diffusing ethanol and methanol vapors.

The estimated diffusivities, found by solving eq 10 using data in Figure 2, are summarized in Table 1. The estimates were obtained using data from separate runs and the combined data from all runs used simultaneously. Smooth curves in Figure 2 indicate model predictions of the interfacial tension given by eq 8, where c_{int} was estimated as $c^s(x_d,t_i)$ and calculated from eq 6, where we used the diffusion coefficients identified by solving eq 10. The distances L and x_d needed to solve eq 10 and calculate $c^s(x_d,t_i)$ were found by averaging the measurements in the repeat experiments. In different runs, L ranged from 35 to 39 mm, while x_d was measured to be between 11 and 16 mm.

The goodness of fit of model predictions shown in Figure 2 was characterized by R^2 values calculated as

$$R^2 = 1 - \frac{\sum_{i=1}^{N_{total}} [\gamma^s(t_i) - c^s(x_d, t_i)]^2}{\sum_{i=1}^{N_{total}} (\gamma^s(t_i) - \overline{\gamma^s})^2} \quad (11)$$

Here, N_{total} is the total number of data points in repeated experiments and $\overline{\gamma^s}$ is the average value of the measured tension. The calculated values based on the data from separate runs and all data used simultaneously are listed in Table 1.

The obtained diffusivities were compared with the values given by the Fuller−Schettler−Giddings (FSG) empirical correlation.[35] The agreement is good for all solutes that are poorly soluble in the complementary fluid (solubility data are summarized in Table 2). At the same time, our estimates predict a lot higher diffusivities (almost twice as high as the FSG correlation values) for the CF-soluble cases of methanol−water and

DOI:10.1021/ie504355w
Ind. Eng. Chem. Res. XXXX, XXX, XXX−XXX

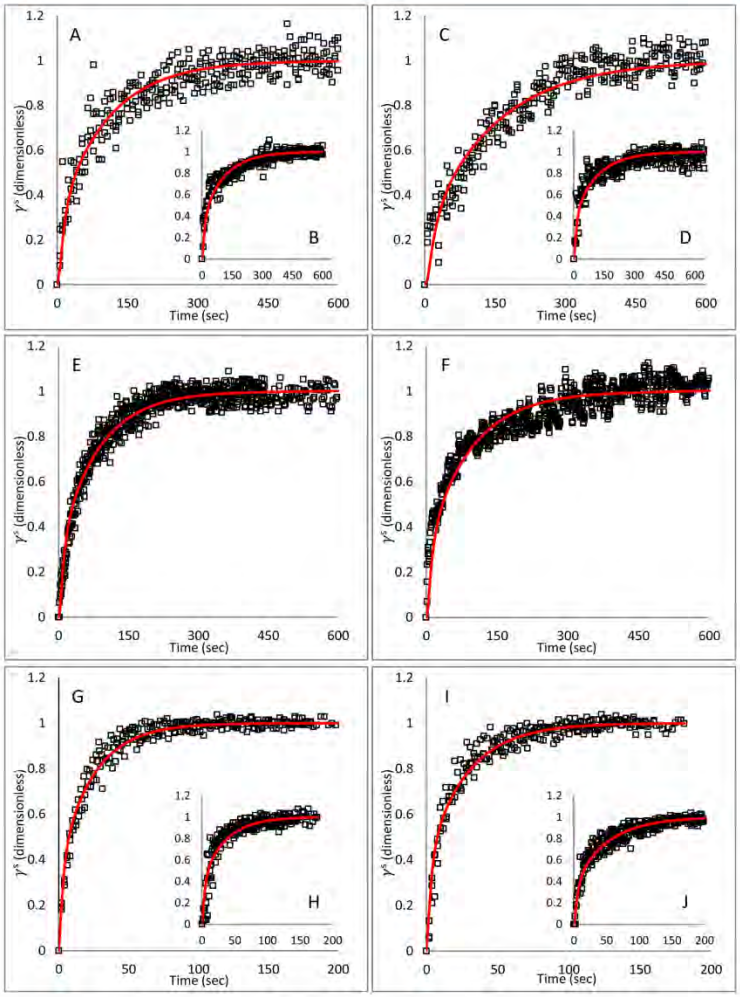

Figure 2. Measurements of the interfacial tension obtained in three repeated experiments are presented in the scaled form, $\gamma^s(t_i)$. The corresponding model predictions were obtained with the diffusion coefficients estimated by solving eq 10 and are shown as solid lines. (A) Case of PFP vapor diffusing through air with water as a complementary fluid. (B) Case of PFP vapor with MeOH as CF. (C) PFH/water system. (D) PFH/MeOH. (E) Hexane/water. (F) Heptane/water. (G) Methanol/water. (H) Methanol/0.25 mM CTAB system. (I) Ethanol/water. (J) Ethanol/0.25 mM CTAB system.

ethanol−water systems. The improvement achieved after the complementary fluid was modified by adding a surfactant and by taking into account the transport of the solute into the liquid phase are discussed below.

■ DISCUSSION

The primary objective in selecting a complementary fluid is to achieve a reasonably high sensitivity of the interfacial tension to changes in a solute concentration. Given multiple choices, the secondary objective is to select the CF with low solubility of the surface active species. When solubility is low, the solute is mostly confined to the bulk solution and the interface, which allows us to use a simple mass transport model and simplifies the data analysis needed to determine the diffusivity. In the case of PFP, PFH, hexane, and heptane vapors diffusing in air, water is an adequate complementary fluid because the tension of the air−water

DOI: 10.1021/ie504355w
Ind. Eng. Chem. Res. XXXX, XXX, XXX−XXX

Table 1. Comparison of Diffusion Coefficients of Vapors in Air (D in $[m^2/s] \times 10^{-6}$)

		interfacial tension method								
		run 1		run 2		run 3		all γ^* data		
vapor	CF	D	R^2	D	R^2	D	R^2	D	R^2	FSG correlation
PFP	water	5.01	0.81	4.95	0.91	4.94	0.91	4.96	0.87	4.97
PFP	methanol	4.93	0.88	4.99	0.87	4.82	0.83	4.95	0.86	4.97
PFH	water	4.26	0.78	4.66	0.75	4.15	0.78	4.09	0.77	4.60
PFH	methanol	4.43	0.86	4.52	0.80	4.37	0.86	4.38	0.75	4.60
hexane	water	6.77	0.92	6.76	0.91	6.84	0.93	6.70	0.90	6.80
heptane	water	6.38	0.85	6.33	0.79	6.35	0.75	6.40	0.72	6.37
methanol	water	24.1	0.97	20.9	0.96	20.6	0.98	21.7	0.99	11.9
methanol	0.25 mM CTAB	15.6	0.91	15.4	0.86	13.3	0.84	14.1	0.86	11.9
ethanol	water	18.5	0.96	17.8	0.99	19.2	0.95	18.4	0.95	9.9
ethanol	0.25 mM CTAB	11.9	0.94	8.91	0.96	9.06	0.95	9.64	0.93	9.9

Table 2. DI Water Solubility Data

solute	temp. (°C)	solubility (mol/L)
perfluoropentane[33]	25[a]	4.00×10^{-6}
perfluorohexane[33]	25[a]	2.70×10^{-7}
hexane[44,45]	20	1.39×10^{-4}
heptane[45,46]	20	2.39×10^{-5}
methanol[47]	20	miscible
ethanol[47]	20	miscible

[a]Solubility at temperature other than 25 °C was not reported.

interface is highly sensitive to the concentration of these vapors and their solubility in water is very low. As long as both objectives are met, the specific CF selection does not appear to matter, as suggested by comparably accurate estimations the diffusivities of perfluorocarbon vapors achieved with either water or methanol as a complementary fluid.

The task of selecting an adequate CF to estimate diffusivities of alcohol vapors proved to be more challenging. An attempt to use mineral oils, in which MeOH and EtOH do not dissolve appreciably, was unsuccessful because the interfacial tension of the air−oil interface showed no measurable sensitivity to changes in methanol and ethanol concentration in air. At the same time, the sensitivity of air−water interface to the concentration of alcohol vapors is significant, but both compounds readily dissolve in water. Without known alternatives, water was selected as a complementary fluid. However, when a simple model (eqs 1−4) was used to estimate the diffusion coefficient, the result substantially overestimated the value of D. To understand the source of this problem, note that the response of the interfacial tension for CF-soluble vapors of methanol and ethanol (Figure 2G and I) shows faster equilibration than seen with vapors that do not dissolve in the complementary fluid (e.g., Figure 2A and E). Based on a simple model (eqs 1−4) that ignores transport of MeOH and EtOH across the interface, this behavior can only be explained by higher diffusivity. In reality, the interaction of two different transport processes contributes to faster equilibration: a diffusive influx of alcohol vapors toward the gas−liquid interface and the liquid-phase flux that carries the solute away from the interface due to its absorption into and transport through the complementary fluid.

To obtain a more accurate estimation of the diffusivity in this case, the data interpretation should be based on a model that takes both processes into account. One approach is to modify the model (eqs 1−4) by adding a "reaction" (or sink) term that describes the loss of the solute to the liquid phase:

$$\frac{dc}{dt} = D\frac{d^2c}{dx^2} - kc(x, t)\delta(x - x_d) \tag{12}$$

where δ is the Dirac delta function that is used to localize the reaction term to the location x_d of the pendant drop. The initial and boundary conditions for model eq 12 are still given by eqs 2−4. The diffusivity D and the rate constant k, characterizing the intensity of cross-interfacial loss of solute into the complementary fluid, are both unknown in this model. Their values that provide the best fit to the measurements of the dynamic interfacial tension are found as the solution of the following optimization problem:

$$(D^*, k^*) = \arg\min_{D,k} J \tag{13}$$

where the cost function given by eq 9 is used. We found the optimal values of D and k using an iterative gradient search. For methanol and ethanol vapors, the behavior of J as a function of unknown diffusivity and adsorption rate in the proximity of optimal values D^* and k^* is shown in Figures 3A and B. The actual values and comparisons with the diffusivities obtained without accounting for the cross-interfacial transport of the solute are given in Table 3, which shows that with a more adequate model the identified diffusivities are substantially closer to the values provided by the FSG correlation. The value of the rate k characterizes the absorption of the solute into the complementary fluid and is of separate interest, which we do not pursue further in this paper.

Figure 3C and D compare the measurements of the interfacial tension and model predictions obtained with and without accounting for the transport across the interface. They indicate that by adding the sink term to the model (eq 12), we are able to adequately explain a more rapid transition to the equilibrium without using an unreasonably high value of the diffusivity coefficient. Solid blue lines in Figure 3C and D show predictions obtained with the model eq 12 and the values of D and k listed in Table 3. The sum of squared errors of these predictions are J = 0.017 and 0.098 for methanol and ethanol vapors, respectively. The corresponding model predictions shown in Figure 2G and I and obtained without accounting for cross-interfacial transport are reproduced for comparison as red lines in Figure 3C and D. They have a lower goodness of fit to data (J = 0.021 for methanol and 0.29 for ethanol).

Further improvements in the accuracy of the identified diffusivity may be expected with a more accurate transport model that (i) accounts for nonuniformity of the solvent concentration along the interface; simple models (eq 1) and (eq 12) approximate the interface as a single point at the coordinate x_d;

DOI:10.1021/ie504355w
Ind. Eng. Chem. Res. XXXX, XXX, XXX−XXX

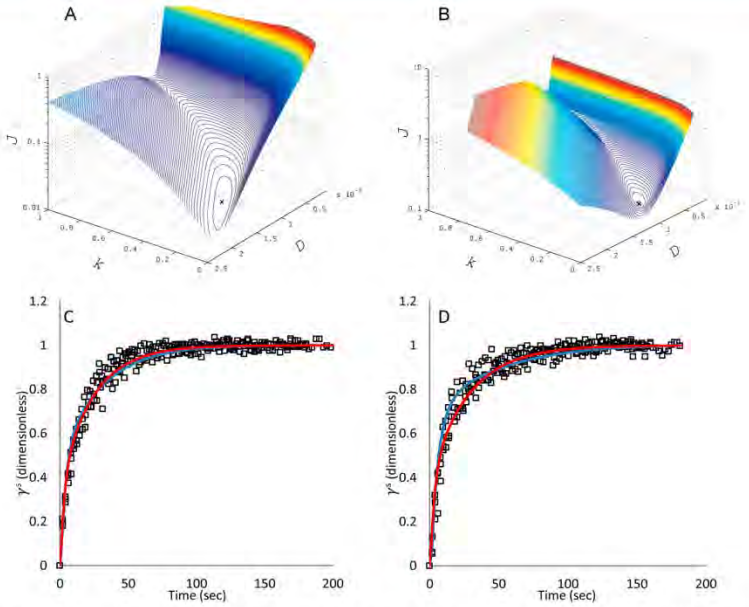

Figure 3. Sum of squared errors J as a function of the diffusivity coefficient D and the adoption rate constant k for methanol (A) and ethanol (B). The minima are marked with × and are achieved with D and k values listed in Table 3. Panels C and D compare the measured surface tension (presented as the scaled deviation from the initial value, $\gamma^s(t_i)$) for methanol and ethanol, respectively, with the predicted values. Predictions based on the model eq 1 are shown in red. Blue lines show predictions of the model eq 12 that accounts for cross-interfacial mass transport.

Table 3. Diffusion Coefficients (D in $(m^2/s) \times 10^{-6}$) and Rate Constants (k in m/s) Identified with Different Models and Complementary Fluids

vapor	model	CF	rate, k	diffusivity, D	D by FSG correlation
methanol	eq 1, $k = 0$	water	–	21.7	11.9
methanol	eq 1, $k = 0$	0.25 mM CTAB	–	14.1	11.9
methanol	eq 12	water	0.250	14.0	11.9
ethanol	eq 1, $k = 0$	water	–	18.4	9.9
ethanol	eq 1, $k = 0$	0.25 mM CTAB	–	9.64	9.9
ethanol	eq 12	water	0.235	7.0	9.9

(ii) uses an isotherm that accounts for the changing concentration of the solute in the complementary fluid when cross-interfacial mass transport occurs; (iii) describes the transport of the solute in the complementary fluid to account for the change in CF composition. Such compositional effect on the interfacial tension was found to be important for alcohol–water systems.[36]

From other applications (e.g., refs 37 and 38), we know that surfactants adsorbed at the interface can increase the resistance to cross-interfacial mass and heat transport. To investigate if similar phenomena occurs with CF-soluble alcohol vapors, the experiments were repeated using 0.25 mM aqueous solution of CTAB as a complementary fluid (critical micellar concentration for CTAB is ~1 mM). After the equilibration of the modified CF and prior to the introduction of alcohol vapors, the surface tension of 0.25 mM CTAB solution was 57 mN/m, which agrees well with literature values.[39] To quantify the absorption of MeOH and EtOH with and without the surfactant, the pendant drop's volume was measured in both cases. Figure 4A shows the measured change of the volume in typical experimental runs, each starting with the pendant drop of an approximately equal size. The results indicate a lower rate of volume increase when the surfactant is present, suggesting an increased resistance to the transport of vapors into the liquid phase provided by a layer of CTAB molecules adsorbed at the interface. Note that the volume did not increase in all experiments with CF-insoluble solutes, as illustrated in Figure 4A for a hexane–water system.

For DI water and 0.25 mM CTAB solution, Figure 4B compares the response of the surface tension to changing concentration of CF-soluble MeOH and EtOH vapors. It indicates that the addition of the CTAB lengthens the equilibration time for both vapors. We quantified the equilibration time using a first order fit of the surface tension data (not shown). It was found that the addition of CTAB has increased the time constant of the response from 18.8 to 28.2 s for methanol; for ethanol, the increase was from 23.5 to 39.9 s. When the model (eqs 1–4) is used to identify the diffusivity coefficients after CTAB modification of the commentary fluid, longer equilibration times lead to the identification of a much smaller diffusion coefficient and closer agreement with FSG correlation.

The diffusion coefficients obtained with or without surfactant in the complementary fluid and identified based on models that either account or ignore mass transport across the interface

DOI: 10.1021/ie504355w
Ind. Eng. Chem. Res. XXXX, XXX, XXX−XXX

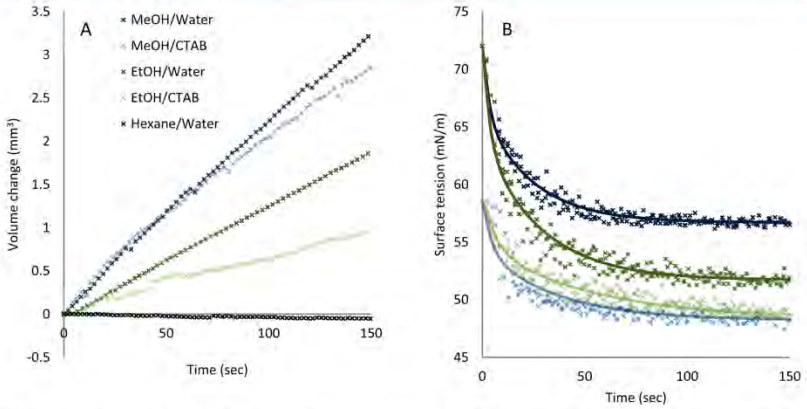

Figure 4. (A) Change in the pendant drop volume during the experiments with several vapors introduced into the test cell at $t = 0$. (B) By adding the surfactant (CTAB), the equilibration time of surface tension in response to changing concentration of water-soluble MeOH and EtOH vapors is lengthened. Solid lines show the corresponding predictions obtained by using model eqs 1−4 and the diffusivity coefficients listed in Table 3.

(Table 3) reveal the following trend. More accurate values of D are identified based on a simple model (eqs 1−4) when a surfactant was added to the complementary fluid to impede the transport of the solute across the interface, and an improved accuracy is achieved when the identification was based on a more appropriate model (eq 12).

The results in Table 3 are shown for D found by simultaneously using all measurements from the repeat experiments. The values obtained using data from separate runs is included in Table 1 for the case of CTAB-modified complementary fluid and the data analysis based on model eqs 1−4.

■ CONCLUSION

The measurements of the dynamic tension on small interfaces, such as those formed around droplets and bubbles, may be used to estimate spatially localized, transient concentrations of a surface active species as it diffuses through a solvent. This work continues a long series of studies exploiting such indirect concentration measurements to identify the diffusion coefficient of surface active solutes with the following differentiation from prior contributions: (a) The selection of the experimental system needed to achieve an accurate diffusivity estimation and, particularly, the selection of the complementary fluid to create the interface sensitive to the solute concentration is emphasized. (b) The method is applied to solutes beyond traditional liquid-phase surfactants, which expands the usefulness of the approach to the measurements of diffusivities of gas-phase species and, perhaps, nanoparticles. (c) The approach is adapted to the cases when a species of interest is soluble in the complementary fluid and is therefore transported across the interface.

The approach is demonstrated in the pendant drop configuration and its ability to accurately estimate diffusivities of several vapors in air is shown. Without modifications, the method can be used to measure liquid phase diffusivities. It is well suited to the measurements of diffusivities over a broad range of temperatures and pressures.

Two different complementary fluids—water and methanol—were used to measure the diffusivity of perfluorocarbon and hydrocarbon vapors through the air. Both perfluorocarbons and hydrocarbons have very low solubility in the selected complementary fluids. The diffusivity of the PFP estimated based on data collected during three separate runs was within less than 1% of the FSG correlation values for both complementary fluids; for PFH, the difference was within 11%. The agreement is even better for the diffusivities of hexane and heptane with water as a complementary fluid (less than 1% and 1.5%, respectively). In all cases, the estimates can be obtained very rapidly (in less than 10 min for a single experiment) and require only basic imaging and laboratory equipment. For the range of tested concentrations, the interfacial tension changes linearly with the vapor concentration. In this case, the inverse problem of finding diffusivity D is particularly simple and reduces to a numerical solution of a single nonlinear eq 10 for CF-insoluble solutes.

A substantially lower agreement (larger than 80% difference with the FSG correlation) was initially obtained for solutes—methanol and ethanol vapors—that readily dissolve in the complementary fluid (water). When a mass transport model was modified to account for the absorption of alcohols into water, the agreement has improved considerably. It was also shown that by adding a surfactant to the complementary fluid, the accuracy of the diffusivity estimation is improved even without accounting for the absorption of alcohols into aqueous phase. We explained this effect by an increased resistance to cross-interfacial mass transport provided by a layer of the surfactant molecules adsorbed to the interface. These observations reinforce the importance of careful selection of the complementary fluid, outline several degrees of freedom available to a user in selecting the most appropriate experimental system, data interpretation procedure, and the versatility of the proposed method.

As with all indirect methods, the transformation of the measured property into the corresponding concentration is the source of potential errors. To reduce such errors, several guidelines are suggested. The primary requirement is an appropriate selection of complementary fluid to form solvent−CF interface with as high as possible sensitivity of the interfacial tension to the changes in the solute concentration. Our experience shows that

DOI: 10.1021/ie504355w
Ind. Eng. Chem. Res. XXXX, XXX, XXX−XXX

satisfying this requirement may not be possible without some solubility of the solute in a complementary fluid. In such a case, a user should attempt to impede the cross-interfacial mass transfer by adding a surfactant to a complementary fluid and/or explicitly account from the absorption of the solute into the CF by an appropriate selection of mass transport model used to estimate the diffusion coefficients.

An accurate relationship (adsorption isotherm) between the interfacial tension and the bulk concentration of the surface active solute, $\gamma = f(c)$, must be known from experiments, correlations, or theory in order to apply the proposed approach. In some cases, this relationship is simple and linear; examples include the solute−solvent−CF combinations considered in this paper and alkylethylene glycol as a solute in water with air used as a complementary fluid (this corresponds to a buoyant bubble configuration of the method). In other cases, the interfacial tension changes linearly with the log of the solute concentration (as in the case of CTAB in water−air system) or has an even more complex relationship (see, for example, refs 40−42; ref 42 gives examples of solutes that increase the interfacial tension). The particular form of $\gamma = f(c)$ relationship does not affect the work flow in determining the diffusivity. However, finding the diffusivity reduces to the solution of a single nonlinear eq 10 only when this relationship is linear and the model does not include a sink term describing cross-interfacial transport of the solute.

The size of the interface with the complementary fluid relative to the concentration gradient of the solute is another important consideration. For higher gradients, the dimension of the interface in the direction of changing concentration should be reduced.

Nonuniformity in the solute concentration in the proximity of the interface is reduced if the area of the interface is small. Therefore, the measured tension is a more accurate reflection of the point concentration of the solute when small pendant drops (or buoyant bubbles and drops) are used. However, the shape of small pendant drops is more spherical and less sensitive to changes in the interfacial tension. Therefore, the trade-off between keeping the size of the interface small and the sensitivity of its shape to changes in the solute concentration exists.

The described unavoidable trade-off in measuring surface tension based on the shape analysis motivates the search for alternatives to the pendant drop configuration. One such alternative is to measure pressure needed to create and maintain a hemispherical interface at the end of the capillary (capillary pressure method) filled with the complementary fluid and immersed into the solution. Such pressure is easily distinguishable as being the maximum pressure observed when the complementary fluid is slightly advanced or withdrawn from the capillary. By obtaining the interfacial tension from pressure measurements, the need to visualize the interface is removed, which is particularly appealing when measuring diffusivity in situ. The size of the interface is controlled by the size of the capillary orifice, which can be as small as a few nanometers in diameter.[43]

The applicability of the presented method to the measurements of gas phase diffusivities of the compounds other than the traditional liquid-phase surfactants is an important feature of the presented approach. Our initial observation[32] that revealed strong surface active properties of perfluorocarbon vapors has now been expanded to include vapors of light hydrocarbons and alcohols.

AUTHOR INFORMATION

Corresponding Author

*E-mail: mikhail.skliar@utah.edu.

Notes

The authors declare no competing financial interest.

ACKNOWLEDGMENTS

The authors acknowledge support from the National Science Foundation (award number IGERT-0903715) and the University of Utah (Graduate Research Fellowship award to V.S.C).

REFERENCES

(1) Fogler, S. H. *Elements of Chemical Reaction Engineering*, 4th ed.; Prentice-Hall: Upper Saddle River, NJ, 1999.

(2) Poling, B. E.; Prausnitz, J. M.; O'Connell, J. P. *Properties of Gases and Liquids*, 5th ed.; McGraw-Hill: New York, 2007.

(3) Schmidt, T. *Mass Transfer by Diffusion In AOSTRA Handbook on Oil Sands, Bitumens and Heavy Oils*; AOSTRA: Alberta, 1989.

(4) Behzadfar, E.; Hatzikiriakos, S. G. Diffusivity of CO_2 in Bitumen: Pressure−Decay Measurements Coupled with Rheometry. *Energy Fuels* **2014**, *28*, 1304.

(5) Grogan, A. T.; Pinczewski, W. V. The Role of Molecular Diffusion Processes in Tertiary CO_2 Flooding. *Soc. Pet. Eng.* **1987**, *39*, 591.

(6) Renner, T. A. Measurement and Correlation of Diffusion Coefficients for CO_2 and Rich-Gas Applications. *SPE Reservoir Eng.* **1988**, *3*, 517.

(7) Ostlund, J.-A.; Wattana, P.; Nydén, M.; Fogler, H. S. Characterization of Fractionated Asphaltenes by UV−Vis and NMR Self-Diffusion Spectroscopy. *J. Colloid Interface Sci.* **2004**, *271*, 372.

(8) Fuller, E. N.; Ensley, K.; Giddings, J. C. Diffusion of Halogenated Hydrocarbons in Helium. The Effect of Structure on Collision Cross Sections. *J. Phys. Chem.* **1969**, *73*, 3679.

(9) Funazukuri, T.; Kong, C. Y.; Kagei, S. Binary Diffusion Coefficients in Supercritical Fluids: Recent Progress in Measurements and Correlations for Binary Diffusion Coefficients. *J. Supercrit. Fluids* **2006**, *38*, 201.

(10) Rouholahnejad, F.; Tabrizchi, M. A New Method for Measuring the Diffusion Coefficient in a Gas Phase. *J. Phys. Chem. A* **2006**, *110*, 11208.

(11) Zhang, Y. P.; Hyndman, C. L.; Maini, B. B. Measurement of Gas Diffusivity in Heavy Oils. *J. Pet. Sci. Eng.* **2000**, *25*, 37.

(12) Lobo, V. M. M.; Ribeiro, A. C. F.; Verissimo, L. M. P. Diffusion Coefficients in Aqueous Solutions of Potassium Chloride at High and Low Concentrations. *J. Mol. Liq.* **1998**, *78*, 139.

(13) Anderson, J. S.; Saddington, K. S 80. The Use of Radioactive Isotopes in the Study of the Diffusion of Ions in Solution. *J. Chem. Soc.* **1949**, S381.

(14) Rohling, J. H.; Shen, J.; Wang, C.; Zhou, J.; Gu, C. E. Determination of Binary Diffusion Coefficients of Gases Using Photothermal Deflection Technique. *Appl. Phys. B: Laser Opt.* **2007**, *87*, 355.

(15) De Mezquia, D. A.; Bou-Ali, M. M.; Larrañaga, M.; Madariaga, J. A.; Santamaría, C. Determination of Molecular Diffusion Coefficient in *n*-Alkane Binary Mixtures: Empirical Correlations. *J. Phys. Chem. B* **2012**, *116*, 2814.

(16) Milner, S. R. On Surface Concentration and the Formation of Liquid Films. *Philos. Mag. Ser. 6* **1907**, *13*, 96.

(17) Ward, A. F. H.; Tordai, L. Time Dependence of Boundary of Solutions. I. The Role of Diffusion in Time Effect. *J. Chem. Phys.* **1946**, *14*, 453.

(18) Mulqueen, M.; Stebe, K. J.; Blankschtein, D. Dynamic Interfacial Adsorption in Aqueous Surfactant Mixtures: Theoretical Study. *Langmuir* **2001**, *17*, 5196.

(19) Mulqueen, M.; Datwani, S. S.; Stebe, K. J.; Blankschtein, D. Dynamic Surface Tensions of Aqueous Surfactant Mixtures: Experimental Investigation. *Langmuir* **2001**, *17*, 7494.

(20) Ariel, G.; Diamant, H.; Andelman, D. Kinetics of Surfactant Adsorption at Fluid−Fluid Interfaces: Surfactant Mixtures. *Langmuir* **1999**, *15*, 3574.

(21) Reichert, M. D.; Alvarez, N. J.; Brooks, C. F.; Grillet, A. M.; Mondy, L. a.; Anna, S. L.; Walker, L. M. The Importance of

DOI:10.1021/ie504355w
Ind. Eng. Chem. Res. XXXX, XXX, XXX−XXX

Experimental Design on Measurement of Dynamic Interfacial Tension and Interfacial Rheology in Diffusion-Limited Surfactant Systems. *Colloids Surf., A* **2015**, *467*, 135.
(22) Chang, C.-H.; Franses, E. I. Adsorption Dynamics of Surfactants at the Air/Water Interface: A Critical Review of Mathematical Models, Data, and Mechanisms. *Colloids Surf., A* **1995**, *100*, 1.
(23) Sutherland, K. The Kinetics of Adsorption at Liquid Surfaces. *Aust. J. Chem.* **1952**, *5*, 683.
(24) Delahay, P.; Fike, C. T. Adsorption Kinetics with Diffusion Control—The Plane and the Expanding Sphere. *J. Am. Chem. Soc.* **1958**, *80*, 2628.
(25) McCoy, B. J. Analytical Solutions for Diffusion-Controlled Adsorption Kinetics with Nonlinear Adsorption Isotherms. *Colloid Polym. Sci.* **1983**, *261*, 535.
(26) Borwankar, R. P.; Wasan, D. T. The Kinetics of Adsorption of Surface Active Agents at Gas−Liquid Surfaces. *Chem. Eng. Sci.* **1983**, *38*, 1637.
(27) Adamczyk, Z. Nonequilibrium Surface Tension for Mixed Adsorption Kinetics. *J. Colloid Interface Sci.* **1987**, *120*, 477.
(28) Van den Bogaert, R.; Joos, P. Diffusion-Controlled Adsorption Kinetics for a Mixture of Surface Active Agents at the Solution−Air Interface. *J. Phys. Chem.* **1980**, *84*, 190.
(29) Hansen, R. S. The Theory of Diffusion Controlled Absorption Kinetics with Accompanying Evaporation. *J. Phys. Chem.* **1960**, *64*, 637.
(30) Yang, D.; Gu, Y. Determination of Diffusion Coefficients and Interface Mass-Transfer Coefficients of the Crude Oil−CO_2 System by Analysis of the Dynamic and Equilibrium Interfacial Tensions. *Ind. Eng. Chem. Res.* **2008**, *47*, 5447.
(31) Eastoe, J. U.; Dalton, J. S. Dynamic Surface Tension and Adsorption Mechanisms of Surfactants at the Air−Water Interface. *Adv. Colloid Interface Sci.* **2000**, *85*, 103.
(32) Chernyshev, V. S.; Skliar, M. Surface Tension of Water in the Presence of Perfluorocarbon Vapors. *Soft Matter* **2014**, *10*, 1937.
(33) Kabalnov, A. S.; Makarov, K. N.; Shcherbakova, O. V.; Nesmeyanov, A. N. Solubility of Fluorocarbons in Water as a Key Parameter Determining Fluorocarbon Emulsion Stability. *J. Fluor. Chem.* **1990**, *50*, 271.
(34) Dukhin, S. S.; Kretzschmar, G.; Miller, R. *Dynamics of Adsorption at Liquid Interfaces: Theory, Experiment, Application*; Elsevier: Amsterdam, 1995.
(35) Taylor, R., Krishna, R. *Multicomponent Mass Transfer*, 1st ed.; Wiley: New York, 1993.
(36) Vazquez, G.; Alvarez, E.; Navaza, J. M. Surface Tension of Alcohol Water + Water from 20 to 50 °C. *J. Chem. Eng. Data* **1995**, *40*, 611.
(37) Connor, L. M.; Bidani, A.; Goerke, J.; Clements, J. A.; Postlethwait, E. M. NO_2 Interfacial Transfer Is Reduced by Phospholipid Monolayers. *J. Appl. Physiol.* **2001**, *91*, 2024.
(38) Henry, D. J.; Dewan, V. I.; Prime, E. L.; Qiao, G. G.; Solomon, D. H.; Yarovsky, I. Monolayer Structure and Evaporation Resistance: A Molecular Dynamics Study of Octadecanol on Water. *J. Phys. Chem. B* **2010**, *114*, 3869.
(39) Lundqvist, H.; Eliasson, A. C.; Olofsson, G. Binding of Hexadecyltrimethylammonium Bromide to Starch Polysaccharides. Part I. Surface Tension Measurements. *Carbohydr. Polym.* **2002**, *49*, 43.
(40) Miles, G. D.; Shedlovsky, L. Minima in Surface Tension−Concentration Curves of Solutions of Sodium Alcohol Sulfates. *J. Phys. Chem.* **1944**, *48*, 57.
(41) Posner, A. .; Anderson, J. .; Alexander, A. . The Surface Tension and Surface Potential of Aqueous Solutions of Normal Aliphatic Alcohols. *J. Colloid Sci.* **1952**, *7*, 623.
(42) Weissenborn, P. K.; Pugh, R. J. Surface Tension and Bubble Coalescence Phenomena of Aqueous Solutions of Electrolytes. *Langmuir* **1995**, *11*, 1422.
(43) Lan, W.-J.; White, H. S. Diffusional Motion of a Particle Translocating through a Nanopore. *ACS Nano* **2012**, *6*, 1757.
(44) Budantseva, L. S.; Lesteva, T. M.; Nemstov, M. S. Deposited Doc. (1976), VINITI 437−476. *Zh. Fiz. Khim.* **1976**, *50*, 1344.
(45) Jönsson, J. Å.; Vejrosta, J.; Novák, J. Air/Water Partition Coefficients for Normal Alkanes (*n*-Pentane to *n*-Nonane). *Fluid Phase Equilib.* **1982**, *9*, 279.
(46) Nelson, H. D.; de Ligny, C. L. The Determination of the Solubilities of Some *n*-Alkanes in Water at Different Temperatures, by Means of Gas Chromatography. *Recl. Trav. Chim. Pays-Bas* **1986**, *87*, 528.
(47) Edding, D.; Gammon, S. D. *General Chemistry*, 10th ed.; Cengage Learning: Boston, 2008.

DOI: 10.1021/ie504355w
Ind. Eng. Chem. Res. XXXX, XXX, XXX−XXX

CHAPTER 4

ADSORPTION OF PERFLUOROCARBON VAPORS TO THE WATER SURFACE

4.1 Abstract

Perfluorocarbons (PFCs), e.g., perfluoropentane (PFP), are biocompatible compounds having low toxicity and chemical properties that allow them to be used in a variety of medical applications. Although a substantial amount of research was done in this area, the study of interfacial properties of PFP in aqueous systems has received limited attention. Our previous work investigated the influence of PFC vapor on the surface tension of water at room temperature. A significant decrease in surface tension of water in the presence of PFC vapor and a linear correlation between PFC concentration and tension value were found. It is hypothesized that PFP vapor adsorbed to the water surface during the experiment. To provide support, quartz crystal microbalance (QCM) was used to measure the amount of PFP adsorbed to the water surface.

4.2 Introduction

Perfluoropentane (PFP) consisting of 5 carbon molecules saturated with fluorine is part of the PFC family. Such molecules are considered biologically inert and have negligible toxicity.[1] PFP also has a unique boiling temperature of 29°C which is below normal human body temperature and above room temperature.[2] This property

provides the ability to form nano/microbubbles in the human body which have useful applications. One application is using them as a contrast agent in ultrasonography (Figure 4.1).[3–6] This is due to the substantially higher echogenicity of nano/microbubbles when compared to tissue and plasma, mainly caused by the compressibility and density difference between the nano/microbubbles and tissue.[5] Another application being derived from the previous example is controlled drug delivery and allowing the use of ultrasonography for monitoring the location of the drug and for controlling the release of the drug being transported by the nano/microbubbles.[7–9]

Although PFCs received a lot of interest, very little is known about their interfacial properties, especially of PFP and water. This is crucial in predicting the stability of nano/microbubbles in the human body which is one of the biggest limitations of their use for imaging and controlled drug delivery applications.[10] Previous work investigated the interface between water and air saturated with PFP vapor.[11] Such interface presented an inverted model of the interface present between a nano/microbubble and blood. A substantial decline in surface tension of water was observed when being exposed to PFP vapor. A similar effect was observed when water was exposed to perfluorohexane (PFH) vapor. Further investigation provided another finding of a linear relation between surface tension of water and PFP or PFH concentration in the vapor phase. To our knowledge, such correlation was not reported prior to our work. However, another observation was also made when allowing water to be exposed to PFP for longer periods of time. In some instances a second droplet (lens) would form at the apex of the water drop. This was also observed by Javadi et al. when water was exposed to alkane vapors.[12] This piqued our interest to take a step forward and

investigate this lens formation. We will first introduce the experimental setup, continue with the results obtained and discuss with supportive data.

4.3 Experimental Setup

4.3.1 Materials and Tensiometry

PFP and PFH of research grade were purchased from Fluoromed (Round rock, TX). PFP was kept in a refrigerator at 1^{o} C in a sealed container. Sealed containers of deionized water and PFH were kept at room temperature (maintained at 20°C). A custom pendant-drop tensiometer was used to provide the capability for continuous, near real-time surface tension measurements.[11] Figure 4.2 provides the main steps involved in a single surface tension measurement. The apparatus consisted of an air-tight cuvette in which a pendant drop of a liquid was introduced. The drop was imaged with a 1024x768 pixel resolution camera (Imaging Source, Charlotte, NC) fitted to an objective with an adjustable optical zoom in the range of 6–24x magnification. The typical magnification was 10x, selected to maximize the number of pixels representing the drop in the camera's field of view. A stainless steel syringe needle with a 2 mm diameter was used for formation of the droplet in a plastic cuvette (10mm x 10mm x 4.5mm).

4.3.2 Quartz Crystal Microbalance

A 5 MHz QCM200 (Stanford Research Systems, Inc, Sunnyvale, CA) instrument was used for all mass measurements. Specific for 5 MHz frequency, polished quartz crystals with 1 inch diameter and titanium/gold electrodes were used for the QCM instrument. The RS-232 port was connected to a desktop computer (HP Z400 Work-station) and LabVIEW stand-alone application was used for data acquisition. The

compensation switch of QCM200 was set to hold and ten-turn dial to 8.0 (dry operation setting). Prior to introduction of water and perfluorocarbon vapor the frequency of oscillation was given 15 minutes to equilibrate.

4.3.3 Procedure

All experiments were conducted at room temperature (20°C) which was checked before and monitored throughout the experiments. The surface tension was measured by first injecting 300 μL of PFC and 300 μL of water into individual containers made inside the cuvette, closing the cuvette and ensuring no leakage to allow the cuvette eventually become saturated with PFC and water vapor. To allow complete saturation of the cuvette with PFC and water vapor and avoid condensation due to temperature gradients, 15 minutes were allowed before the introduction of the pendant drop of water. A pendant drop of water was then formed at the end of a stainless steel syringe needle (1.6/2.09 mm inside/outside diameter) inside the sealed cuvette and measurements were started and monitored in real time by the tensiometer. To minimize any possible condensation above the drop, the syringe was inserted such that a minimum amount of stainless still is exposed to the vapors inside the cuvette. The volume and surface area of the drop were monitored to ensure no evaporation is taking place. Figure 4.3 shows a schematic of the experimental procedure. The data were saved and data processing done in Excel.

4.4 Results

After the formation of the droplet, the surface tension measurements appeared to be similar to results obtained in the previous study when the linear relation between the concentration of PFC in the vapor phase and surface tension of water was found. Table

4.1 provides the results obtained by using the linear relation between PFC concentration and surface tension reported previously[11] and compared to experiments conducted in this study. For a period of time the surface tension experienced only a minor decline (1-2 mN/m). About 20 minutes after the formation of the pendant drop which was allowed to be exposed to air saturated with PFP vapor, the surface tension experienced a more drastic decline (Figure 4.4a).

A similar phenomenon was seen when the pendant drop of water was exposed to air saturated with PFH and water vapor but to a lower extent (Figure 4.5a). During the steep decline it was observed that a second drop would begin to grow (Figure 4.6). It can be seen that the decline in surface tension is more significant in the case PFP is used yet the time required for such second drop formation was similar when comparing PFP and PFH vapor. The second drop most likely consisted of the PFC being used in the experiment. The surface tension measurements for both PFCs were no longer accurate due to the formation of such second drop (lens) at the bottom of the water pendant drop leading to an irregular geometry and causing the Young-Laplace equation to fail when attempting to fit the theoretical shape. The growth of such lens was also noted from the increase in volume of the pendant drop (Figures 4.4b and 4.5b). Such lens would continue to grow until reaching a maximum size where the lens would no longer be able to stick to the water drop. This can be explained by weak molecular interactions between PFCs being used and water drop surface although water on the surface is present at higher energy.

4.5 Discussion

Javadi et al observed a similar result when exposing water to hydrocarbons using a similar experimental setup.[12] However, the study did not take into account several important factors that could be involved in the formation of the hydrocarbon lens. One effect could be the condensation of hydrocarbons on the metal surface of the syringe and movement down to the water droplet simply due to gravity when a thick enough hydrocarbon layer formed on the metal surface. Such effect was minimized in our study by avoiding the syringe to be exposed to the vapor inside the cuvette. The possibility of condensation of PFC vapor on the surface of the syringe was observed when conducting an experiment where a clean syringe that was exposed to nitrogen gas prior was inserted inside the cuvette and exposed to the PFC vapor. Such experiment was repeated 6 times for insurance. Figure 4.7 shows the formation of a PFP layer on the stainless steel surface after being exposed for ~30 minutes. This was also confirmed by inserting the syringe at a higher temperature (~40^0 C) to confirm that the formation PFP layer on the metal was not due to a temperature gradient leading to condensation. This provided support that such formation could be involved in the formation of the lens but was avoided in our experimental setup.

The second important parameter is the temperature gradient that may be present due to the humidity inside the cuvette. If the cuvette was not allowed to become saturated with water vapor, this could cause condensation of PFC vapor due to the temperature gradient. This was previously investigated and found that 10 minutes is enough time for the cuvette to become saturated with water vapor under the experimental conditions being

sed by us. This led us to the conclusion that condensation was less likely the reason for lens formation.

To better understand the formation of the lens, we further investigated the interaction between water and PFP vapor. One hypothesis was that although previous reports consider PFP and water immiscible there could still be some absorption of PFP occurring. To investigate this hypothesis we have conducted experiments by using a Fourier Transform Infrared Spectrometer (FT-IR) (Nicolet iS10, Thermo Scientific, Waltham, MA). The first setup used is shown in Figure 4.8. Two cuvettes were connected by a tube to allow vapor to diffuse from one sealed plastic cuvette to another. After injecting 300μL of water to one cuvette, the absorbance was collected and subtracted as a background. Then, 500μL of PFP was injected into the second cuvette and absorbance of water was made over time. The measurements were done up 3 hours after introduction of PFP. The results obtained showed no change in absorbance.

For comparison, a second setup was used (Figure 4.9). First, 300μL of water was introduced inside the cuvette and absorbance measured. By carefully adding a small amount of PFP (~50 μL) on the water surface allowed it to stay above the water due to the water surface tension. The absorbance was then measured by using FT-IR 3 hour after introduction of PFP. This setup also showed no change in absorbance after adding the PFP liquid. Both cases are most likely due to the limit of detection of the FT-IR that is dependent on the signal-to-noise ratio. Kabalnov et al. used Ostwald ripening kinetics to calculate the solubility of PFP and PFH in water to be $4.0\text{x}10^{-6}$ mol/L and $2.7\text{x}10^{-7}$ mol/L (at 25^0 C), respectively.[13] Such negligible values support the hypothesis that FT-IR was simply not able to sense the change in absorbance. To further see if such

solubility had any effect on the formation of the lens, we conducted similar experiments of monitoring surface tension, surface area and volume by varying the size of the pendant drop and estimating the time of the lens formation. For each size of the pendant drop at least 5 experiments were conducted for statistical purposes. Figure 4.10 shows the results obtained in terms of the average surface area (a) and volume of the droplet (b). Figure 4.11 provides the average time needed for lens formation with respect to the surface-area-to-volume ratio. The results show that surface area, volume, or surface-area-to-volume ratio does not have a significant effect on the time needed for the lens formation. However, it can be seen that there may be a possibility of shorter time that is required to saturate a pendant drop with a higher surface-area-to-volume ratio but more accurate measurements will be needed. In the future, we are considering investigating the geometric effect on the saturation of water with PFCs by modeling the experiments conducted in this study.

This led us to the hypothesis that most likely adsorption of PFP from the gas phase to the water surface was taking place. To estimate the amount of PFP being adsorbed to the water surface, a quartz crystal microbalance (QCM200, SRS) was used. A water bubbler was connected to a chamber by tubing to control humidity and a hygrometer placed inside the chamber to monitor humidity (Figure 4.12). QCM200 with the QCM cell was placed inside the chamber. The input of the QCM cell was connected to the cuvette by a tube which will allow PFP vapor to enter the chamber and output of the QCM cell being exposed to the environment of the chamber where humidity is being controlled. Initial humidity was measured and was found to be ~25-30% before the experiments were conducted. A new 5MHz Quartz Crystal with gold surface was used for

the measurement and LabVIEW software used to record the frequency change throughout the experiment. The valve of air source was opened and time was allowed for the humidifier to raise the humidity inside the chamber. The humidity of 90-95% was allowed to be reached and the frequency change is shown in Figure 4.13. To calculate the amount of water adsorbed to the gold surface, the Sauerbrey equation was used with the sensitivity factor of the crystal being $56.6\ \frac{\text{Hz cm}^2}{\mu\text{g}}$. The decrease of ~5.5 Hz represents mass density of $9.72\text{x}10^{-8}\ \frac{\text{g}}{\text{cm}^2}$ and a minimum of 3 monolayers (0.825 nm) of water molecules present on the gold surface by assuming the monolayer capacity of $3.10\text{x}10^{-8}\ \frac{\text{g}}{\text{cm}^2}$.[14] This calculation did not take into account the surface roughness of gold which will result in a higher amount of monolayers from the calculation. PFP was then injected inside the cuvette to allow PFP vapor to enter the QCM cell and caused a further decrease in frequency (~12 Hz) (Figure 4.13). This accounted for the $2.12\text{x}10^{-7}\ \frac{\text{g}}{\text{cm}^2}$ mass density of the adsorbed PFP molecules now adsorbed to the layer of water.

To confirm the results obtained when using the crystal with the gold surface, a modification was done to make the surface more hydrophilic. The gold surface was exposed to 0.1mM mercaptododecanoic acid overnight (Figure 4.14). The experimental procedure of introducing water and PFP vapor was the same as the one described previously. As expected, a substantially higher amount of water vapor adsorbed to the mercaptododecanoic acid modified gold surface. This continuing decline was most likely due to the carboxylic acid layer causing more water to be adsorbed after saturation of the chamber with water vapor. The minimum amount of water that adsorbed was calculated to be ~9 monolayers (2.5 nm) with mass density being $2.70\text{x}10^{-7}\ \frac{\text{g}}{\text{cm}^2}$ (Figure 4.15).

After the injection of PFP into the cuvette, the frequency declined by an amount close to the one presented in Figure 4.13 giving mass density of $2.37\text{x}10^{-7}\,\frac{\text{g}}{\text{cm}^2}$.

The results of QCM experiments provide support that PFP does in fact adsorb to the water surface similar to hydrocarbons as was reported previously by others.[12,15] Although here it appears that the amount of PFP being adsorbed reaches a maximum, it must be noted that PFP is not able to stay on the water surface especially on the side of the pendant drop due to weak molecular interaction. This weak interaction causes PFP to move down the pendant drop of water due to gravity, eventually forming the lens.

4.6 Conclusion

Exposure of the water drop to air saturated with PFP or PFH vapor for long periods of time caused a steep decline in surface tension due to the formation of the lens at the apex and the Young-Laplace equation was no longer able to fit theoretical shape of the drop. Negligible solubility of PFP in water which was seen by FT-IR and confirmed by previous research in this area, the molecules were most likely adsorbing to the water surface. This hypothesis was confirmed by conducting experiments with QCM. Weak molecular interaction between PFP and water caused PFP to form the lens and eventually detach from the surface of the water drop. This project provided better understanding of PFC/water interface and allows taking a step forward in designing nano/microbubbles used for therapeutics with better stability and ability to control drug and gene release for medical treatments.

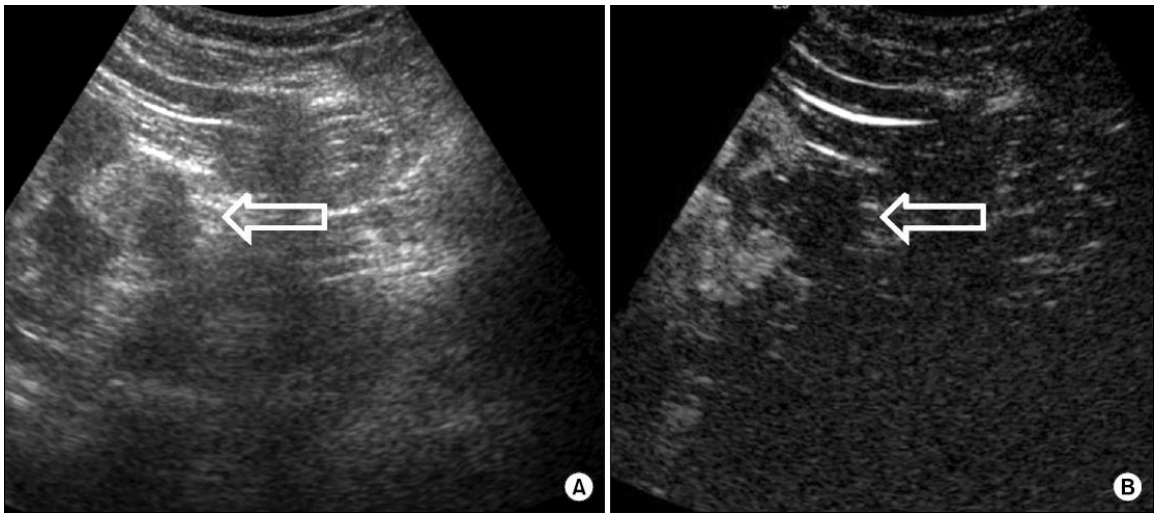

Figure 4.1: Angiomyolipoma of a 56-year-old man. (A) Conventional ultrasonography showing a hyperechogenic mass with a 2.3 cm diameter located in the left lower kidney. (B) Ultrasonography in the same location but with application of nano/microbubbles as contrast agent. Figures adapted from.[3]

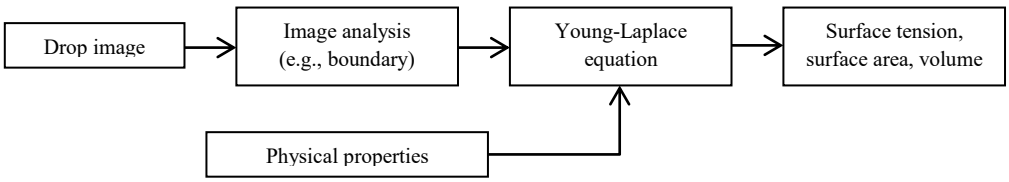

Figure 4.2: Method used for measurement of dynamic surface tension.

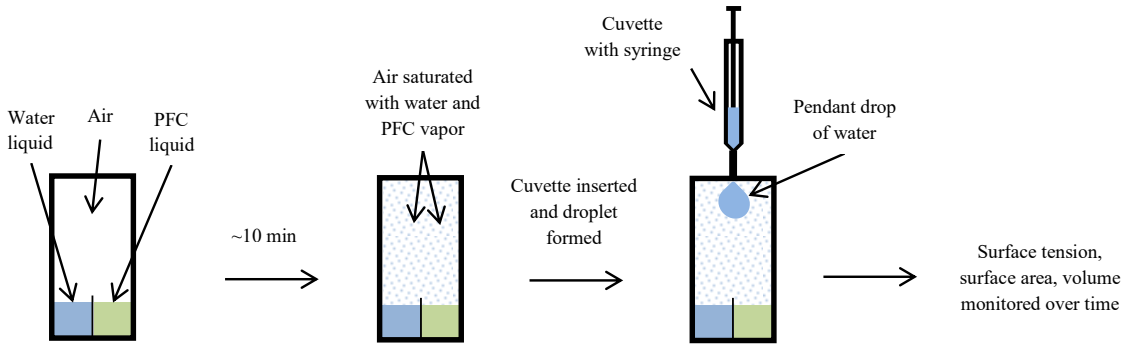

Figure 4.3: Experimental procedure used in this study.

Table 4.1: Surface tension (mN/m) of water in air saturated with perfluorocarbons.

Sample	Linear relation	Presaturated experiment
PFP	64.0	63.4±0.748
PFH	65.9	65.0±0.420

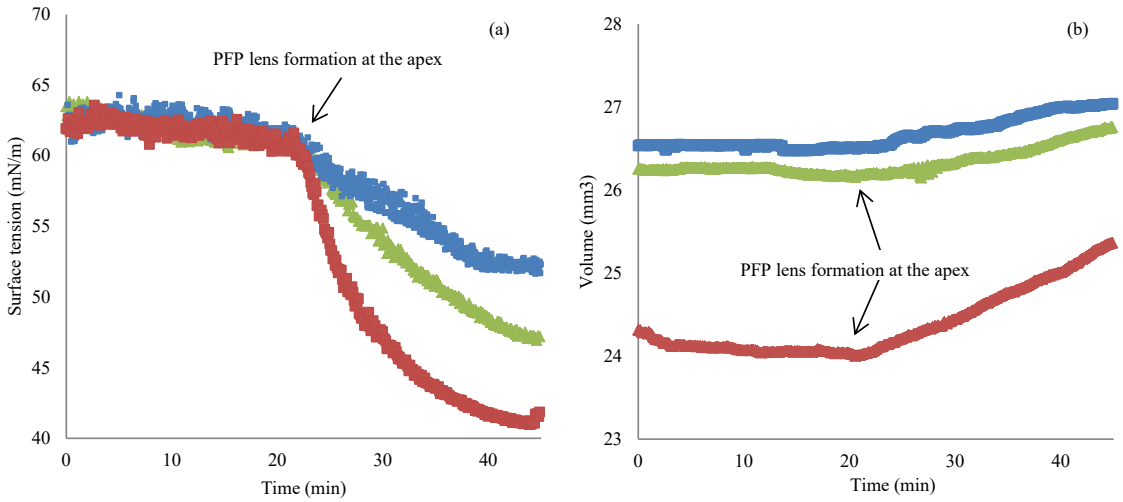

Figure 4.4: Exposure of pendant drop of water to air saturated with PFP vapor (a) Dynamic surface tension (b) Change of volume with time.

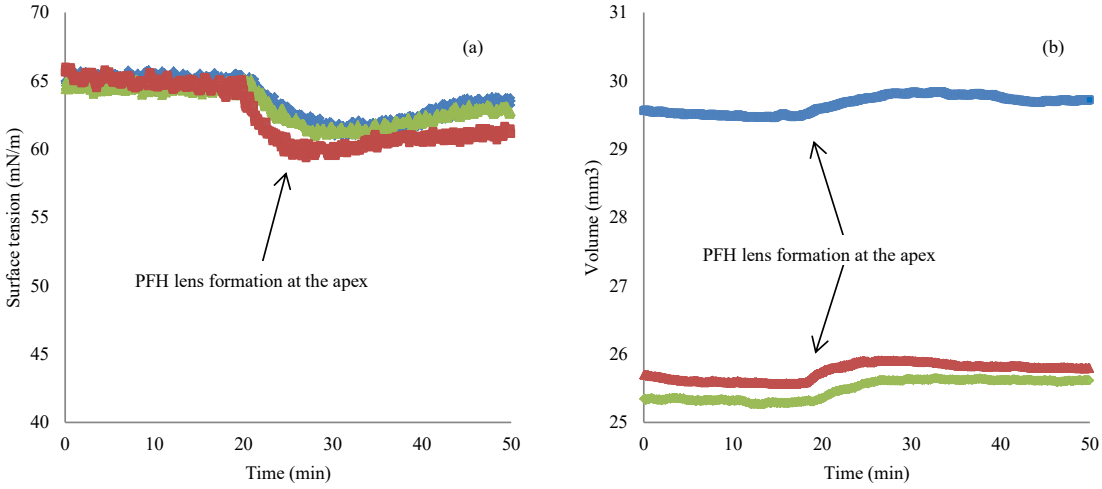

Figure 4.5: Exposure of pendant drop of water to air saturated with PFH vapor (a) Dynamic surface tension (b) Change of volume with time.

Figure 4.6: Formation of PFP lens at the apex of the water drop (red arrow).

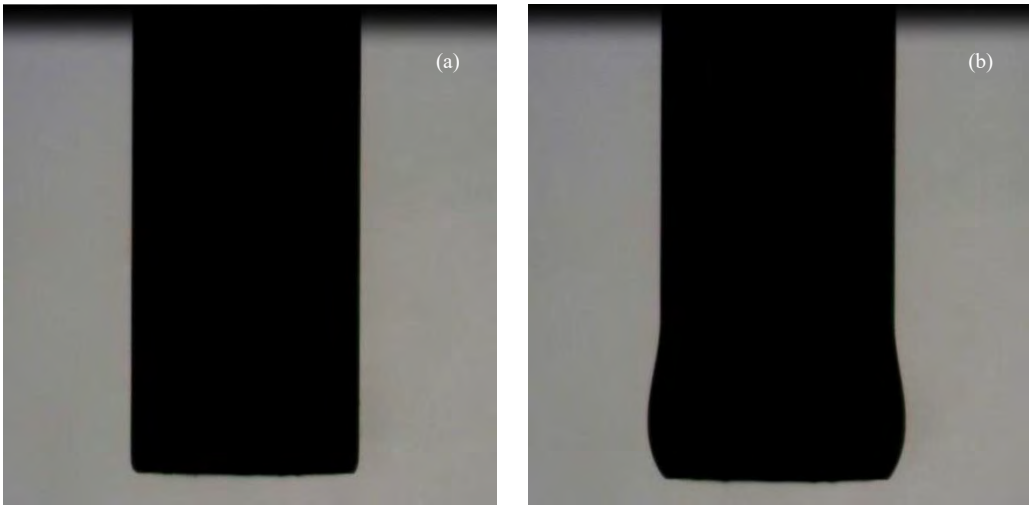

Figure 4.7: Adsorption of PFP vapor on stainless steel surface. (a) Syringe inserted into the cuvette saturated with PFP vapor. (b) Accumulation of PFP being adsorbed to the stainless steel surface.

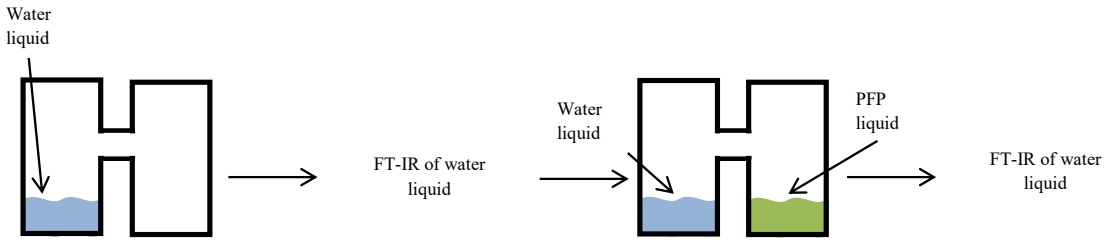

Figure 4.8: First setup used to measure absorption of PFP into water.

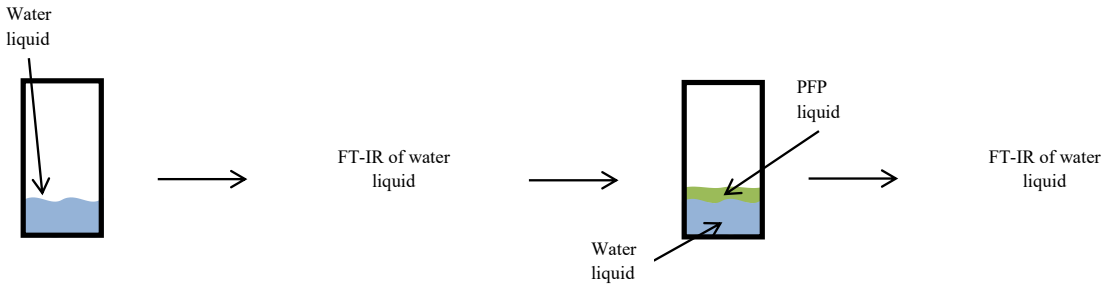

Figure 4.9: Second setup used to measure absorption of PFP into water.

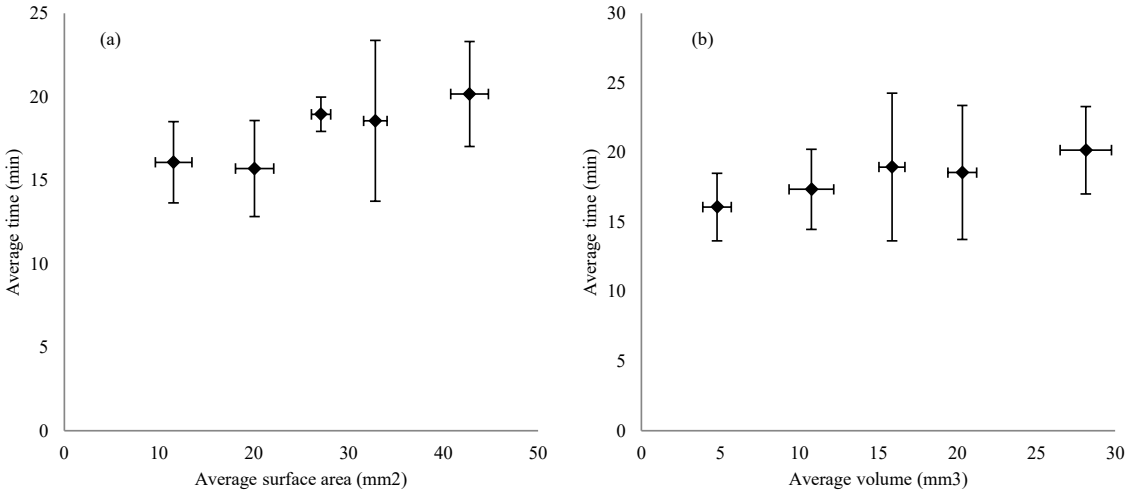

Figure 4.10: The effect of surface area and volume on time of lens formation. (a) Surface area of the water pendant drop and the average time until the formation of the PFP lens. (b) Volume of the water pendant drop and the average time until formation of the PFP lens.

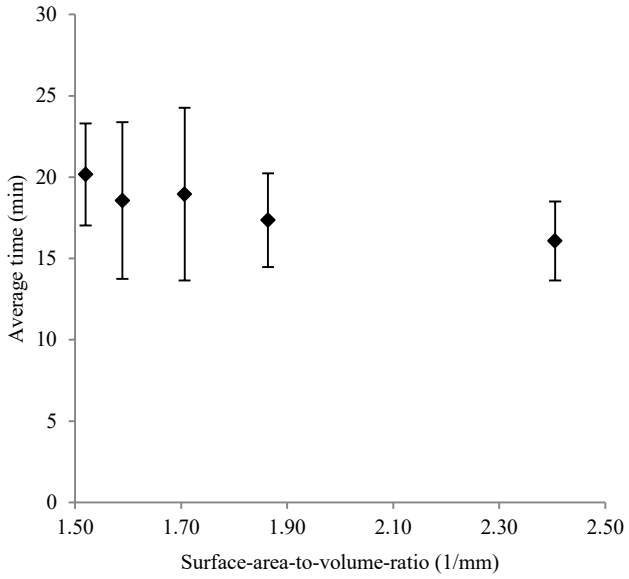

Figure 4.11: The effect of surface-area-to-volume-ratio of the pendant drop on the time of lens formation.

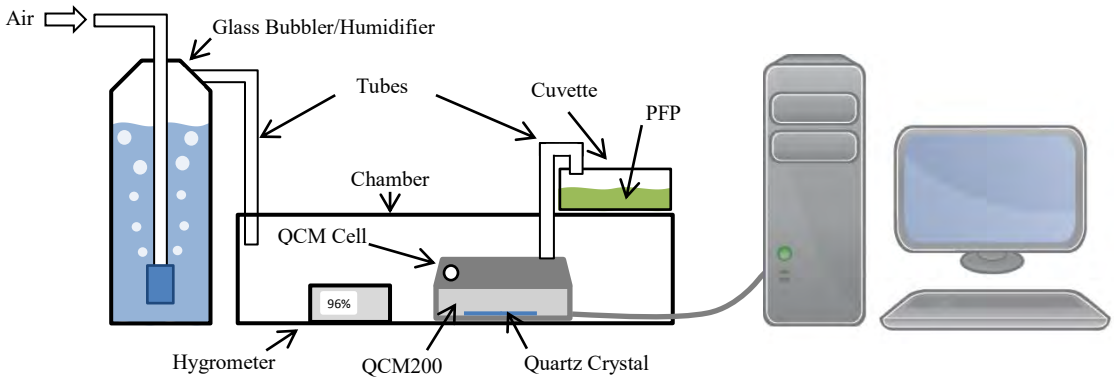

Figure 4.12: QCM setup for estimation of the adsorbed PFP to the water surface.

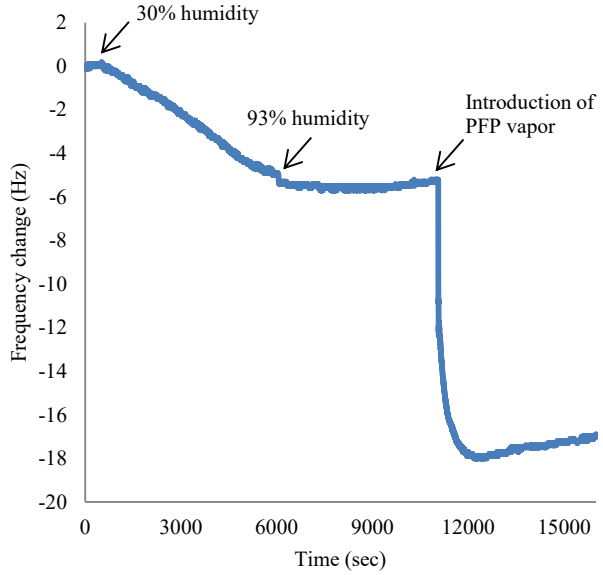

Figure 4.13: Adsorption of water on the gold surface followed by adsorption of PFP on the water surface.

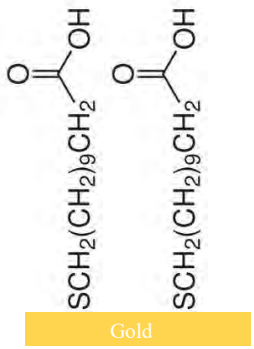

Figure 4.14: Modification of the gold surface with mercaptododecanoic acid.

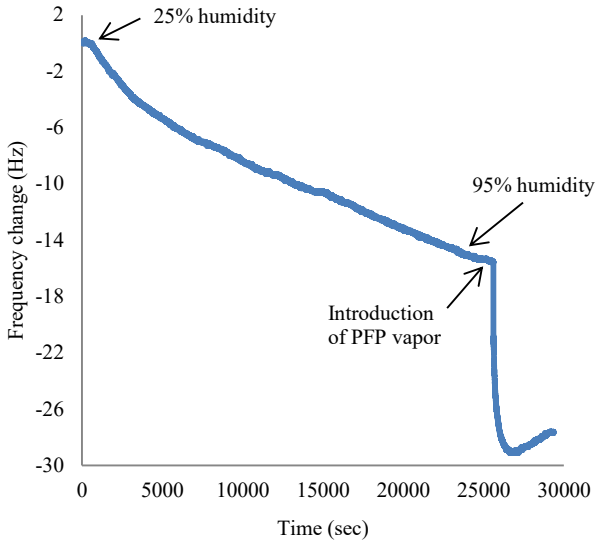

Figure 4.15: Adsorption of water vapor on the mercaptododecanoic acid modified gold surface and adsorption of PFP on the water surface.

4.7 References

1. Strohm, E., Rui, M., Gorelikov, I., Matsuura, N. & Kolios, M. Vaporization of perfluorocarbon droplets using optical irradiation. *Biomed. Opt. Express* **2,** 1432–1442 (2011).

2. Fang, J. Y., Hung, C. F., Liao, M. H. & Chien, C. C. A study of the formulation design of acoustically active lipospheres as carriers for drug delivery. *Eur. J. Pharm. Biopharm.* **67,** 67–75 (2007).

3. Oh, T. H., Lee, Y. H. & Seo, I. Y. Diagnostic efficacy of contrast-enhanced ultrasound for small renal masses. *Korean J. Urol.* **55,** 587–592 (2014).

4. Albrecht, T. *et al.* Non-invasive diagnosis of hepatic cirrhosis by transit-time analysis of an ultrasound contrast agent. *Lancet* **353,** 1579–1583 (1999).

5. Baert, A. L. & Sartor, K. *Contrast Media in Ultrasonography: Basic Principles and Clinical Applications* (Springer Science & Business Media, 2005).

6. Schneider, M. *et al.* BR1: a new ultrasonographic contrast agent based on sulfur hexafluoride-filled microbubbles. *Invest. Radiol.* **30,** 451–457 (1995).

7. Deckers, R. & Moonen, C. T. W. Ultrasound triggered, image guided, local drug delivery. *J. Control. Release* **148,** 25–33 (2010).

8. Hernot, S. & Klibanov, A. L. Microbubbles in ultrasound-triggered drug and gene delivery. *Adv. Drug Deliv. Rev.* **60,** 1153–1166 (2008).

9. Liu, Y., Miyoshi, H. & Nakamura, M. Encapsulated ultrasound microbubbles: therapeutic application in drug/gene delivery. *J. Control. Release* **114,** 89–99 (2006).

10. Sirsi, S. R. & Borden, M. A. Microbubble compositions, properties and biomedical applications. *Bubble Sci. Eng. Technol.* **1,** 3–17 (2009).

11. Chernyshev, V. S. & Skliar, M. Surface tension of water in the presence of perfluorocarbon vapors. *Soft Matter* **10,** 1937–1943 (2014).

12. Javadi, A., Moradi, N., Möhwald, H. & Miller, R. Adsorption of alkanes from the vapour phase on water drops measured by drop profile analysis tensiometry. *Soft Matter* **6,** 4710–4714 (2010).

13. Kabalnov, A. S., Makarov, K. N., Shcherbakova, O. V. & Nesmeyanov, A. N. Solubility of fluorocarbons in water as a key parameter determining fluorocarbon emulsion stability. *J. Fluor. Chem.* **50,** 271–284 (1990).

14. Lee, S. & Staehle, R. W. Adsorption of water on gold. *Corrosion* **52,** 843–852 (1996).

15. Kwon, O., Jing, H., Shin, K., Wang, X. & Satija, S. K. Formation of n-alkane layers at the vapor/water interface. *Langmuir* **23,** 12249–12253 (2007).

CHAPTER 5

SURFACE ACTIVITY OF EXOSOMES

5.1 Abstract

Dynamic surface tension (DST) is a method that is widely used for characterization of surfactants and nanoparticles. However, DST has not been applied to characterize exosomes. In this chapter, the discovery of surface activity of exosomes is presented. This finding allows the application of DST for determining concentration and potentially size of exosomes in a given sample. It also provides the potential mechanism of exosome adsorption to the cell membrane and release of its content.

5.2 Introduction

Exosomes are membrane-bound nanovesicles found in all biological fluids.[1,2] They contain molecular cargo of nucleic acids, proteins, and other compounds derived from the parent cell and are released via an endocytic pathway.[2–4] Exosomes have been found to be very stable and after their release into circulation serve as messengers for short and long-range intercellular signaling by fusing with the target cells and releasing their contents.[5,6] The stability of these vesicles in the blood, urine, saliva and breast milk allows their extraction and characterization which can include their size, concentration, content and other properties which can potentially be used for medical diagnostics.[7] It has already been shown that exosomes contain noncoding RNAs such as microRNAs that

vary in their abundance in the blood when comparing normal individuals and those with cancer.[8–10] Cancer cells *in vitro* were also found to increase the release of exosomes and contain microRNAs specific to their environment such as hypoxia and low pH.[11] This shows that the concentration of exosomes will in the future become a critical parameter that will allow differentiation of a normal sample from a sample that is acquired from a patient. However, exosome size (20-120nm) greatly limits the techniques that can be used for measurements of the particle concentration. ELISA assays are protein specific and can only determine the number of exosomes containing a specific marker, such as CD63, CD9 or CD81. It was found that such markers are not necessarily present in all exosomes[12] which can lead to underestimation of exosome concentration in a sample and potentially lead to false conclusions. Nanoparticle tracking analysis (NTA) is currently the most widely used method for estimation of not only the particle concentration but also their size distributions.[7,13] However, the narrow field of view that is used to conduct measurement using NTA (e.g., Nanosight LM10) permits analysis of only 30-80 particles from which the concentration estimation is made. The measurement is based on Stokes-Einstein equation that assumes the particles to be spherical. In addition, the model does not take into account other parameters such as surface decoration as well as ions present in the solution that may affect particle diffusivity. Background particles that may be present in the sample which are not exosomes may also contribute to deviation from the real concentration and size distribution. The tunable resistive pulse sensing (TRPS) method which uses pulses of current occurring due to particles passing through a nanopore and decreasing the flux of ions is another technique that is available for exosome size and concentration measurements.[14] The drawback of such a technique is the

use of a specific nanopore which allows only a narrow size distribution of particles to pass. This does not allow including the particles that are out of the size range for which the chosen nanopore can be applied. In addition, some aggregates present in the sample can easily cause clogging of the nanopore which will require cleaning and repeating measurement of the sample and standard bringing the need for more analysis time. Although the amount of particles used to calculate concentration and size distribution is larger than NTA (>500 particles), it is still a statistical limitation of TRPS. This shows that determining exosome concentration still remains a challenge as pointed out previously.[15] Such disadvantages provided motivation to develop an alternative method for measuring exosome concentration in a given sample.

Dynamic interfacial tension method is one that is commonly used for estimation of concentration and diffusion coefficients of surfactants. The discovery that surface tension equilibrium during presence of surface active molecules is in fact not reached instantly when interface is formed goes back to 1869 when Dupré presented the surface tension of a soap solution with fresh surface tension to be different from the equilibrium value.[16] This was later noted by Rayleigh studying dynamics of soap solutions by applying the oscillating jet method and by Gibbs theory of capillarity;[17–19] however it was not until the beginning of the 1900s that dynamic surface tension was proposed. Milner was able to measure dynamic surface tension and proposed that the interface is formed by the diffusion of surfactant from the bulk to the surface.[20] Numerous techniques were explored to measure the surface tension change with time, such as Langmuir balances and electric potentials.[21] Some quantitative descriptions of dynamic surface tension were also attempted using a diffusion model.[22–25] The quantitative model for surfactant adsorption

only by diffusion later contributed by Ward and Tordai became the core for other models and is commonly applied today for determination of concentration and diffusion coefficient of surface active solutes.[26] Recently, the dynamic interfacial tension method was applied not only to characterize short chain molecules including solutes that are not common surface active solutes[27] but also surface active nanoparticles. Gupta and Rausseau developed surface-active lipid nanoparticles (SLNs) with 152nm diameter to stabilize oil-in-water emulsions.[28] They were able to show that the particles were wetted by both the aqueous and oil phases and preferentially positioned themselves at the interface. Lui et al. presented a preparation method of gold nanoparticles with hydrophobic and hydrophilic polymer brushes that migrate to the oil/water interface and decreasing the size of oil droplets.[29] Bizmark et al. recently studied adsorption-driven self-assembly of nanoparticles at fluid interfaces by using synthesized nanoparticles with 89nm and 42nm in diameter.[30] Dynamic surface tension measurement of nanoparticle solutions provided a potential of measuring energy of adsorption, adsorption rate constant and energy of particle-interface interaction at different amounts of surface coverage. Rana et al. studied dynamic interfacial tension of gold nanoparticles with monolayer ligand shells as well as nanoparticle-protein complexes and reported the effect of ligand/protein hydrophobicity on the interfacial assembly.[31] Although the composition of exosomes is still being explored, they are known to contain transmembrane proteins and complexes such as CD9, CD3, CD81, sodium/potassium-transporting ATPase α-1, α-2 and α-3,[32] LAMP-1/2, MHC[33] and others,[7,34,35] yet there are currently no reports about the potential of their surface activity. In addition to phospholipid membrane of exosomes, proteins are well known to be surface active[36] which may allow determination of

exosome concentration and potentially size in a sample using dynamic surface/interfacial tension analysis. In addition, the flexibility of experimental conditions where dynamic surface/interfacial tensiometry can be applied may allow modeling of exosome transport, their adsorption to the cell surface followed by fusion and release of content. Here we present our study of exosome surface activity and its application.

5.3 Proposed Method and Implementation

5.3.1 Cell Line Exosomes

MDA-MB-231, MCF7 and MCF10a breast cancer cell lines, PC3, PCS, LNCap and 22Rv1 human prostate cancer cell lines prior to cell culture were stored in liquid nitrogen. For cell culture the cell line was thawed and plated on 150 mm plates. Table 5.1 provides the media used for each cell line. Once the cells settled down, the media was changed (approximately 24 hours after plating). The plate was then split at 1:10 ratio and 10 plates were cultured. Each plate contained 20 mL of media. Media from 9 of these plates (180mL) was harvested and pooled. Media was then split into 30 ml/tube and centrifuged at 3000×g for 15 minutes. The supernatant was transferred to a new sterile 50 mL tube for each. Exosomes were isolated by using the ExoQuick TC technique (System Bioschiences, Mountain View, CA, USA). In short, 6mL of ExoQuick TC reagent was added to each 30 mL supernatant and left for overnight incubation at 4°C. On the next day, the mixture was centrifuged at 1500×g for 30 minutes at room temperature. After centrifugation, the exosomes would appear as a beige pellet. The pellet obtained from 6 of these 30mL media was resuspended in 1x phosphate buffered saline (PBS) to obtain 2700 µL of resuspended exosomes. The resuspended exosomes were then separated into 100 µL aliquots and stored in 1 mL tubes at -80°C until use.

5.3.2 Serum Exosomes

Seven 1 mL serum samples obtained from different patients were provided by ARUP Laboratories (Salt Lake City, UT, USA) and deidentified according to IRB protocol. Exosomes were isolated from serum using an ExoQuick kit (System Biosciences, Mountain View, CA) following manufacturer's instructions. Briefly, serum was centrifuged at 3,000×g for 15 minutes to remove cells and cell debris. The supernatant was transferred to a sterile vessel and 252 μL of ExoQuick was added. The mixture was refrigerated for 30 minutes and then centrifuged at 1500×g for 30 minutes at room temperature. After centrifugation, the supernatant was discarded and the exosome pellet saved. To spin down the residual ExoQuick solution, the pellet was centrifuged for another 5 minutes at 1500×g and the supernatant was removed without disturbing the pellet. The pellet was then resuspended in 200 μl of 1x PBS buffer and stored in a 1 mL tube at -80°C until use.

5.3.3 Surface Tension Measurement

Surface tension can be measured using various methods such as Du Nouy-Padday pull method,[37] bubble pressure,[38] sessile[39] or pendant drop methods.[40] After the exposure of the interface to the analyte in question, the interface tension will change with time due to the change in its composition as the analyte migrates to the interface. Assuming a linear relation between interfacial tension and logarithm of the analyte concentration, the concentration of the analyte can be found if surface tension is known. Due to ease and reliability of the pendant drop method in finding interfacial tension, we proposed its implementation for determination of exosome concentration in a sample. Prior to the surface tension measurement, the exosome sample stored at -80°C was thawed at 4°C.

When the sample reached the liquid state, it was diluted to appropriate concentration in the 1x PBS buffer used for exosome pellet resuspension described above. A pendant drop of 24-26 mm^3 volume was then created using the diluted exosome sample at the end of a stainless steel syringe needle (1.6/2.09 mm inside/outside diameter) placed inside a sealed cuvette containing air and maintained at 20°C room temperature in the laboratory located ~1470 m above sea level. Measurements of the pendant drop surface tension, volume and surface area were then started immediately using a custom real-time tensiometer developed by us.[27] The surface tension measurement was stopped at least 4 hours after the formation of the drop. The measurement for each sample was repeated 4 times. The surface tension change with time data was saved from the start until the end of the measurement and analyzed after its completion.

5.3.4 Concentration Measurement

Concentration was determined using Nanosight instrument (model LM10; Salisbury, United Kingdom) by illuminating the sample with a 40 mW violet laser (405 nm wavelength), capturing the light scatted by exosomes with a high-sensitivity sCMOS camera (OrcaFlash2.8, Hamamatsu C11440), and analyzing the results using the software provided by the manufacture (Nanosight Version 2.3). The minimal expected particle size, minimal track length, and blur size were set to Auto, gain set to 1, brightness to 0, and detection threshold set to 10 Multi. The viscosity of 1x PBS was assumed to be equal to viscosity of water which depends on temperature and was adjusted automatically based on the temperature measurements. Temperature of the cell was measured manually and remained at 20°C with a maximum of 0.1 degree fluctuation throughout the nanoparticle tracking. Viscosity of water at these temperatures is nearly constant and equal to 1cP.

Prior to analysis, the exosome samples were diluted to appropriate concentration (e.g., 1:100 and up to 1:2,000) in 1x PBS and allowed to equilibrate to room temperature (20°C). Samples were analyzed within 5 minutes of the initial dilution. Using a 1 mL sterile syringe, each sample was injected into the test cell. Approximately 30-100 particles were observed in the field of view and the typical concentration was approximately $4 - 12 \times 10^8$ particles/mL for each measurement. A set of 60-second videos was recorded for each sample at 19.96 frames per second with 22.98 ms shutter speed and camera gain set to 475 and analyzed using NTA software with the described settings. Each video consisted of more than 1000 frames and the total of valid particle tracks for each 60-second measurement was more than 1200. The video data characterizing hydrodynamic mobility of particles in the field of view were analyzed with the NTA software which reported the exosome concentration, size distribution, its mode, mean and the standard deviation. Each sample was measured at least 3 times.

5.3.5 Environmental Scanning Electron Microscopy (ESEM)

One exosome sample obtained from serum was diluted 1:100 in DI water, 10 μl of the sample placed on the aluminum sample holder and imaging was performed using FEI Quanta 600 FEG under ESEM mode. Gaseous back-scattered electron detector (GBSD) was used at magnification in the 40,000-400,000x range at 30kV and temperature of 5-6°C.

5.4 Results and Discussion

Table 5.2 provides the summary of concentration and size results for exosomes isolated from sera and cell lines. The hydrodynamic mode and mean size of exosomes

extracted from serum were calculated to be 103 ± 21 nm and 130 ± 26 nm, respectively, which were noticed to be smaller than mode and mean size of exosomes extracted from cell lines, 130 ± 13 nm and 183 ± 25 nm, respectively. A difference in size when comparing normal and cancer exosome populations was previously noted by Sharma et al. when comparing exosome dimensions present in saliva of healthy and oral cancer donors and reported the patient with oral cancer to contain a larger average size.[41] Baran et al. also reported the size distribution of exosomes coming from gastric cancer patients to be very dispersed and it can be observed from their results that the mode is considerably larger in these samples.[42] The difference in size in our study is seen even with presence of two outliers in each group, serum sample (#7) and PCS cell line. In addition to size, serum sample #7 also contained a higher concentration of exosomes when compared to other samples. Interestingly, after patient's #7 blood sample was taken and analyzed, the patient was considered healthy. The possible cause of this sample to be a clear outlier will be further investigated in our future study.

Surface tension of each sample was measured after conducting a specific dilution. Initially, the surface tension appeared to be close to surface tension of 1x PBS (~73 mN/m) but after a short time the surface tension of all samples used in this study was dynamic and varied significantly from sample to sample especially after 4 hours of pendant drop formation (Figure 5.1). One serum (#1) and one cell line sample (22Rv1) were chosen to also observe the change in surface tension with respect to dilution factors (no dilution to 1:1 million dilution) while other samples were analyzed at a set dilution factor (1:100 or 1:1000) with each surface tension measurement repeated 4 times. It can be seen that the surface tension 4 hours after pendant drop formation and natural

logarithm of exosome concentration in the chosen samples analyzed at different dilutions overlap well with samples that were independently measured at a set dilution factor (Figure 5.2). Interestingly, a linear correlation between surface tension 4 hours after pendant drop formation and logarithm of exosome concentration is observed in both serum and cell line samples. Error bars in Figure 5.2b show the standard deviation of surface tension value after 4 hours of drop formation. This observation is convincing and shows that exosomes are surface active and behave as surfactants. Such linear correlation is not the same when comparing serum and cell line sample groups. Cell line samples appeared to contain other highly surface active impurities present after exosome extraction such as proteins that are included in culture media and well known to be surface active.[36] For example, the dynamic surface tension of the original undiluted exosome free culture media used for 22Rv1 was measured to be ~50 mN/m after 4 hours while its initial surface tension was measured to be ~65 mN/m. The presence of impurities could have introduced the sharp initial decrease in surface tension that is shown in Figure 5.3 forming a barrier at the surface and leading to not as large a decrease in surface tension at the same exosome concentration when compared to serum samples. Exosome size could also contribute to this difference, since the hydrodynamic size of exosomes is larger in cell line samples when compared to sera samples and a smaller amount of these particles can occupy the surface. To investigate this hypothesis, a 100 kDa filter (Pall, Port Washington, NY) was used to remove particles below ~10nm from one serum sample (#1) and one cell line sample (22Rv1) using a standard protocol. In short, 500 µL of the sample was placed into the sample reservoir which was then capped and spun at 14,000g for 5 minutes. At the end of spin time, the centrifuge was stopped

and reservoir removed. The sample remaining was of ~10-20 µL volume, was resuspended in 1x PBS to make the total volume 500 µL and analyzed by using the NTA and tensiometer. Figure 5.4 shows the surface tension of the supernatant at each filtration step including final filtered exosome samples and Table 5.2 shows the concentration and size measurements of the final filtered samples measured by NTA. Sample 22Rv1 required three repetitions of filtration in order to remove the effect of other surface active molecules while the serum sample only underwent one filtration step and showed negligible amount of other surface active analytes as can be seen from background surface tension measurement (Figure 5.4b). After all filtration steps 22Rv1 exosomes also appeared to fit the correlation between surface tension and exosome concentration found for the serum samples (Figure 5.2b) supporting the hypothesis that sample impurities consisting of surfactants that are <10nm in size were the reason for the deviation between serum and cell line results and average size difference of exosomes extracted from cell lines and sera having a negligible effect.

ESEM analysis confirmed the presence of exosomes in close proximity to the liquid/air interface (Figure 5.5). The transport of exosomes to the liquid/air interface was also observed when using NTA by positioning the interface at the field of view (Figure 5.6a). Within 1 hour of particle tracking, the interface appeared to stay in the same location with evaporation, if occurring, being low. The velocity of exosomes to the surface after 1 hour of interface formation was estimated to be 2.12 µm/s and 2.66 µm/s corresponding to $3.56 \cdot 10^{-16}$ mol/m^{2}s and $3.35 \cdot 10^{-16}$ mol/m^{2}s molar flux for serum sample #1 and 22Rv1, respectively. Initial velocity of exosomes toward the interface appeared to be considerably higher than at later times (Figure 5.6b and c). This is an

expected result, since the flux to the surface will slow down as the surface coverage increases and concentration gradient decreases. Liquid/liquid interface was also observed by using perfluorohexane liquid, a substance that is immiscible in water or 1x PBS, instead of air. Although the migration of exosomes toward the interface was more difficult to observe as it appeared to occur significantly slower when compared to the liquid/air case, estimation for sample #1 and 22Rv1 was made and determined to be approximately 0.4 μm/s or 400 nm/s corresponding to $1.05 \cdot 10^{-16}\ \mathrm{mol/m^2 s}$. The difference between liquid/air and liquid/liquid flux to the interface could be contributed by a temperature gradient present in liquid/air case due to liquid evaporation although visual inspection of the surface led us to conclude that evaporation is negligible as mentioned earlier.

As discussed previously, it was shown by others that solid particles can adsorb at gas-liquid and liquid-liquid interfaces favored by thermodynamics and reducing the surface or interfacial tension.[30] Similarly to surfactants, such particles can stabilize "pickering" emulsions.[43] Such dependence may affect interpretation of the results obtained for exosomes, especially extracted from cell line samples that may vary in their surface content. This difference may affect surface tension change and under or overestimate exosome concentration; however, large deviations from the linear correlation was not observed. Error can also be contributed from NTA which may overestimate the concentration due to other particles present in the sample or underestimate due to the limits of laser diffraction.

This novel technique of exosome characterization can also potentially be used to approximate the size of exosomes based on their diffusivity obtained from the surface

tension dynamics.[30,44] To explore this, a classical reversible adsorption model was applied. The model contains two processes, Fickian diffusion of the surface active species from the bulk to the subsurface ($s < x < \infty$) and transport from the subsurface to the fluid/fluid or fluid/gas interface ($0 < x < s$). Assuming a one-dimensional model, absence of temperature gradients, absence of convection and reaction, having equal body forces and assuming a constant diffusion coefficient the general mass transfer equation can be simplified and applied for ($s < x < \infty$):

$$\frac{\partial c}{dt} = D\frac{d^2c}{dx^2} \tag{1}$$

with boundary and initial conditions:

$$c(x, 0) = c_0 \tag{2}$$

$$c(\infty, t) = c_0 \tag{3}$$

$$c(s, t) = c_s(t) \tag{4}$$

where c is the concentration of the species, c_s is the subsurface concentration that depends on time, t is time, D is the diffusion coefficient, x defines a location in the single dimension and s the location of the subsurface. The kinetic equation describing adsorption, desorption and accumulation of the species at the surface or interface can be expressed by

$$\frac{d\Gamma}{dt} = k_a g(\Gamma)c_s - k_d f(\Gamma) = k_a g(\Gamma)\left(c_s - \frac{k_d f(\Gamma)}{k_a g(\Gamma)}\right) = k_a g(\Gamma)(c_s - c_i) \tag{5}$$

where Γ represents surface concentration, k_a and k_d are adsorption and desorption constants, $g(\Gamma)$ and $f(\Gamma)$ are functions that account for the effect of Γ on the adsorption and desorption rates and finally c_i represents the concentration of the species at the

interface. To take into account temperature, activation energy and constants the reaction constant k_a can be expressed using an Arrhenius equation

$$k_a = \frac{\bar{v}}{4} \exp\left(-\frac{E_{barrier}}{k_B T}\right) \tag{6}$$

where $k_B$is Boltzmann constant, T is the temperature , $\bar{v}$ is the mean velocity of the surfactant molecules towards the interface and $E_{barrier}$ is the adsorption potential barrier.[45] Multiplying and dividing the right hand side of equation (6) by s (representing thickness of the subsurface $0 < x < s$) allows representing the adsorption constant in terms of the diffusion coefficient by substituting

$$D = \frac{s\bar{v}}{4} \tag{7}$$

and leading equation (6) to

$$D^* = D \exp\left(-\frac{E_{barrier}}{k_B T}\right) \tag{8}$$

where D^* becomes the actual diffusion coefficient when $E_{barrier} = 0$.[45] Equation (6) can now be written as

$$k_a = \frac{D}{s} \exp\left(-\frac{E_{barrier}}{k_B T}\right) \tag{9}$$

Substituting equation (9) into equation (5) and allowing *s* approach *0*, equation (5) can now be written as

$$\frac{d\Gamma}{dt} = D \exp\left(-\frac{E_{barrier}}{k_B T}\right) g(\Gamma) \frac{(c_s - c_i)}{s} = D^* g(\Gamma) \left.\frac{dc}{dx}\right|_{x=0^+} \tag{10}$$

where $D^* g(\Gamma)$ can be interpreted as the diffusion coefficient of species in the subsurface $(0 < x < s)$ and D the diffusion coefficient of species from the bulk to the subsurface $(s < x < \infty)$. This shows that the diffusion coefficient is constant in the bulk but

dependent on adsorption at the interface (x=0). The dc/dt equation is now modified to make it applicable for not only $d < x < \infty$ but also include the subsurface $0 < x < \infty$.

$$\frac{\partial c}{dt} = D_a \frac{d^2 c}{dx^2} \tag{11}$$

where

$$D_a = \frac{D^{*2}}{D} = D \exp\left(-2\frac{E_{barrier}}{k_B T}\right) \tag{12}$$

is introduced as the apparent diffusion coefficient.[45] Applying boundary and initial conditions

$$c(0,t) = c_i(t) \tag{13}$$

$$c(x,0) = c_0 \tag{14}$$

$$c(\infty,t) = c_0 \tag{15}$$

and applying $c(x,t)$ obtained allows equation (10) to be expressed as

$$\frac{1}{g(\Gamma)}\frac{d\Gamma}{dt} = \sqrt{\frac{D_a}{\pi}}\left[\frac{c_0}{\sqrt{t}} + \frac{1}{2}\int_0^t \frac{c_i(\tau)}{\sqrt{(t-\tau)^3}}d\tau\right] \tag{16}$$

and in the integrated form expressed as[45]

$$\int_0^\Gamma \frac{1}{g(\Gamma)}d\mu = \sqrt{\frac{D_a}{\pi}}\left[2c_0\sqrt{t} - \int_0^t \frac{c_i(\tau)}{\sqrt{(t-\tau)}}d\tau\right] \tag{17}$$

Relationship between concentration of the surface active species and surface tension can be obtained from Gibbs equation that describes thermodynamics of adsorption

$$\Gamma = -\frac{1}{nRT}\frac{d\gamma}{dln(c)} \tag{18}$$

where γ is the dynamic surface/interfacial tension and n is constant, n=1 used for non-ionic surfactants and n=2 for 1:1 ionic surfactants. There are also numerous adsorption

isotherms that can be used to interpret dynamic surface/interfacial tension but only five will be discussed here.

Henry isotherm can be used for low surface concentrations due to the assumption of no interaction between adsorbed monomers and no definition of maximum value of Γ and is expressed as

$$\Gamma = Kc \tag{19}$$

where K is the equilibrium adsorption constant. Applying the Gibbs equation the surface equation of state can be derived[46]

$$\gamma_o - \gamma = nRT\Gamma \tag{20}$$

The Langmuir isotherm is the most commonly used for a nonlinear isotherm and based on lattice type model with assumption that every adsorption site on the lattice is the same, occupancy of sites does not affect probability of adsorption and no interactions and forces between monomers in the lattice is present. The isotherm can be presented as

$$\Gamma = \Gamma_{max}\frac{Kc}{1 + Kc} \tag{21}$$

where Γ_{max} is the maximum number of sites available on the interface.

Freundlich isotherm is an empirical equation which makes enthalpy of adsorption to change exponentially with surface coverage.[46] The relation is given as

$$\Gamma = kc^{\frac{1}{n}} \tag{22}$$

where k and n are constants.

Volmer isotherm is another model that takes into account nonideal nonlocalized adsorption and finite size of molecules with interaction being estimated using statistical mechanics[46] and is presented as

$$c = K\left(\frac{\Gamma}{\Gamma_{max} - \Gamma}\right)\exp\left(\frac{\Gamma}{\Gamma_{max} - \Gamma}\right) \tag{23}$$

Finally, Frumkin isotherm can be applied that takes into account solute-solvent interactions at nonideal surface and most appropriate for nonionic surfactants. It is usually expressed as

$$c = \frac{1}{K}\left(\frac{\Gamma}{\Gamma_{max} - \Gamma}\right)\exp[-A\left(\frac{\Gamma}{\Gamma_{max}}\right) \tag{24}$$

In the case where $A = 0$, the equation will be simplified to Langmuir isotherm.[46]

Assuming that equilibrium between interface and subsurface is established instantaneously and hence the absence of the adsorption potential barrier allows the simplification of the model shown above. This assumption was introduced by Ward and Tordai[47] and allows setting $g(\Gamma) = 1$ and $D_a = D$ which simplifies equation (17) to

$$\Gamma = \sqrt{\frac{D}{\pi}}\left[2c_0\sqrt{t} - \int_0^t \frac{c_i(\tau)}{\sqrt{(t-\tau)}}d\tau\right] \tag{25}$$

Solutions to equation (25) can be obtained only numerically; however, there are asymptotic solutions given by Fainerman et al.[38] for short time $t \to 0$ and long time $t \to \infty$ approximations. As $t \to 0$ Ward and Tordai equation can be simplified to

$$\Gamma = 2c_0\sqrt{\frac{D_0 t}{\pi}} \tag{26}$$

where D_0 signifies diffusion coefficient determined by using the short time solution. To find the right isotherm, the conditions should be taken into account. Assuming that in a short time the amount of surfactant at the interface is negligible and minimum interaction will be present, Henry isotherm can be applied. Combining equation (26) and (20) gives

$$\gamma_o - \gamma_{t\to 0} = 2nRTc_0\sqrt{\frac{D_0 t}{\pi}} \tag{27}$$

As $t \to \infty$, the subsurface concentration will be close to the bulk concentration having negligible change with time and equation (25) can be simplified to

$$\Gamma_{eq} = \sqrt{\frac{D_\infty}{\pi}}\left[2c_0\sqrt{t} - c_i\int_0^t \frac{1}{\sqrt{(t-\tau)}}d\tau\right] = \sqrt{\frac{4D_\infty t}{\pi}}[c_0 - c_i] = \sqrt{\frac{4D_\infty t}{\pi}}\Delta c \tag{28}$$

where D_∞ signifies diffusion coefficient determined by using the long time solution. The Gibbs equation can be used for dilute solutions and written as

$$\frac{\Delta\gamma}{\Delta c} = -\frac{\Gamma_{eq}nRT}{c_0} \tag{29}$$

and substituting equation (28) into (29) gives

$$\frac{\Delta\gamma}{\Gamma_{eq}\sqrt{\frac{\pi}{4D_\infty t}}} = -\frac{\Gamma_{eq}nRT}{c_0} \tag{30}$$

Rearranging equation (30) produces

$$\Delta\gamma = \gamma - \gamma_{t\to\infty} = \frac{nRT\Gamma_{eq}^2}{c_0}\sqrt{\frac{\pi}{4D_\infty t}} \tag{31}$$

Estimating Γ_{eq} by using the surface area of the pendant drop and estimation of area occupied by the exosomes and combining it with surface/interfacial tension data will allow estimation of the diffusion coefficient D by using the equations derived by Fainerman et al.[38]

Figure 5.7 shows an example of clearly a linear correlation between γ and $\sqrt{t}$ for early time and γ and $1/\sqrt{t}$ for late time surface tension data which confirms that exosome adsorption is diffusion-limited and allows application of the two solutions to Ward and

Tordai equation.[44] An assumption was made in this study that exosomes that are acting as surfactants are nonionic and any presence of ionic surfactants can be ignored since a large amount of electrolyte is present in the sample allowing to set $n = 1$ in equations (27) and (31). To find the longer time solution of Ward and Tordai equation (31) the amount of particles at equilibrium at the interface Γ_{eq} needs to be determined. Assuming dense hexagonal packing of exosomes at the interface Γ_{eq} can be estimated by

$$\Gamma_{eq} = \frac{\theta_{max}}{N_A \pi r^2} \tag{32}$$

where θ_{max} is the maximum fraction of the pendant drop surface area that exosome can occupy, N_A is Avogadro's number and r is the mode radius of exosome in the analyzed sample. For hexagonal packing, $\theta_{max} \cong 0.91$.

Table 5.3 shows the diffusion coefficients obtained using the two solutions to Ward and Tordai equation described previously. Estimations of diffusion coefficients vary drastically when reaching the critical micelle concentration (CMC) point. It can also be seen that D_0 is orders of magnitude greater and D_∞ is orders of magnitude smaller than the expected diffusion coefficient estimated by the Stokes-Einstein equation showing failure of two Ward and Tordai relations (27) and (31) to predict diffusion coefficients. Such equations had already been used before for nanoparticles such as cadmium selenide (CdSe) nanoparticles with 2.3 and 6 nm diameter and a decrease of D_∞ from expected diffusion coefficient was noticed when increasing the bulk concentration and was thought to be due to energy barrier to adsorption.[48] A more substantial deviation of Ward and Tordai from Stokes-Einstein prediction was reported when larger surface active nanoparticles were analyzed and reported this to be irreversible adsorption.[30]

Calculated D_∞ appears to decrease with increase in bulk exosome concentration especially when reaching CMC staying orders of magnitude lower than the expected diffusion coefficient and a similar trend was pointed out previously for other nanoparticles.[48] It can be concluded based on this evidence that there is an energy barrier for adsorption. The magnitude of the energy barrier to exosome adsorption can be estimated by equation (8) that was touched on previously and which allows to relate diffusion coefficient D obtained from Stokes-Einstein's equation with the long time diffusion coefficient D_∞

$$D_\infty = D\exp\left(-\frac{\Delta E_{barrier}}{k_B T}\right) \tag{33}$$

where $\Delta E_{barrier}$ represents the potential adsorption barrier.[48] Using data reported in Table 5.3, $\Delta E_{barrier}$ was determined to be $11.7 \pm 4.1 k_B T$ for all measurements which is interestingly close to values reported for ethyl cellulose[30] and tri-*n*-octylphosphine oxide (TOPO)-stabilized cadmium selenide (CdSe) nanoparticles.[48] When reaching CMC bulk concentration, $\sim 10^{-7}$ mol/m^3, $\Delta E_{barrier}$, which determines the kinetic limit of adsorption, becomes larger due to increased occupancy by other exosomes at the interface. This was also mentioned by others with a schematic shown in Figure 5.8.[49]

Bizmark et al. investigated phenomena of irreversible adsorption-driven assembly of nanoparticles at the interface and this became interest in our study.[30] One signature of irreversible adsorption is the equilibrium surface/interfacial tension γ_{eq} that can be obtained from intersection of the long time dynamic surface tension data against $t^{-1/2}$ to be nearly independent of bulk particle concentration. Figure 5.9 clearly shows that in the concentration range studied here, there is no significant difference in γ_{eq} which also means that after a long period of time, the surface coverage approaches the maximum of

0.91. It also shows that at exosome concentration lower than $\sim 3.4\text{x}10^{-10}$ mol/m^3 exosomes become depleted from the bulk. This brings to the hypothesis that exosome adsorption is favored and is irreversible similar to nanoparticles reported previously. A different indicator of a reversible adsorption is the energy of adsorption to be on the order of thermal fluctuation that is close to k_BT. To estimate adsorption energy, two approaches were used. The first approach is the use of equation recently introduced by Du et al.[50]

$$\Delta E_{ads} = \frac{\gamma_{eq} - \gamma_0}{\theta_{max}} \pi r^2 \tag{34}$$

where ΔE_{ads} is the adsorption energy of nanoparticles, θ_{max} is the maximum interface coverage being set to 0.91, $\gamma_0$is the initial surface tension and r is the radius of nanoparticles. Since exosomes do not have the same size and instead have a size distribution, the mode size was used for the calculation. Another approach is a novel equation introduced by Bizmark et al. [30]

$$\gamma = \gamma_0 - 2N_A|\Delta E_{ads}|c_0\sqrt{\frac{Dt}{\pi}} \tag{35}$$

which in differential form can be represented as

$$\left.\frac{d\gamma}{d\sqrt{t}}\right|_{t\to 0} = -2N_A|\Delta E_{ads}|c_0\sqrt{\frac{D}{\pi}} \tag{36}$$

where D is the Stokes-Einstein diffusion coefficient determined using the mode size of exosomes and change of early time dynamic surface tension γ with respect to $\sqrt{t}$. The average values obtained are presented in Table 5.4 with equation (34) and (36) giving $9.82E4\ k_BT \pm 2.89E4\ k_BT$ and $9.65E4\ k_BT \pm 6.81E4\ k_BT$, respectively. The large deviation when using equation (36) is most likely due to the short time change in surface

tension being affected by background surface active molecules contributing to higher standard deviation than (34). It can be seen that values of ΔE_{ads} obtained from both methods are orders of magnitude greater than thermal fluctuation and not dependent on bulk concentration of exosomes. This high magnitude of adsorption energy leads to conclude that adsorption of exosomes to the interface is thermodynamically favored and equations (27) and (31) are no longer appropriate for analysis.

When adsorption energy is known, it is possible to estimate transient surface coverage of nanoparticles at the surface directly from dynamic surface tension data. Knowing adsorption energy, equation (34) can now be represented as time dependent

$$\Delta E_{ads} = \frac{\gamma(t) - \gamma_0}{\theta(t)} \pi r^2 \tag{37}$$

where $\theta(t)$ is change in surface coverage with time and $\gamma(t)$ is dynamic surface tension. Using equation (37) and ΔE_{ads} presented in Table 5.4 the surface coverage of pendant drop with respect to time was determined and examples for serum sample #1 and 22Rv1 are presented in Figure 5.10. Knowledge of the change in surface coverage due to irreversible adsorption of nanoparticles now allows estimation of adsorption constant k_a by applying an equation introduced previously for late stages of adsorption[30,51]

$$\theta(t) = \theta_{max} - \frac{K_l}{\pi r^2 c_0} \sqrt{\frac{1}{Dt}} \tag{38}$$

where K_l is the long-time expansion coefficient [30] and can be obtained from the slope obtained from $\theta(t)$ vs $1/\sqrt{t}$ plot, while θ_{max} from the intercection with y-axis which is equal 0.91 when a sufficient bulk concentration of particles is present. K_l is known to be related to the dimensionless adsorption constant $\overline{k_a}$ for spherical particles by[30,51]

$$\overline{k_a} = \frac{\theta_{max}^3}{2K_l^2} \tag{39}$$

and the actual adsorption constant obtained by [30]

$$k_a = \overline{k_a}\,\pi r^2 c_0 D \tag{40}$$

Table 5.5 shows that k_a ranges from $10^{-5} - 10^{-4}$ m/s. The outliers showing smaller values are mostly due to the sample already containing a large particle concentration on the interface which lowers the adsorption constant by orders of magnitude.

During the early time when the surface concentration of particles is low, the adsorption flux of exosomes to the surface can be estimated by

$$j|_{x\to 0^+} = -\,c_0\sqrt{\frac{D}{\pi t}} \tag{41}$$

and results are provided in Figure 5.6d and e. The change of adsorption flux with time from the liquid/air experiment is ~5-7 times larger while liquid/liquid agrees better with the flux predicted by the model. This difference can be due to the effect of sample evaporation during liquid/air analysis and accuracy of NTA.

5.5 Conclusion

Exosomes are biological nanoparticles that have received a lot of attention due to their potential of being an early stage diagnostic tool for different types of cancer as well as highly localized and specific drug delivery. Due to their size and concentration, the number of characterization methods is sparse. We have found that exosomes are surface active and the interface acts as a sink which would play a critical role in biological function. This finding opened a new method for characterization of exosome samples to easily determine their concentration in a sample and potentially size. It was also shown

that exosomes irreversibly adsorb to the interface due to significantly higher energy released after adsorption compared to the mean energy of thermal fluctuation and failure of Ward and Tordai approximation. Such a property of adsorption may be also involved in exosome binding to the cell membrane.

Table 5.1: Medium used for cell line growth.

Cell line	LNCap	22Rv1	PC3	PCS	MCF7	MCF10a	MDA-MB-231
Medium	RPMI-1650 Medium	RPMI-1650 Medium	F-12K Medium	SteCM Medium	Eagle's Minimum Essential Medium	Mammary Epithelial Cell Growth (MEGM)	Leibovitz's L15 Medium (grown without CO2)

Table 5.2: Exosome samples analyzed using NTA and surface tension methods. (a) and (b) show the results obtained for serum and cell line samples, respectively, by using NTA.

(A)	Serum							
Sample	#1	#1 filtered	#2	#3	#4	#5	#6	#7
Mode (nm)	112	100	108	93	77	86	106	141
Mean (nm)	148	165	133	122	91	113	134	172
SD (nm)	78	97	59	57	40	58	67	72
NTA Original Conc (#/mL)	4.3E12 ±3.0E11	3.9E11 ±3.4E10	9.1E11 ±2.7E11	9.5E11 ±1.3E11	4.3E11 ±3.5E10	6.2E11 ±3.6E10	2.2E10 ±1.3E9	2.7E12 ±3.6E11
ST Original Conc (#/mL)	5.7E12	3.9E11	1.0E12	6.4E11	6.7E11	4.0E11	2.3E10	2.25E12

(B)	Cell lines							
Sample	22Rv1	22Rv1 Filtered	LNCap	PC3	PCS	MCF7	MCF10a	MDA-MB 231
Mode (nm)	144	147	123	145	112	125	123	139
Mean (nm)	181	184	150	230	163	175	189	190
SD (nm)	71	87	58	131	76	92	89	88
NTA Original Conc (#/mL)	2.6E12 ±2.8E11	5.4E10 ±2.3E10	1.3E12 ±1.2E11	1.2E12 ±1.1E11	2.2E12 ±1.7E11	2.8E12 ±2.5E11	2.0E11 ±1.5E10	4.6E12 ±4.4E11
ST Original Conc (#/mL)	3.2E12	7.6E10*	1.4E12	9.6E11	3.7E12	4.0E12	1.1E11	3.7E12

* The correlation between surface tension and exosome concentration found for serum was used for this sample

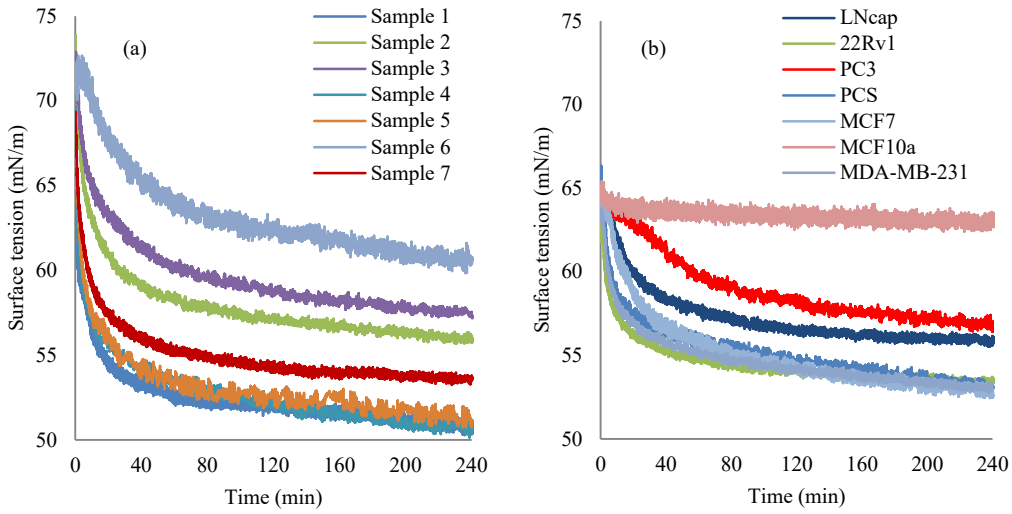

Figure 5.1: Surface tension measurements of samples diluted 1:1000 or 1:100 of serum (a) and cell line samples (b). An average of 4 runs (4 hours/run) is shown for each sample.

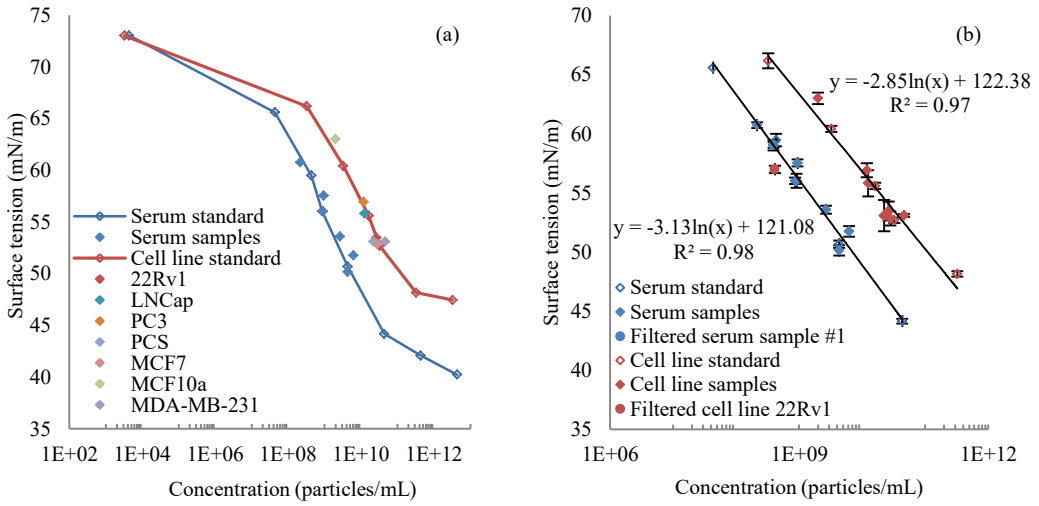

Figure 5.2: Correlation of surface tension and exosome concentration in a sample (a) Surface tension after 4 hours of pendant drop formation and natural logarithm of the exosome concentration (b) Linear dependence of surface tension after 4 hours of pendant drop formation with the natural logarithm of exosome concentration.

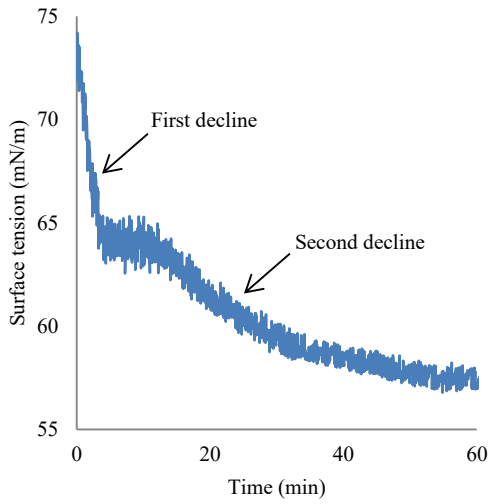

Figure 5.3: Surface active analyte present in a cell line sample with first decrease in surface tension due to presence of other surface active analyte besides exosomes.

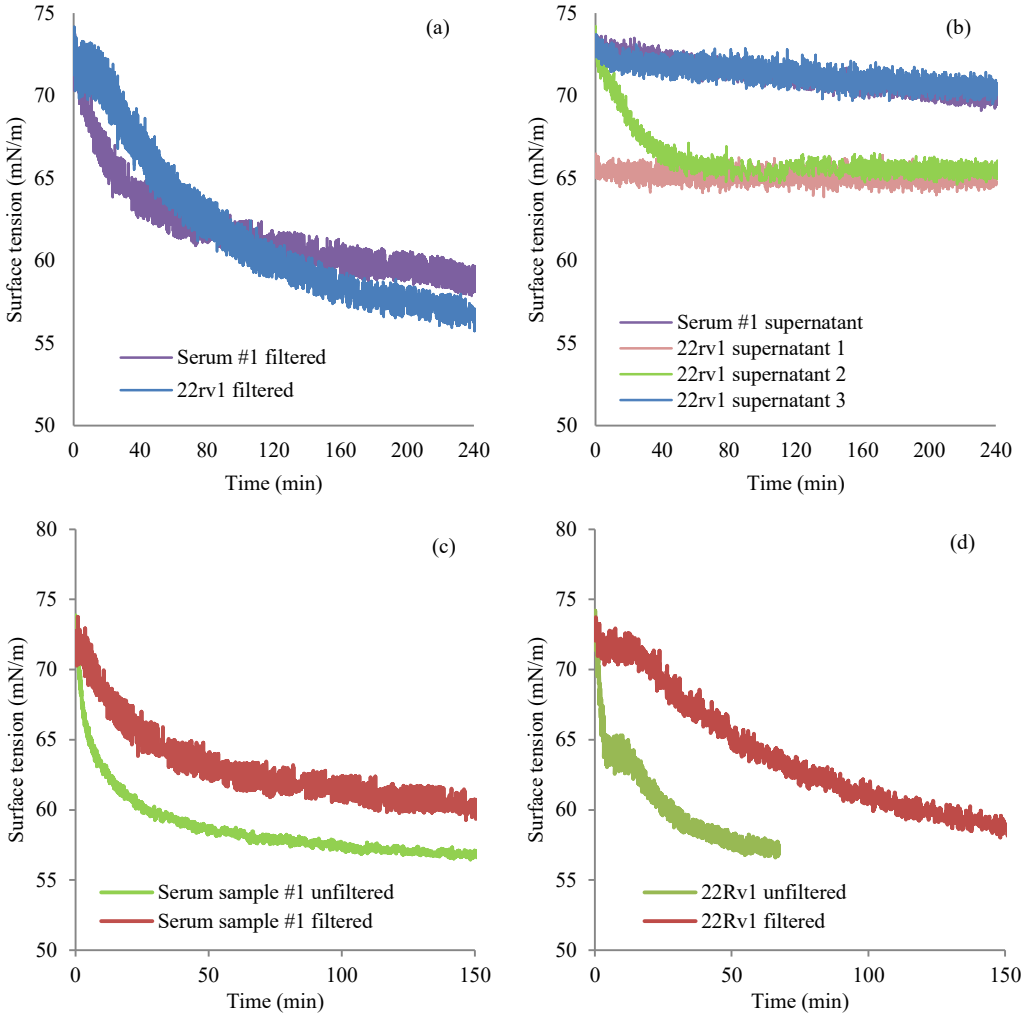

Figure 5.4: Impact of 100 kDa filtration of the sample on surface tension (a) Final 22rv1 and serum #1 samples after filtrations (b) Supernatants after each filtration step (1 for serum and 3 for 22rv1) (c) Comparison of surface tension profile before and after filtration of serum sample #1 (d) Comparison of surface tension profile before and after filtration of exosomes from 22Rv1 cell line.

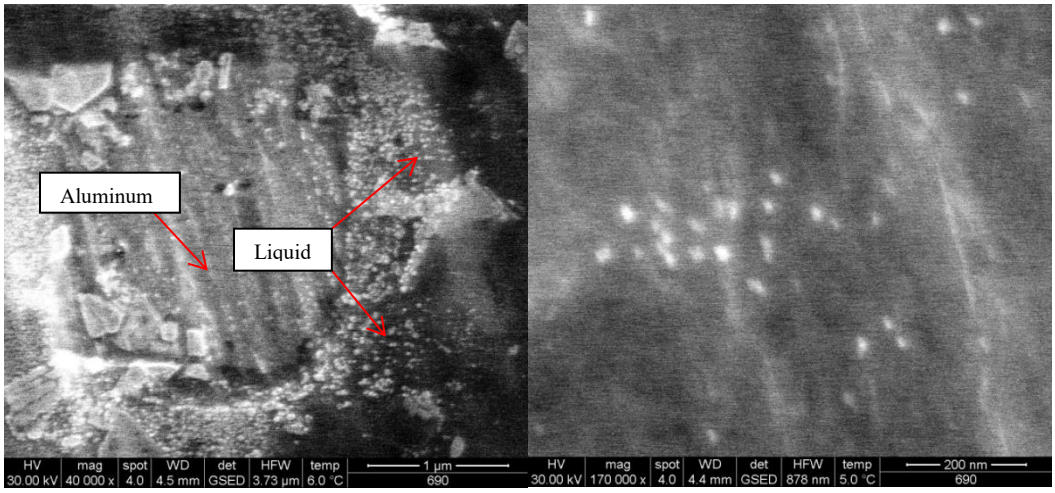

Figure 5.5: ESEM (vapor/liquid equilibrium) images showing exosomes present near the liquid surface.

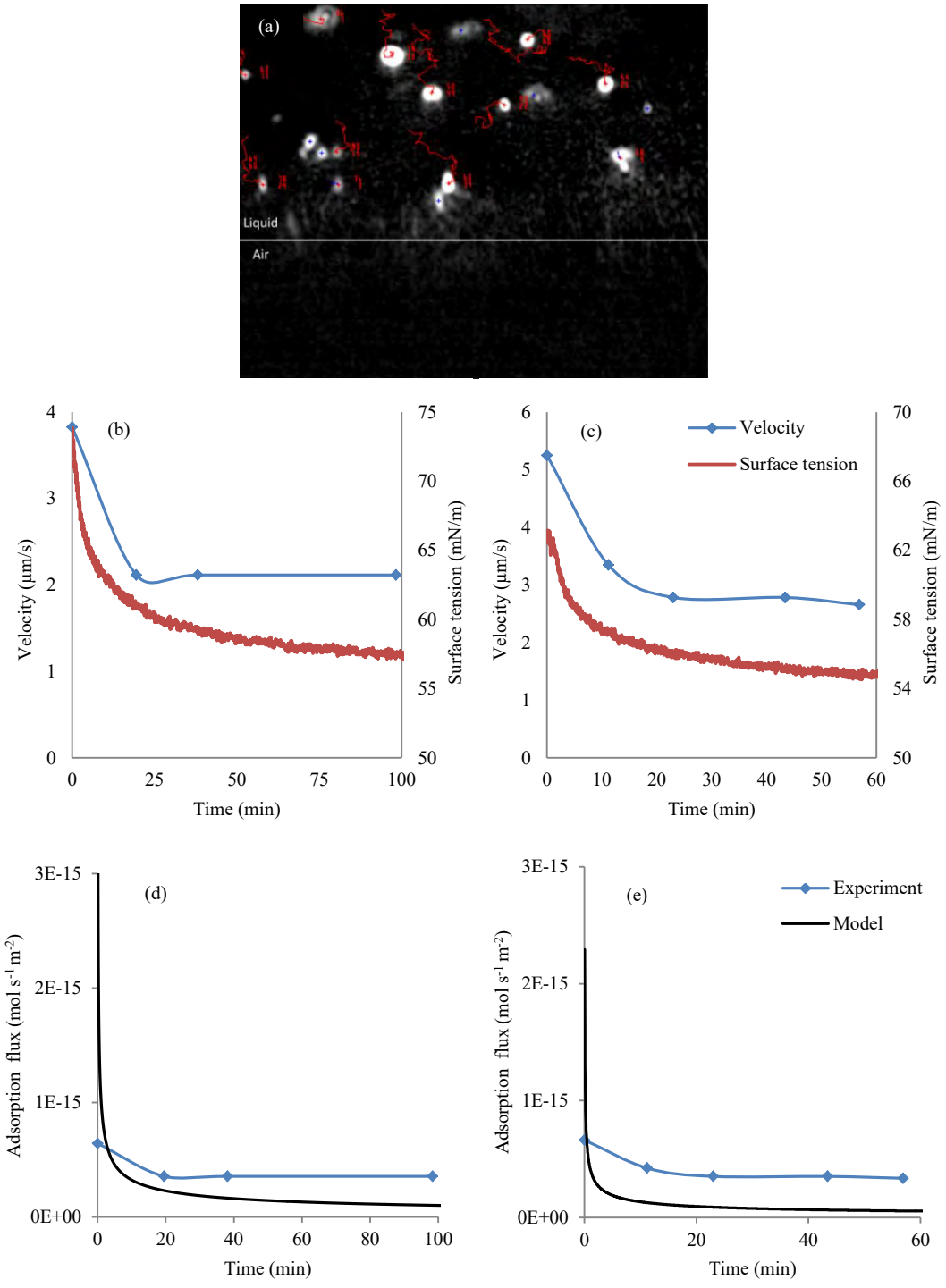

Figure 5.6: Migration of exosomes to the liquid/air interface. White marks show exosomes and red lines show tracking path of exosomes in the given frame (a). Magnitude of exosome velocity towards the liquid/air interface for serum sample #1 (b) and cell line 22Rv1 (c) and exosome adsorption flux to the surface calculated from equation (39) and using NTA of exosomes from serum sample #1 (d) and 22rv1 cell line (e).

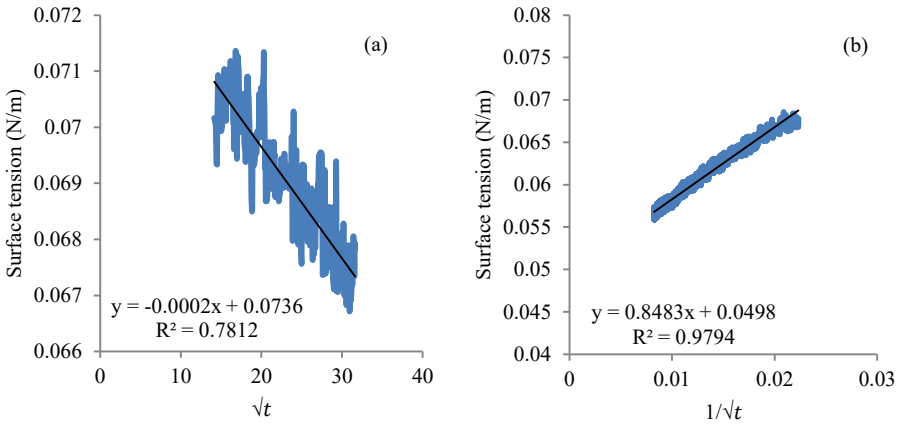

Figure 5.7: Examples of results based on raw surface tension data that are used for calculating D_0 and D_∞. (a) $\frac{d\gamma}{d\sqrt{t}}$ and (b) $\frac{d\gamma}{d\left(\frac{1}{\sqrt{t}}\right)}$.

Table 5.3: Calculated D_0 and D_∞ based on Fainerman et al. model.[38]

Exosome source	Concentration (mol/m^3)	D_0 (x 10^{-3}) (m^2/s)	D_∞ (x 10^{-16}) (m^2/s)	$\Delta E_{barrier}/k_BT$
		$D_{SE} = 3.83$ x 10^{-12} m^2/s		
Serum#1 (liquid/air)	1.44E-9	45.8	30.5	7.14
	7.19E-9	0.581	9.77	8.27
	7.19E-8	7.90	0.134	12.6
	7.19E-7	0.897	0.0247	14.3
	7.19E-6	0.0326	0.000647	17.9
		$D_{SE} = 3.97$ x 10^{-12} m^2/s		
Serum #1 (liquid/air) filtered	6.54E-10	35.4	226	5.17
		$D_{SE} = 2.98$ x 10^{-12} m^2/s		
22Rv1 (liquid/air)	3.37E-9	23.9	0.650	10.7
	6.74E-9	11.3	1.51	9.89
	3.37E-8	27.2	0.344	11.4
	3.37E-7	8.56	0.0102	14.9
	3.37E-6	0.173	0.00144	16.8
		$D_{SE} = 2.92$ x 10^{-12} m^2/s		
22Rv1 (liquid/air) filtered	6.87E-10	32.1	40.7	6.58
		$D_{SE} = 3.08$ x 10^{-12} m^2/s		
MDA-MB-23 (liquid/liquid)	1.31E-7	3.13	0.00105	17.2
		$D_{SE} = 3.48$ x 10^{-12} m^2/s		
LNCap (liquid/liquid)	4.23E-8	6.47	0.682	10.8

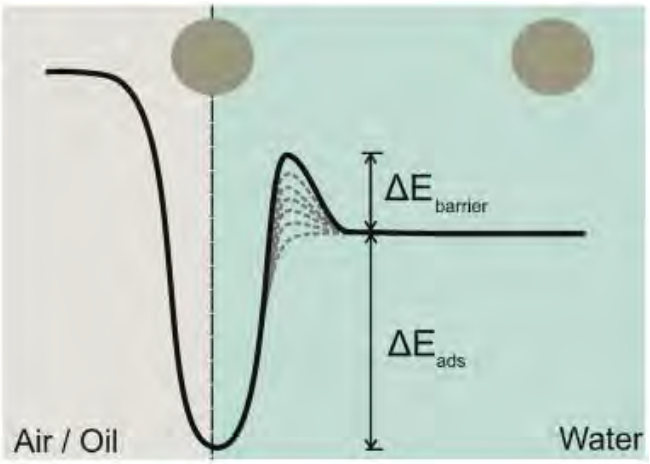

Figure 5.8: Schematic adapted from[49] showing increase in the energy barrier as surface becomes occupied with particles.

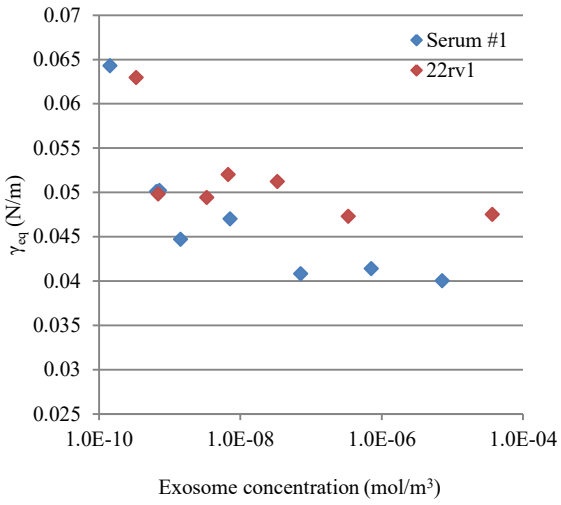

Figure 5.9: Equilibrium surface tension obtained from intercept of long time surface tension change with $t^{-1/2}$ (e.g., Figure 7b).

Table 5.4: Adsorption energy of exosomes obtained by applying equation (34) and (36) for comparison.

Exosome source	Concentration (mol/m^3)	$\Delta E_{ads}/k_BT$ Equation (34)	$\Delta E_{ads}/k_BT$ Equation (36)
Serum #1 (liquid/air)	1.44E-9	5.61E4	19.4E4
	7.19E-9	6.68E4	2.18E4
	7.19E-8	8.34E4	8.05E4
	7.19E-7	8.98E4	2.71E4
	7.19E-6	9.70E4	0.52E4
Serum #1 (liquid/air) filtered	6.54E-10	17.8E4	17.0E4
22Rv1 (liquid/air)	3.37E-9	7.43E4	15.9E4
	6.74E-9	10.2E4	10.9E4
	3.37E-8	9.19E4	16.9E4
	3.37E-7	10.9E4	9.50E4
	3.37E-6	10.9E4	1.35E4
22Rv1 (liquid/air) filtered	6.87E-10	9.81E4	18.3E4
MDA-MB-231 (liquid/liquid)	1.31E-7	11.5E4	5.06E4
LNCap cell line (liquid/liquid)	4.23E-8	6.29E4	7.28E4

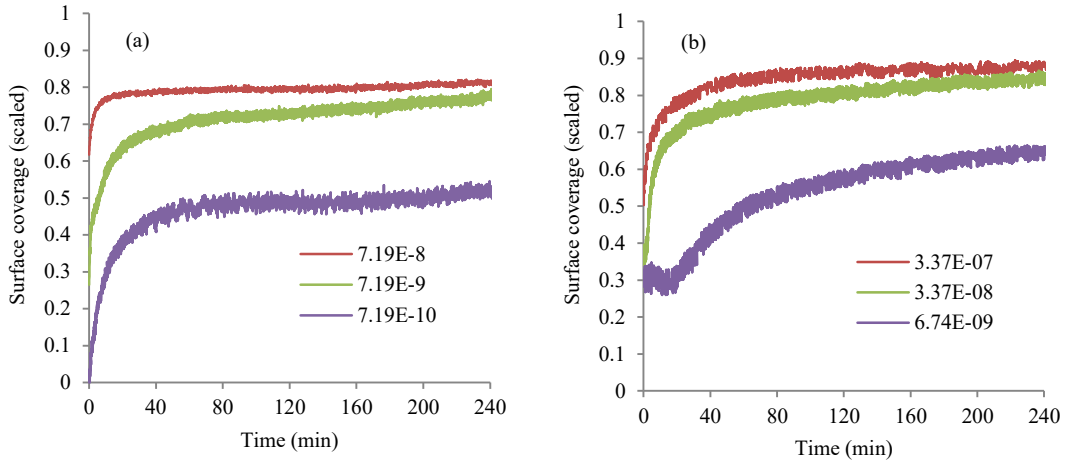

Figure 5.10: Surface coverage obtained from equation (36) for serum sample #1 (a) and 22Rv1 cell line (b). The concentration is given in $\mathrm{mol}/\mathrm{m}^3$.

Table 5.5: Long-time expansion coefficient K_l and exosome adsorption constant k_a.

Exosome source	Concentration (mol/m^3)	K_l	$k_a\left(\frac{m}{s}\right)$
Serum #1 (liquid/air)	1.44E-9	8.80E-5	5.87E-4
	7.19E-9	4.73E-4	1.86E-4
	7.19E-8	8.16E-4	6.46E-4
	7.19E-7	3.79E-3	2.58E-4
	7.19E-6	2.18E-1	1.16E-6
Serum #1 (liquid/air) filtered	6.54E-10	5.84E-5	5.07E-5
22Rv1 (liquid/air)	3.37E-9	4.38E-3	1.92E-6
	6.74E-9	2.35E-3	1.07E-5
	3.37E-8	3.83E-3	2.44E-5
	3.37E-7	2.43E-2	6.33E-6
	3.37E-6	1.74E+2	1.22E-12
22Rv1 (liquid/air) filtered	6.87E-10	4.05E-4	4.60E-5
MDA-MB-231 (liquid/liquid)	1.31E-7	6.49E-2	3.08E-7
LNCap (liquid/liquid)	4.23E-8	5.27E-3	1.42E-5

5.6 References

1. Simons, M. & Raposo, G. Exosomes-vesicular carriers for intercellular communication. *Curr. Opin. Cell Biol.* **21,** 575–81 (2009).

2. Palma, J. *et al.* MicroRNAs are exported from malignant cells in customized particles. *Nucleic Acids Res.* **40,** 9125–38 (2012).

3. Thery, C., Zitvogel, L. & Amigorena, S. Exosomes: composition, biogenesis and function. *Nat. Rev. Immunol.* **2,** 569–579 (2002).

4. Trams, E. G., Lauter, C. J., Salem, Jr., N. & Heine, U. Exfoliation of membrane ecto-enzymes in the form of micro-vesicles. *Biochim. Biophys. Acta.* **645,** 63–70 (1981).

5. Ge, R., Tan, E., Sharghi-Namini, S. & Asada, H. H. Exosomes in cancer microenvironment and beyond: have we overlooked these extracellular messengers? *Cancer Microenviron.* **5,** 323–332 (2012).

6. Pucci, F. & Pittet, M. J. Molecular Pathways: Tumor-derived microvesicles and their interactions with immune cells in vivo. *Clin. Cancer Res.* **19,** 2598–604 (2013).

7. Vlassov, A. V., Magdaleno, S., Setterquist, R. & Conrad, R. Exosomes: current knowledge of their composition, biological functions, and diagnostic and therapeutic potentials. *Biochim. Biophys. Acta.* **1820,** 940–8 (2012).

8. Chen, X. *et al.* Characterization of microRNAs in serum: a novel class of biomarkers for diagnosis of cancer and other diseases. *Cell Res.* **18,** 997–1006 (2008).

9. Lee, Y. S. & Dutta, A. MicroRNAs in cancer. *Annu. Rev. Pathol.* **4,** 199–227 (2009).

10. Taylor, D. D. & Gercel-Taylor, C. MicroRNA signatures of tumor-derived exosomes as diagnostic biomarkers of ovarian cancer. *Gynecol. Oncol.* **110,** 13–21 (2008).

11. King, H. W., Michael, M. Z. & Gleadle, J. M. Hypoxic enhancement of exosome release by breast cancer cells. *BMC Cancer* **12,** 421 (2012).

12. Jørgensen, M. *et al.* Extracellular vesicle (EV) array: microarray capturing of exosomes and other extracellular vesicles for multiplexed phenotyping. *J. Extracell. Vesicles* **2,** doi: 10.3402/jev.v2i0.20920

13. Momen-Heravi, F. *et al.* Impact of biofluid viscosity on size and sedimentation efficiency of the isolated microvesicles. *Front. Physiol.* **3,** 162 (2012).

14. Anderson, W., Kozak, D., Coleman, V. A., Jämting, Å. K. & Trau, M. A comparative study of submicron particle sizing platforms: accuracy, precision and resolution analysis of polydisperse particle size distributions. *J. Colloid Interface Sci.* **405,** 322–30 (2013).

15. Duijvesz, D., Luider, T., Bangma, C. H. & Jenster, G. Exosomes as biomarker treasure chests for prostate cancer. *Eur. Urol.* **59,** 823–31 (2011).

16. Dupr , A. *T orie M canique de la Chaleur* (Gauthier-Villars, Paris, 1869).

17. Rayleigh, Lord. On the tension of recently formed liquid surfaces. *Proc. R. Soc. Lond.* 281–287 (1889).

18. Gibbs, J. W. *The Collected Works vol 1* (Green and Co., New York, 1928).

19. Bigelow, L. & Washburn, R. Variations in the surface tensions of solutions. *Am. Chem. Soc.* **32**, 321–353 (1928).

20. Milner, S. R. On surface concentration, and the formation of liquid films. *Philos. Mag. Ser.* **13,** 96–110 (1907).

21. Florence, R. T., Myers, R. J. & Harkins, W. D. Contact potentials of reversible soluble films of lauric acid. *Nature* **138**, 405–406 (1936).

22. Bond, W. N. & Puls, H. O. The change of surface tension with time. *London, Edinburgh, Dublin Philos. Mag. J. Sci.* **24,** 864–888 (1937).

23. Ross, S. The change of surface tension with time. I. Theories of diffusion to the surface. *J. Am. Chem. Soc.* **67,** 990–994 (1945).

24. Langmuir, I. & Schaefer, V. J. Optical measurement of the thickness of a film adsorbed from a solution. *J. Am. Chem. Soc.* **59,** 1406 (1937).

25. Addison, C. C. 66. The properties of freshly formed surfaces. Part II. The rate of adsorption of isoamyl alcohol at the air–water surface. *J. Chem. Soc.* 252–256 (1944).

26. Ward, A. F. H. & Tordai, L. Time-dependence of boundary tensions of solutions I. the role of diffusion in time-effects. *J. Chem. Phys.* **14,** 453 (1946).

27. Chernyshev, V. S. & Skliar, M. Surface tension of water in the presence of perfluorocarbon vapors. *Soft Matter* **10,** 1937–43 (2013).

28. Gupta, R. & Rousseau, D. Surface-active solid lipid nanoparticles as Pickering stabilizers for oil-in-water emulsions. *Food Funct.* **3,** 302–11 (2012).

29. Liu, L., Zhang, J., Wu, C. & Zhao, H. Surface-active gold nanoparticles with mixed polymer brushes as surfactants in the preparation of polystyrene colloid particles. *Macromol. Rapid Commun.* **29,** 45–51 (2008).

30. Bizmark, N., Ioannidis, M. A. & Henneke, D. E. Irreversible adsorption-driven assembly of nanoparticles at fluid interfaces revealed by a dynamic surface tension probe. *Langmuir* **30,** 710–7 (2014).

31. Rana, S. *et al.* Control of surface tension at liquid-liquid interfaces using nanoparticles and nanoparticle-protein complexes. *Langmuir* **28,** 2023–7 (2012).

32. Conde-Vancells, J. *et al.* Characterization and comprehensive proteome profiling of exosomes secreted by hepatocytes. *J. Proteome Res.* **7,** 5157–5166 (2008).

33. Hu, G., Drescher, K. M. & Chen, X.-M. Exosomal miRNAs: biological properties and therapeutic potential. *Front. Genet.* **3,** 1–9 (2012).

34. Taylor, D. D. & Gercel-Taylor, C. in *Emerg. Concepts Tumor Exosome–Mediated Cell-Cell Commun.* 133 (2012).

35. Kharaziha, P., Ceder, S., Sanchez, C. & Panaretakis, T. Multitargeted therapies for multiple myeloma. *Autophagy* **9,** 255–257 (2013).

36. Tripp, B. C., Magda, J. J. & Andrade, J. D. Adsorption of globular proteins at the air/water interface as measured via dynamic surface tension: concentration dependence, mass-transfer considerations, and adsorption kinetics. *J. Colloid Interface Sci.* **173,** 16–27 (1995).

37. Harkins, D. A method for the determination of surface and interfacial tension from the maximum pull on a ring. *J. Am. Chem. Soc.* **399,** 1751–1772 (1930).

38. Fainerman, V. B., Miller, R. & Joos, P. The measurement of dynamic surface tension by the maximum bubble pressure method. *Colloid Polym. Sci.* **272,** 731–739 (1994).

39. Spelt, J. K., Rotenberg, Y., Absolom, D. R. & Neumann, A. W. Sessile-drop contact angle measurements using axisymmetric drop shape analysis. *Colloids and Surfaces* **24,** 127–137 (1987).

40. Río, O. & Neumann, A. Axisymmetric drop shape analysis: computational methods for the measurement of interfacial properties from the shape and dimensions of pendant and sessile drops. *J. Colloid Interface Sci.* **196,** 136–147 (1997).

41. Sharma, S., Gillespie, B. M., Palanisamy, V. & Gimzewski, J. K. Quantitative nanostructural and single-molecule force spectroscopy biomolecular analysis of human-saliva-derived exosomes. *Langmuir* **27,** 14394–400 (2011).

42. Baran, J. *et al.* Circulating tumour-derived microvesicles in plasma of gastric cancer patients. *Cancer Immunol. Immunother.* **59,** 841–50 (2010).

43. Böker, A., He, J., Emrick, T. & Russell, T. P. Self-assembly of nanoparticles at interfaces. *Soft Matter* **3,** 1231 (2007).

44. Diamant, H. & Anderlman, D. Adsorption kinetics of surfactants at fluid-fluid interfaces. *Progr. Colloid Polym. Sci.* **103**, 51–59 (1997).

45. Liggieri, L., Ravera, F. & Passerone, A. A diffusion-based approach to mixed adsorption kinetics. *Colloids Surfaces A Physicochem. Eng. Asp.* **114,** 351–359 (1996).

46. Eastoe, J. & Dalton, J. . Dynamic surface tension and adsorption mechanisms of surfactants at the air–water interface. *Adv. Colloid Interface Sci.* **85,** 103–144 (2000).

47. Ward, A. F. H. & Tordai, L. Time dependence of boundary of solutions. I. The role of diffusion in time effect. *J. Chem. Phys* **14,** 453–461 (1946).

48. Kutuzov, S. *et al.* On the kinetics of nanoparticle self-assembly at liquid/liquid interfaces. *Phys. Chem. Chem. Phys.* **9,** 6351–6358 (2007).

49. Deshmukh, O., van den Ende, D., Stuart, M. C., Mugele, F. & Duits, M. H. G. Hard and soft colloids at fluid interfaces: adsorption, interactions, assembly & rheology. *Adv. Colloid Interface Sci.* **In Press** (2015).

50. Du, K., Liddle, J. A. & Berglund, A. J. Three-dimensional real-time tracking of nanoparticles at an oil-water interface. *Langmuir* **28,** 9181–9188 (2012).

51. Adamczyk, Z. Kinetics of diffusion-controlled adsorption of colloid particles and proteins. *J. Colloid Interface Sci.* **229,** 477–489 (2000).

CHAPTER 6

SIZE AND SHAPE CHARACTERIZATION OF HYDRATED AND DESICCATED EXOSOMES*

6.1 Abstract

Exosomes are nanovesicles secreted by cells into circulation. Their reported sizes vary substantially, which likely reflects the difference in utilized isolation techniques, cells that secreted them and the methods used in their characterization. We analyzed the influence of the last factor on the measured sizes and shapes of hydrated and desiccated exosomes isolated from the serum of a pancreatic cancer patient and a healthy control. We found that hydrated exosomes are close to spherical nanoparticles with a hydrodynamic radius that is substantially larger than the geometric size. For desiccated exosomes, it was found that the desiccated shape and sizing are influenced by the manner in which drying occurred. Isotropic desiccation in aerosol preserves the near spherical shape of the exosomes, while drying on a surface likely distorts their shapes and influences sizing results by techniques that require surface fixation prior to analysis.

---

*Springer and Analytical and Bioanalytical Chemistry, 407, 2015, 3285-3301, Size and Shape Characterization of Hydrated and Desiccated Exosomes, Chernyshev V.S., Rachamadugu R., Tseng Y.H., Belnap D.M., Jia Y., Branch K.J., Butterfield A.E., Pease L.F. 3rd, Bernard P.S., Skliar M., 1-7, original copyright notice with kind permission from Analytical and Bioanalytical Chemistry

6.2 Introduction

Cells actively secrete exosomes via an endocytic pathway.[1–3] Exosomes are found in the extracellular space and all body fluids, including blood, urine, and saliva. The molecular content of exosomes is derived from the cells that release them. The frequency of release depends on the cell environment, such as the level of dissolved oxygen and pH,[4,5] and a cell type, with cancer cells known to release a larger number of exosomes. They carry small noncoding RNAs, though the number of microRNA (miRNA) molecules enveloped inside each exosome may not be high.[6] Nevertheless, some reports suggest that the majority of miRNAs in the blood are contained within exosomes.[7] By fusing with recipient cells and releasing their RNA and other cargo,[8–11] exosomes are thought to play a role in short and long-range intercellular signaling.

Exosomes can be differentiated from other circulating vesicles by the markers of the endosomal pathway and their small size that distinguishes them from other microvesicles. Though an important differentiator, the size of exosomes is often reported with substantial variability, as illustrated by a sample of published results summarized in Table 6.1.

Several factors likely contribute to a large range in reported sizes, including the source of exosomes by the type of body fluid or cell line from which they were isolated. The exosome isolation method, which may include ultracentrifugation (UC),[12] solvent precipitation,[13] size exclusion chromatography (SEC),[14] immunoaffinity isolation,[15] microfluidic techniques,[16] and ultrafiltration[17] is another factor in size variability.[15,18,19] The choice of characterization techniques influences the measured size of exosomes, as well. While it is recognized that the precise determination of the size distribution of

exosomes with any given technique is difficult,[20–22] it is often underappreciated that different analytical methods estimate sizes based on dissimilar physical principles, which produce identical results only in limited cases.

Sample preparation steps used with different methods, such as sample verification, desiccation, or surface fixation, also affect sizing results. The geometric shape of exosomes influences size measurements obtained with techniques that determine particle sizes from their mobility, such as nanoparticle tracking analysis (NTA), dynamic light scattering (DLS), and differential mobility analysis (DMA). The standard practice in NTA and DLS is to assume that the shape of exosomes is spherical, contrary to numerous reports and reviews[23] suggesting that the exosomes have a cup-shaped geometry. Therefore, to provide sizing consistency and accuracy by methods that rely on particle mobility, the shape of hydrated and desiccated exosomes becomes an important factor that must be examined.

In this paper, we quantify the influence of different analytical techniques on the measurements of exosome sizes. By reanalyzing the same samples by different sizing techniques we find significant variability in the results that is comparable with the variability seen in Table 6.1, where the difference between samples – by biofluids, cell lines, and techniques employed in their isolation – is also a contributing factor. We offer a model that explains this result and suggests that the difference in exosome sizes measured by different techniques may itself be an important characteristic of a sample that depends on such biophysical properties of the exosomes as their surface decoration, elasticity, and molecular content.

6.3 Materials and Methods

6.3.1 Samples and exosome isolation

Sera samples from a 75-year-old female pancreatic cancer patient with high levels of the tumor marker CA19-9 (414 U/mL) and a healthy 42-year-old female seen for routine cholesterol testing were used in this study. Both samples were obtained from ARUP Laboratories Inc. (Salt Lake City, UT) and deidentified according to IRB protocol. Exosomes were isolated from 1mL serum using an ExoQuick kit (System Biosciences, Mountain View, CA) following manufacturer's instructions. Briefly, serum was centrifuged at 3,000×g for 15 minutes to remove cells and cell debris. The supernatant was transferred to a sterile vessel and 252 μL of ExoQuick was added. The mixture was refrigerated for 30 minutes and then centrifuged at 1500×g for 30 minutes at room temperature. After centrifugation, the supernatant was discarded and the exosome pellet saved. To spin down the residual ExoQuick solution, the pellet was centrifuged for another 5 minutes at 1500×g and the supernatant was removed without disturbing the pellet. The pellet was then re-suspended in 200 μl of 2 mM ammonium acetate (AA) buffer. The buffer solution was prepared using AA salt (Sigma-Aldrich, St. Louis, MO) and DI water (Milli-Q filtration). The exosome size was then characterized by all analytical techniques.

6.3.2 Analytical Methods

6.3.2.1 Scanning Electron Microscopy (SEM)

Prior to SEM imaging, both samples were diluted 1:100 in DI water. A glass slide was gently cleaned with nitrogen gas and placed on the specimen stage of the SEM (FEI NanoNova 630 High Resolution SEM). Five microliters of each sample were then placed

on the glass slide and allowed to dry. The samples were imaged at 0.98 Torr using a low vacuum secondary electron detector at magnifications in the 35,000-65,000× range. The acquired 1024×943 pixel images were analyzed using custom MATLAB software to determine the exosome size distribution. The grayscale SEM images were first converted into a binary form to define the boundary of each particle. Each exosome in each image was approximated by an ellipse that provided the best (in the least squares sense) fit to its perimeter. The exosome diameter was calculated by geometrically averaging the lengths of major and minor axis (equal for spherical particles) of the fitted ellipse.

6.3.2.2 Electrospray Differential Mobility Analysis (ES-DMA)

DMA has been previously used to size biological particles, including cold viruses,[24] lipoproteins,[25] virus-like particles,[26] and other macromolecular assemblies.[27,28] This study is the first to use this technique to characterize exosome sizes. Patient and control samples were diluted 1:100 in AA solution and 0.5 mL of the preparation was used in the electrospray (ES) aerosol generator (TSI Model 3480; Shoreview, MN) to confine individual exosomes inside charged droplets formed by atomizing the suspension in the Taylor cone formed at the end of 25 μm ID capillary. Pressure-driven flow through the capillary was maintained by 26 kPa excess pressure across the capillary. A stream of gas consisting of 1.0 L/min of air and 0.2 L/min of carbon dioxide was used to entrain the charged droplets and carry them into a bipolar charge neutralizer where they were bombarded by α-particles formed by radioactive decay of ^{210}Po. The solvent and volatile ammonium acetate salt rapidly evaporated from the entrained droplets, while the bombardment by α-particles electrically neutralized most exosomes desiccated in the gas phase.[29] A fraction of the desiccated exosomes retained a single net positive or negative

change (±1 electron charge), while particles with higher charges (±2, ±3,…) occur at an increasingly rare frequency.[30] For example, after the neutralization, 46.7% of 74 nm particles carry an elementary charge of ±1 (26.2% of particle will have an excess and 20.5% a deficit of a single charge); 1.9% and 3.2% will have a charge of ±2, respectively, and a negligible number of higher charged particles; the balance is formed by neutral particles.[29]

After charge reduction in the neutralizer, the desiccated exosomes were carried by flowing gas into the differential mobility analyzer (TSI Model 3080) operated with sheath flow of 10 L/min of nitrogen. Inside the DMA, a strong negative electrical potential deflects positively charged exosomes towards a collection slit. The exact deflection trajectory towards the collection slit depends on electrical and drag forces on the particles. The electrical force is constant for a vast majority of attracted exosomes because the neutralization process left them with the same charge of +1. Therefore, at a given potential only the drag force (which changes linearly with the particle diameter) and the particle shape determine which particles pass through the collection slit and are counted one-by-one inside the condensation particle counter (CPC; TSI Model 3025A). The result is expressed as the average number of particles analyzed per volume of inlet gas at a flow rate of 1.0 L/min over 20 seconds. By sweeping the bias potential from 1.7 to 2.5 kV and assuming that the desiccated exosomes are spherical particles, we characterized their size distribution in the range from 20 to 82 nm in 1 nm increments. Alternatively, by maintaining a constant potential, a narrow size fraction can be directed from the DMA into an electrostatic deposition chamber and deposited on a substrate for subsequent analysis.

6.3.2.3 Cryo-Transmission Electron Microscopy (Cryo-TEM)

The imaging procedure was described in detail previously.[31] Briefly, prior to cryo-TEM imaging, the exosome samples were diluted 1:100 in DI water. Approximately 3.5 μL of sample was placed on a holey carbon-coated copper grid. The unstained sample was vitrified with the aid of a robotic accessory (FEI Vitrobot, Hillsboro, OR) used to plunge freeze the aqueous sample into liquid ethane maintained at the temperature of liquid nitrogen. Once vitrified, the samples were stored in liquid nitrogen. Prior to image acquisition, the stored samples were transferred to a cryoholder (Gatan 626, Pleasanton, CA), which maintained their temperature at approximately -180^{o}C during imaging. The 2048×2048-pixel cryo-TEM images were obtained at 200kV using FEI Tecnai F20 transmission electron microscope (Hillsboro, OR) coupled to a FEI Eagle CCD camera and sized using the same MATLAB image analysis algorithm as the one used in SEM sizing. Particles were also sized manually using MATLAB Image Processing Toolbox for comparison.

6.3.2.4 Dynamic Light Scattering (DLS)

The samples were diluted 1:100,000 in DI water and filtered through 0.2 μm syringe filters (Corning, Tewksbury, MA). Prior to the measurements, 1 mL of the sample preparation was placed into a low volume disposable sizing cuvette for analysis and given 5 minutes to reach 25°C. The DLS measurements were performed on a Malvern Zetasizer Nano ZS (Worcestershire, UK) at 173° angle which measures particles in the 0.3–10,000 nm size range. Water viscosity at 25°C (0.8872 cP) and the refractive index of the solution equal to 1.33 were used to interpret the measurements. The refractive index for exosomes was set to 1.35. Samples were analyzed in 3 repeats, each

consisting of 12 scattering measurements. The obtained data were processed using a General Purpose Model implemented in the Zetasizer software to obtain the size distribution, its mean and the standard deviation.

6.3.2.5 Nanoparticle Tracking Analysis (NTA)

NTA was performed using Nanosight instrument (model LM10; Salisbury, United Kingdom) by illuminating the sample with a 40 mW violet laser (405 nm wavelength), capturing the light scatted by exosomes with a high-sensitivity sCMOS camera (OrcaFlash2.8, Hamamatsu C11440), and analyzing the results using the software provided by the manufacture (Nanosight Version 2.3). The minimal expected particle size, minimal track length, and blur size were set to Auto, gain set to 1, brightness to 0, and detection threshold set to 10 Multi. The viscosity of DI water depends on temperature and was adjusted automatically based on the temperature measurements. Temperature of the cell was measured manually and stayed at 20°C with a maximum of 0.1 degree fluctuation throughout the nanoparticle tracking. Viscosity of water at these temperatures is nearly constant and equal to 1cP. Prior to analysis, the exosome samples were diluted 1:1,000 in DI water and allowed to equilibrate to room temperature (20°C). Water used in dilution was filtered using Nanopure Filtration System (Thermo Scientific Inc, Waltham, MA) and stored in a glass container prior to use. Samples were analyzed within 5 minutes of the initial dilution. Using a 1 mL sterile syringe, each sample was injected into the test cell. Approximately 35 particles were observed in the field of view and the typical concentration was approximately 5×10^{8} particles/mL for each measurement. A 60-second video was recorded for each sample at 20 frames per second with 25.98 millisecond shutter speed and camera gain set to 512 and analyzed using NTA software with the

described settings. Each video consisted of more than 1000 frames and the total of valid particle tracks for each 60-second measurement was ~1200. The video data characterizing hydrodynamic mobility of particles in the field of view were analyzed with the NTA software which reported the exosome size distribution, its mode, mean and the standard deviation.

6.3.2.6 Data Analysis

Size-frequency measurements for a given sample obtained with different techniques were converted into the probability density functions (pdf) of particle sizes expressed as a histogram. The width of a data bin, h, in each histogram was calculated as $h = 3.5\sigma/n^{\frac{1}{3}}$, where n is the number of sized exosomes having diameters in the range characterized by the standard deviation σ. The hypothesis that medians of two distributions are different was tested with 95% confidence, assuming that the size measurements were normally distributed. The testing was found to be robust to the type of the assumed distribution. Specifically, the outcome of the test did not change when the assumption of normality was changed to the assumption that size measurements were log-normally distributed.

6.4 Results

6.4.1 Hydrodynamic Sizing

We measured the size distribution of exosomes in solution by nanoparticle tracking analysis and dynamic light scattering. For spherical particles, both techniques estimate hydrodynamic diameters based on the measurements of particle mobility in liquid. The insert in Figure 6.1b is a typical frame of a NTA video sequence of the

particle motion captured by the CMOS sensor. The spots in the image are formed by scattered laser light collected by a 20× optical objective. The temporal motion of each particle is used to estimate its diffusivity; the corresponding hydrodynamic size is found from the Stokes-Einstein equation. The results for individual particles are then summarized as the size distribution of the particle populations. Figures 6.1a and 6.1b, respectively, show the size distributions of exosomes (scaled to represent probability density functions, pdf) from a healthy woman control and a woman with pancreatic cancer measured by NTA. The mode for the control sample was 136 nm compared to 121 nm for the sample from the pancreatic cancer patient, while the mean size (plus or minus standard deviation, std) for the control sample was 182±79 nm compared to 157±72 nm for the pancreatic cancer sample. The exosome concentration in the control sample was 5.00×10^{11} particles/mL and higher (5.41×10^{11} particles/mL) in the patient sample.

The same samples analyzed by DLS gave similarly broad size distributions (Figure 6.1c and 6.1d). The mode and mean for the control was 91 and 119±47 nm compared to 92 and 130±55 nm for the patient sample.

6.4.2 Geometric Sizing of Hydrated Exosomes by Cryo-TEM

Figures 6.2a and 6.2b show typical cryo-TEM images of exosomes in control and pancreatic cancer patient samples, respectively. The imaged particles are unstained, yet sufficient contrast was present to identify particle boundaries. Algorithmic image analysis identified and sized 106 exosomes derived from the control sample and 212 patient exosomes. The exosomes appear as close to circular projections, with mean eccentricities equal to 0.334±0.084 and 0.290±0.085 for control and patient exosomes, respectively. Algorithmic analysis (illustrated in Figures 6.2 and 6.3) shows that the geometric mean

diameters of exosomes derived from the control sample are in the range between 26 and 129 nm and patient exosomes are in 25-98 nm range. The size distributions for the two samples are shown in Figure 6.2c. The average diameter plus or minus the standard deviation was found to be 71±24 nm for the control and 55±14 nm for the patient sample when using this analysis method. Consistent with the NTA results, the concentration of patient exosomes was observed to be higher and their tendency to cluster was notable.

Visual inspection revealed that a larger number of exosomes was present. The undercount during algorithmic analysis occurred because exosomes were on or between carbon supports and some were clustered together, especially in the patient sample. White arrows in Figure 6.3a indicate particles that were not identified as such by computer image analysis. As a comparison with algorithmic quantification presented in Figure 6.3, manual sizing of all visually identified exosomes was carried out. Figures 6.3a and 6.3b illustrate the process used to manually size the enlarged images of the exosomes with the aid of the MATLAB Image Processing Toolbox. In total, 173 control and 355 patient exosomes were observed visually. The size distribution based on manual sizing and its comparison with the results of computer analysis are given in Figure 6.3c and Table 6.2. The tendency of manual sizing to estimate smaller exosome diameters is caused by underfocusing in cryo-TEM images, which leads to coronal appearance of exosome membranes. Individuals performing manual sizing tend to ignore these coronas when estimating the size of exosomes (see Figure 6.3b for examples) and estimate smaller sizes than identified by computer analysis (Figure 6.3d). Figure 6.3d shows ellipses that the automatic image analysis algorithm fitted to the three exosomes seen in Figure 6.3c, and their calculated sizes and eccentricities. For the largest exosomes in Figures 6.3b and

6.3d, Figure 6.3e shows the major and minor lengths of the fitted ellipse, the corresponding eccentricity, and the diameter calculated as the geometric mean of the two lengths. Manual analysis was not robust in identifying major and minor axis; therefore, the manual results were reported as a single number for each particle. It was noted that manual results varied with the rotation of the image on the computer screen. Despite the tendency of manual sizing to produce smaller size values, the comparison of distributions in Figures 6.3c shows that, both, algorithmic and manual sizing produce consistent results.

6.4.3 Geometric Sizing of Desiccated Exosomes

6.4.3.1 SEM

A representative SEM image of desiccated exosomes is shown in Figure 6.4a. In total, 8 SEM images of the patient and 17 images of a control sample were used to size the exosomes. The histograms in Figure 6.4b show the sizing result obtained from the analysis of 24,024 control and 12,298 patient exosomes. The mean (± standard deviation) sizes were found to be 52±21 and 50±18 nm for the control and patient samples, respectively.

Image analysis of these desiccated samples revealed dependence of exosome sizes on their spatial location within the perimeter of the dried sample. This can be seen in Figure 6.4c, which shows the particle size segregation, from larger to smaller, as we move diagonally away from the upper left corner of the image. Quantification of this change given in Figure 6.4d shows a rather significant change in exosome sizes in the four areas of the image. In the top left corner, the exosome sizes are in the range from 50 to 80 nm and decrease to the predominant sizes of 20-50 nm as we move towards bottom

right area of the image. Such size segregation of exosomes as a result of drying has not been previously reported. It is likely related to the coffee ring effect[32] known to occur when a suspension of particles dries on a surface. For the case of micrometer particles, the deposition pattern depends on capillary flow in the drying drop[32] and roughness of the surface on which desiccation occurs.[33] Deposition also depends on several characteristics of the particles themselves – their size, shape,[34] surface activity and the presence of other surface-active compounds in the solution.[35] These same factors likely influence the deposition of exosomes during surface desiccation of the sample. The observed coffee ring phenomenon with size segregation suggests that, to avoid bias in characterizing the concentration and sizes of surface-deposited exosomes with techniques like SEM, TEM and AFM, the entire area of the dried sample should be imaged and analyzed.

6.4.3.2 DMA

The ES-DMA sizing results are shown in Figure 6.5. Particles with diameters less than 20 nm were observed but were attributed to the contribution of macromolecules, such as globular proteins, lipids, lipoproteins, and agglomerates (dimers, higher order oligomers, etc.) thereof.[36] For this reason, only particles larger than 20 nm were considered to be exosomes in the DMA results. This decision is supported by cryo-TEM and SEM results that show that very few exosomes smaller than 20 nm are present. An even more direct justification is provided by TEM imaging of DMA-deposited exosomes in Figure 6.6. The exosomes desiccated inside the DMA were deposited on a carbon grid and imaged by conventional TEM. The purpose of this experiment was to confirm that: a) Aerosol-desiccated exosomes are larger than 20 nm, thus justifying the 20 nm cutoff of

the DMA size distribution and b) Isotropic drying largely preserves innate spherical shape of exosomes.

Exosomes were isolated from the serum of a 66-year-old male pancreatic cancer patient (concentration of the CA19-9 tumor marker equal 234U/mL) using the ExoQuick kit, as described previously. The isolated exosomes in ammonium acetate buffer were electrosprayed, dried, and partially neutralized to a predominant ±1 elemental charge per particle. They were then entrained by the gas flow of 30 L/min and a positively charged fraction corresponding to ~ 30 nm diameters was deflected into a collection slit in the electrode maintained at electrostatic potential equal to −1,531 V. A 1.0 L/min sample flow of particles collected through the collection slit were sent into an electrostatic deposition apparatus (Figure 6.8C) where they were deposited on a TEM grid placed on the electrode maintained at −10 kV voltage. A sample of imaging results is shown in Figure 6.6. Predominantly circular projections of exosomes are preserved after electro-spraying and airborne desiccation (mean eccentricity of 194 exosomes visualized by TEM after their deposition through the DMA was 0.420±0.175), as would be expected for near spherical particles randomly deposited on the surface from the gas phase. Figure 6.7 shows eccentricities for all exosomes observed in TEM images. It also shows that their sizes remained above 20 nm. Smaller than 20 nm particles seen in DMA measurements do not clearly appear on TEM images, which is consistent with a lower density of biomolecular complexes. The surface concentration of deposited exosomes was relatively low, with only few TEM images showing three or more particles per image. The size distribution with 20 nm cutoff seen in Figure 6.5 is based on the condensation particle count of 5.50×10^6 particles from the patient sample and 6.22×10^6

particles derived from the control. The average diameter of control and patient particles was 37±12 and 40±12 nm, respectively.

6.5 Discussion

6.5.1 Influence of Exosome Isolation Method

Exosome sizes overlap with other biological particles.[37] Specifically, lipoprotein and protein agglomerates overlap with exosomes in the lower range of size distribution, while larger extracellular microvesicles and cell debris interfere with exosome sizing at the high end of their sizes. Therefore, the exosome isolation method has an influence on the population of the isolated particles and thus affects the sizing results.

Exosome isolation is not a standardized procedure and the benefits of different alternatives are hotly debated. Differential ultracentrifugation remains the most widely used approach, followed by gradient ultracentrifugation and precipitation techniques,[38] like ExoQuick employed by us. Numerous studies have been conducted to reveal the influence of the isolation methods on the population of the isolated exosomes and the contamination of the isolated samples by soluble proteins, molecular complexes, and extracellular vesicles other than exosomes.[15,18,19,38,39,40] For example, Van Deun et al.[38] used three different isolation methods – UC, gradient centrifugation, and ExoQuick – to isolate exosomes produced by MCF7 breast cancer cell line transfected to stimulate exosomal production. They found that isolation used has an effect on proteomic and nucleic content of the sample, as well as the concentration and size distribution of isolated particles. They concluded that certain gradient fractions obtained with iodixanol-based gradient UC produce exosome samples most enriched in CD63 and other exosomal marker proteins, lowest contamination by extravehicular proteins, and distinct mRNA

profile. However, it is not clear if the same narrow density fraction contain exosomes produced by different cell lines and whether the exosome-rich density band remains narrow in more complicated cases of heterogeneous exosomes secreted by many different types of cells and contained in biological fluids. A recent result shows that most individual exosomes do not carry biologically significant numbers of miRNAs,[6] which suggests nonuniform distribution of nucleic material across the population and varying density between exosomes. This is further supported by Jeppesen et al.[40] that found different exosome subpopulations characterized by variable sedimentation characteristics. Reliance on protein biomarkers to verify quality of exosome isolation has also been questioned because not all exosomes express such marker proteins as PDCD6IP, TSG101, CD9, CD63, and others.[41] For exosomes secreted by RBL-2H3 cells, it was reported that only 47%, 32%, and 21% of exosomes contain CD63, MHC II, and CD81 markers, respectively.[42] As another example of variability in proteins biomarkers, Bobrie et al.[43] reported evidence of heterogeneous vesicle populations and different proportions of CD63, CD9 and Mfge8 markers in exosomes isolated in sucrose gradients at "classical" densities of ~1.15 g/ml. To confirm this we conducted CD63 measurements in the two studied patient sample by using an ExoELISA kit (System Biosciences, Mountain View, CA). In short, the exosome samples were diluted 1:2 in the exosome binding buffer and incubated at room temperature for 10 minutes. Exosome protein samples and 50 µL of prepared protein standards were placed in a micro-titer plate and allowed to incubate at 37°C for 2 hours. After incubation, the plate was inverted to empty all contents and washed 3 times with 100 µL 1x wash buffer. To each well, 50 µL of the exosome specific CD63 antibody was then added and incubated at room temperature for

1 hour with shaking. The plate was then washed 3 times with 100 µL of 1x wash buffer, and 50 µL of exosome validated secondary antibody was added to each well and incubated at room temperature for 1 hours with shaking. The plate was then washed 3 times with 100 µL of the wash buffer and 50 µL of super-sensitive tetramethylbenzidine (TMB) ELISA substrate added and allowed to incubate at room temperature for 30 minutes with shaking. To fix the endpoint for the assay 50 µL of stop buffer was added and CD63 quantification done by using a spectrophotometric plate reader (Synergy HT, BioTek, Winooski, VT) at 450 nm absorbance. It was determined that only 17% and 21% of exosomes expressed CD63 on the surface in the normal and cancer sample, respectively. This confirms that CD63 is not the best exosome marker.

ExoQuick was compared with exosome isolation by ultracentrifugation in the study of Caradec et al.[39] It was concluded that ExoQuick provides an efficient and reproducible method for exosome isolation for quantitative studies, whereas UC does not. They reported that for sera samples both methods isolate exosomes equivalently expressing several exosomal markers but UC preparations were strongly contaminated by proteins (albumin and IgG). Rekker et al.[18] examined UC and ExoQuick isolation of exosomes for the purposes of miRNA profiling. They concluded that both methods are suitable for use with sera samples, but noted that the exosomal miRNA profile is slightly affected by the isolation method.

While the influence of isolation techniques has not been investigated in the current study, literature reports indicate that it is an important factor contributing to the reported size variability of exosomes. The source of the exosomes, by biological fluids or

cell lines, was also not examined, but is likely a contributing factor to the variability seen in Table 6.1 and other studies.

6.5.2 Exosomes are Spherical Bioparticles

In the vitrified state, the properties of the exosomes are similar to those observed at biological conditions. Cryo-TEM images are formed by electrons transmitted through vitrified sample (Figures 6.8A) and give two-dimensional projections of three-dimensional exosomes in their native hydrated state. Our results show that these projections are close to circular for both patient and control exosomes (mean eccentricities equal to 0.290±0.085 and 0.334±0.084, respectively). This finding is consistent only with a near spherical shape of exosomes. It contradicts common claims that exosomes have a "cup shape"[23] (as illustrated in Figure 6.8D) reported based on electron microscopy imaging of desiccated samples[12,44,45,46] and atomic force microscopy of both hydrated and desiccated exosomes.[47–49] Our finding is supported by prior cryo-TEM results that report round morphology[50] of exosomes released by hepatocytes, spheroid shape[51] of human mesenchymal stem cell exosomes, and naturally spherical[52] exosomes secreted by prion-infected cells. The cup shaped morphology of exosomes was questioned before. For example, van der Pol et al.[53] noted that "identification of exosomes based on their cup-shaped morphology after negative staining and visualization by TEM seems questionable." Our results confirm this suspicion. We furthermore suggest a mechanism that explains this artifact by nonuniformity of capillary forces during surface desiccation, as discussed below.

The conclusion that the innate shape of exosomes is spherical should be taken into account when sizing is performed by techniques that produce shape dependent results.

For example, because particle mobility in a liquid or electrical field is shape dependent, exosome sizing by NTA, DLS (Figure 6.8B), or DMA (Figure 6.8C) should account for their shape as being spherical, as we have done in this work. Furthermore, the shape distortion away from spherical at the sample preparation step – for example, due to electrostatic forces used to immobilize exosomes on a charged substrate prior to AFM characterization or surface desiccation prior to EM imaging – will likely affect the measured sizes and require correction for such distortion.

6.5.3 Exosome Sizing Is Method Specific

Of the three factors contributing to size variability – the difference in exosome sources, isolation techniques, and sizing methods – only the latter was present in this study. Nevertheless, as illustrated by the summary of the sizing results in Figure 6.9 and Table 6.3, the difference in sizing techniques alone introduces variability consistent with what was observed when all three factors were present (Table 6.1). Specifically, the obtained average size by NTA falls within the range reported by others for sample isolated from different sources;[17,54,55] the average sizes obtained by the SEM and cryo-TEM imaging are also consistent with prior observations which report average sizes in the 40-60 nm range[17,48,55] when electron microscopy was used to size exosomes. Sizing by the DMA gives the average size of exosomes at approximately 40 nm, which is the smallest average size found with any technique. The difference in sizing results by different techniques provides an important insight into biophysical properties of exosomes, the understanding of which requires a closer look at physical principles employed in exosome sizing.

6.5.4 Measurements of Hydrodynamic Sizes

Nanoparticle tracking analysis[17,54] (which has emerged as the most widely used method for characterizing the size distribution and the concentration of exosomes) and dynamic light scattering both estimate hydrodynamic (liquid mobility) size of particles (Figure 6.8B). The hydrodynamic size is obtained by first estimating particle diffusivity in the solution and then calculating the corresponding particle diameter to match the observations. NTA estimates diffusivity separately for each particle in the field of view of the instrument by measuring particle displacement over time. Unlike the NTA, dynamic light scattering[56] – another commonly used exosome sizing method – is an ensemble technique that estimates the hydrodynamic size distribution of the entire particle population by analyzing the temporal variation in the intensity of the scattered light measured at a fixed scattering angle. If we ignore the contribution of a solvation layer formed around particles due to changes in hydrogen bonding of water molecules at the particle-solvent interface,[57,58] the hydrodynamic and geometric sizes will be equal for smooth, hard, electrically neutral, spherical particles with zero surface charges. Several of these assumptions fail in the case of exosomes, which are elastic particles known to have a negative surface charge[44] and have a membrane with conjugated macromolecules. In an aqueous solution, any particle with a surface charge is surrounded by an electrical double layer, sometime referred to as an ionic atmosphere.[59] As the particle moves, the ionic atmosphere moves with it, making a particle's apparent size larger than its physical size. The thickness of the ionic atmosphere is approximately equal to the Debye length, which depends on ionic strength and dielectric permittivity of the solution.

Surface-conjugated macromolecules also exert strong influence on particle diffusivity. To complicate matters further, the configuration of such surface decoration (e.g., its lateral extension) may change with the concentration of surface ligands, ionic strength of the solution, its pH and, the type of parent cells that secreted the exosomes.[60]

6.5.5 Geometric Sizing of Exosomes

6.5.5.1 Desiccated Samples

Too small for light microscopy, exosomes can be directly imaged by electron microscopy. The traditional EM (scanning and transmission) characterizes samples in vacuum after exosomes are desiccated on a surface. Exosomes desiccated in the gas phase may be characterized based on their electrical mobility inside differential mobility analyzers. Drying, either on a surface or in a gas phase, introduces severe environmental transformation of biological samples. Figure 6.8C and 6.8D illustrates that a change in interfacial forces during desiccation likely alters the shape and size of exosomes measured by EM, AFM, and DMA. As discussed below, these changes depend on whether the desiccation occurred on the surface or in the gas phase.

6.5.5.2 Hydrated Samples

Few options exist to characterize geometric sizes of hydrated exosomes, of which cryo-TEM[61] is the gold standard. Prior to imaging, a thin sample of hydrated exosomes is pipetted on the TEM grid and blotted to remove excess liquid. The sample is then plunged into liquid ethane to impose rapid cooling needed to obtain the vitrified (amorphous) form of ice, which has properties similar to liquid water.[61] In addition to the complexity of sample preparation, another notable disadvantage of the cryo-TEM

imaging is a relatively small number of exosomes seen in each acquired image. Consequently, the number of exosomes used to characterize the size distribution is small and only the range of their sizes is often reported in the literature (Table 6.1).

Atomic force microscopy can be used to visualize the three-dimensional topography of hydrated biological particles. Prior to imaging in the solution, the particles must be immobilized on a substrate, by either tethering to a functionalized surface, trapping in a filter, or by electrostatic attraction to a charged surface. The negatively charged exosomal membrane makes electrostatic surface fixation particularly convenient. Note, however, that the same electrostatic forces that immobilize exosomes on the surface likely distort their spherical shape.

6.5.5.3 Hydrodynamic Size of Exosomes Is Substantially Larger than their Geometric Size

In view of the discussed differences, it is expected that the hydrodynamic size of exosomes will always be larger than their geometric size. The degree to which the measured hydrodynamic size exceeds their geometric size is, however, surprising. With reference to Figure 6.9 and Table 6.3, we see that the mean hydrodynamic diameter measured by NTA and DLS is in the range between 119 and 182 nm for both patient and control samples, compared to 37–71 nm range of average geometric sizes of hydrated and desiccated exosomes. Under the conditions of our experiments, the formation of the electric double layer alone cannot explain this very large difference. The factor most likely responsible for substantially larger hydrodynamic size of exosomes observed by us is their membrane-conjugated macromolecular decoration, which may include transmembrane and tethered proteins; lipids; and saccharides, as well as functional and

self-assembled surface-active compounds present in biological fluids and cell growth medium. We observed faint excess density around some exosomes (Figure 6.2d, arrows) that suggests the presence of such molecular decoration on the surface of these particles. The interaction of surface molecules and complexes with a biofluid or buffer impedes the mobility of exosomes, which increases their hydrodynamic size to the extent consistent with our observations. A similarly large increase in a hydrodynamic size due to surface decoration was observed after PEGylation of gold nanoparticles,[62] which increased their hydrodynamic diameters to 75±33 and 122±50 nm from the initial 38 and 89 nm geometric diameters, respectively. To test this hypothesis exosomes were isolated from MCF7 breast cancer cell line by using ExoQuick-TC. The isolated exosomes were resuspended in 1x PBS and kept at -80°C until analysis. To remove proteins from the exosome membrane half of the sample volume was exposed to proteinase K enzyme that preferentially breaks down proteins in locations of hydrophobic, aliphatic and aromatic amino acids. In short, 10μL of proteinase K was added to 30μL of MCF7 exosomes resuspended in 1x PBS and incubated for 1 hour at 37°C. The sample was then spun at 15,700g at 4°C for 1 hour. The pellet was then resuspended in 30 μL of 1x PBS and supernatant saved. The samples were then analyzed using NTA on the same day by conducting five 60 second measurements per sample. Mode and mean exosome size in the original MCF7 sample were measured to be 86 ± 3 nm and 110 ± 6 nm respectively (Figure 6.11) while mode and mean size of exosomes in the MCF7 sample exposed to proteinase K were measured to be 59 ± 1 nm and 65 ± 2 nm, respectively. The hydrodynamic size clearly decreased when exosomes were shaved from membrane proteins and became closer to geometric exosome size discussed earlier. This allows us to

conclude that membrane proteins, although present, are difficult to identify during cryoTEM analysis while they clearly contribute to exosome mobility and hydrodynamic size. The contribution of membrane proteins was not investigated further.

6.5.5.4 Effect of Aerosol and Surface Desiccation on Exosome Shape and Size

Differential mobility analysis characterizes exosome sizes after they were rapidly desiccated while suspended in gas. The drying front in an airborne exosome progresses isotropically in the exosome's radial direction, as illustrated in Figure 6.8C. This balances the capillary forces during desiccation and minimizes shape distortion of desiccated exosomes away from their hydrated spherical shape. To confirm that isotropic drying largely preserves innate spherical shape of hydrated exosomes, the aerosol-desiccated exosomes were imaged by conventional TEM (Figure 6.6). Though some exosomes showed signs of shape distortion after experiencing electrospray atomization, aerosol-desiccation, and surface impact with the deposition surface, Figure 6.7 indicates that they maintain close to circular two-dimensional TEM projections (mean eccentricity equal 0.420±0.175), as would be expected if close to spherical shape was maintained.

Surface desiccation, unlike aerosol drying, proceeds with a nonisotropic front. This leads to unbalanced capillary forces that likely distort the shape of desiccated exosomes to produce the often observed cup shape of surface-desiccated exosomes, as conceptualized in Figure 6.8D. Two symptoms of shape distortion were observed. First, as Table 6.3 shows, the eccentricity of surface desiccated control (patient) exosomes increased to 0.493±0.313 (0.540±0.260) from 0.334±0.084 (0.290±0.085) for hydrated exosomes observed by cryo-TEM. The second observation is that, when spherical shape

is distorted by desiccation on the surface, the two-dimensional projection of SEM-imaged exosomes would be expected to be larger than the diameter of spherical aerosol-desiccated exosomes. This is exactly what we see in Figures 6.9 and 6.10, which show with 95% statistical confidence that diameters of aerosol-desiccated exosomes, measured by DMA, are smaller than the SEM size measurements of surface-desiccated exosomes.

6.5.5.5 Effect of Osmolarity on Exosome Sizes

Several analytical techniques employed by us require that the concentration of solute in the exosome suspension is low. This, for example, is necessary to avoid crystal and precipitate formation that affect SEM imaging and DMA characterization. To maintain consistency, solution of low osmolarity was also used with other sizing techniques, even when not required. Lower osmolarity of the solution in which exosomes are suspended, in our case osmolarity being ~0 mOsm/kg, compared to their luminal osmolarity (~280-300 mOsmol/kg) creates an osmotic pressure acting to cause swelling of exosomes (hypotonic condition). This pressure may eventually be relieved after the osmolarity is equilibrated by the transport of water and solutes across the membrane. Such equilibration is expected to be rapid due to the small size of the exosomes but may cause exosome lysis due to the large osmotic pressure.

To investigate if the transient change in the pressure across the exosomal membrane leads to a permanent change in their sizes, we isolated exosomes from serum of a 66-year-old male pancreatic cancer patient (sample 280) and a supernatant of the MCF7 breast cancer cell line grown in exosome-free medium (Figure 6.12). The isolation of serum exosomes was carried out using the ExoQuick kit, as described before, while the cell line exosomes were isolated using a specialized kit, ExoQuick-TC. The equal

aliquots of the isolated exosomes were suspended in DI water and PBS; their concentration and sizes were then characterized by the NTA. Table 6.4 shows that, within experimental error, the concentration of exosomes was unaffected by suspension in either PBS or DI water. We can therefore conclude that exosomes are not lysed by osmosis after their suspension in DI water. Lysis might not occur due to high curvature of the exosome membrane which may allow ions to freely diffuse out under the hypotonic condition although stress-induced pore formation, leakage and eventual ionic equilibrium inside and outside of the vesicle may also be contributing to exosome stability but further investigation will be needed.[63–65] Inspection of sizing results given in Table 6.4 and Figure 6.12 suggests that, within standard error of the experiments, low osmolarity and potential equilibration still leads to small swelling of the exosomes. Noting that transport of inorganic ions is a regulated process in semipermeable plasma membranes, the observed change may be explained by an incomplete equilibration of ionic concentration across the membrane, which would lead to a net transport of water and, thus, swelling. However, the observed size change is small relative to sizing differences introduced by different analytical techniques and was not further investigated in this study.

6.5.5.6 Application of AFM for Hydrated and Desiccated Exosome Sizing

As mentioned previously there are only a few methods capable of imaging nanoparticles in both hydrated and desiccated state with good enough resolution. The current gold standard that is able to do so is cryo-TEM and TEM for hydrated and desiccated sizing, respectively. Another available method is ESEM (Environmental Scanning Electron Microscopy) which can be used to keep the particle hydrated

providing hydrated size and SEM providing size of the desiccated particles. There are numerous disadvantages of each of these methods due to complexity of sample preparation and image acquisition as well as lower resolution. For example, ESEM cannot provide good enough resolution below 100 nm and sample preparation is complex. In addition, both TEM and SEM are only able to measure the desiccated size of particles when they dry on the surface which leads to nonuniform desiccation (Figure 6.8D) as well as difficulty in identifying the particles due to other debris. Finally, the provided methods are time consuming and expensive.

AFM is an alternative method having high potential for exosome characterization. Although several authors reported AFM application for exosome characterization,[48,66,67] no reliable protocol was found for sample preparation and imaging, especially for exosomes in the liquid. This motivated us to develop a simple yet reliable protocol for exosome imaging.

Exosomes were previously shown to have a negative zeta potential which allows us to conclude that the surface is negatively charged and is most likely due to the phospholipid membrane.[55] To confirm this, a zeta potential was measured by us using Malvern Zetasizer Nano ZS (Worcestershire, UK) in 1x PBS and an average of -20mV was obtained for samples used in this study. Presence of this charge can allow fixation of exosomes on a given surface which is mandatory for AFM imaging. To take advantage of this feature the surface should be positively charged and have insignificant roughness for high resolution imaging. Freshly cleaved mica naturally provides a smooth (<0.3 nm roughness) negatively charged surface.[68,69] To modify the surface charge, 100µL of 10mM $NiCl_2$ (Sigma-Aldrich, St. Louis, MO) prepared in DI water was pipetted on the

freshly cleaved 10mm diameter mica (Ted Pella Inc, Redding, CA) surface and allowed to stay at room temperature for 10 seconds (Figure 6.13). A 10mM $NiCl_2$ solution was then pipetted from mica, the surface cleaned with DI water 3 times and then gently dried with nitrogen gas. Exosomes analyzed were extracted from an MCF7 cell line by using ExoQuick-TC and serum from a 47-year-old healthy female patient who was following up for routine cholesterol testing by using ExoQuick. Exosomes were resuspended in 100μL of 1x PBS, diluted 1:25 in DI water and 100μL of the diluted sample pipetted on the freshly prepared mica. The samples were then placed in a petri dish which was then sealed and stored at 4°C for 18 hours to allow exosomes to adsorb to the modified mica surface. The unadsorbed exosomes were then removed by a pipette and mica cleaned with DI water 3 times while keeping the surface hydrated. To image in liquid 40μL of 1x PBS was then pipetted on mica or gently dried with nitrogen gas to image in air. AFM of was done using Nanoscope V controller. Imaging exosomes in the liquid was done using a triangular cantilever with 175 μm length, 22 μm width, 0.07 N/m spring constant and 20 nm tip radius while imaging in air was done using a rectangular cantilever with 125 μm length, 40 μm width, 42 N/m spring constant and 8 nm tip radius (Bruker, Billerica, MA). The mica surface with 5x5 μm area was then imaged with scan rate set to 0.8 Hz for both liquid and air samples. Acquired images were then analyzed by using NanoScope Analysis 1.4 software (Bruker, Billerica, MA).

Figure 6.14 shows an example of data acquired by using AFM. Images containing a total of 1097 and 602 MCF7 exosomes were obtained and analyzed in 1x PBS and air respectively and compared to 205 (in 1x PBS) and 501 (in air) serum exosomes. Table 6.5 shows the average diameter and height for each sample type and it can be seen that

these values agree with sizes previously obtained by others (Figure 6.1).[49,70] Exosomes which are elastic most likely deviate from a spherical shape (discussed in Section 6.5.2) primarily due to strong electrostatic forces they experience from the interaction of their negative surface charge with the positive charge of the modified mica surface. Estimating the geometry of exosomes to be half of an ellipsoid allows determining the diameter of a sphere occupying the same volume. Table 6.5 shows that the average spherical exosome diameter is close to the geometric size reported by others (Table 6.1) and earlier reported by us in this study and substantially smaller than the hydrodynamic size determined by using NTA method for exosomes coming from the MCF7 cell line which also supports the results discussed previously for the serum samples. To support this trend, TEM and TRPS were done for this cell line. Figure 6.15 shows an example of a TEM image of MCF7 cell line exosomes after negative staining. Exosomes can be identified by circular shaped particles seen in the image. After manual analysis of TEM images using ImageJ software provided by National Institute of Health (NIH), 132 exosomes were sized and the average diameter determined to be 34 nm with 7 nm standard deviation. These values appear to be close to spherical size estimated when using AFM data (Table 6.5). Tunable resistive pulse sensing was done on the MCF7 sample diluted 1:50 in 1x PBS by using qNano instrument with NP150 pore (Izon Science Ltd, Oxford, United Kingdom). The pore was stretched to the 48mm mark and applied voltage was set to 0.24 V which produced an average current of 110 nA. The mean size was determined to be 140 nm with SD = 33.5 and mode of 115 ± 4.3 nm (Figure 6.16) after analysis of 506 particles which is close to NTA results for this cell line shown in Table 6.4 although it was noted that TRPS was unable to count particles below ~70 nm so the result was inconclusive.

According to AFM results, the average size of desiccated exosomes is smaller than the average size of hydrated exosomes obtained from serum of a healthy female, while nearly no change in size is seen for the MCF7 cell line exosomes. These results may be due to the difference in membrane composition and fluidity when comparing exosomes obtained from the MCF7 cell line and serum. This may also be caused by a larger amount of cargo (e.g., miRNA and DNA) the MCF7 exosomes may contain when compared to the exosomes obtained from a healthy female, which are capable of undergoing a significant "shrinkage" when dried. This hypothesis will be studied in the future on a larger scale to obtain reliable statistics.

6.6 Conclusions

We examined the shape and size of sera exosomes in their hydrated state and after desiccation. We found that sizing results for the same sample change significantly when different analytical techniques are used to size the exosomes. The size variability between different methods is significant and consistent with the variability in sizes reported in literature for the cases when the types of cells that secreted the exosomes, the body fluids from which they were isolated, and exosome isolation methods were also the contributing factors. This conclusion places further emphasis on the need to standardize the size quantification techniques and improve our understanding of biophysical properties of exosomes responsible for the difference in sizing results obtained with different methods.

Our results indicate that the innate shape of hydrated exosomes is spherical, which implies that the commonly reported "cup shape" of exosomes is an artifact of the sample preparation steps, such as desiccation and surface fixation. Though there is a broad agreement that sample preparation and fixation steps may be responsible for

commonly observed “cup-shaped” morphology, this paper appears to be the first report that provides a mechanistic explanation of this artifact, and quantifies its influence on the reported exosomes sizes.

We report a large difference in hydrodynamic and geometric sizes of exosomes and attribute it to the presence of membrane-conjugated macromolecules that impede their hydrodynamic mobility. The difference between geometric and hydrodynamic sizes may therefore be useful in analyzing the conjugation of macromolecules to the surface of exosomes.

The method-dependence of exosome sizing extends beyond the differences in hydrodynamic and hydrated geometric sizes. For desiccated samples, we found that exosome sizing is influenced by the manner in which the drying occurs. We also found that isotropic drying during aerosol desiccation preserves the near spherical shape of the exosomes, while drying on a surface likely distorts their shapes and influences sizing results by electron microscopy, atomic force microscopy, and other techniques that require fixation on the surface for analysis. In addition, we have shown that osmolarity difference between the extracellular space and internal fluid of exosomes has no significant effect on their size and concentration, showing their stability under such conditions.

Table 6.1: Variability of exosome diameters by sizes measured and the source of exosomes.

Size measured		Method		Exosome source		Reported size (nm)		
Geometric	Hydrated	Cryo-TEM	Biofluid/ Cell type	Plasma[10]		Range: 40-200		
				Rat hepatocytes[50]		Mean=57	std=23	
			Cell culture	MLP-29[50]		Mean=40.9	std=11.2	
				THP-1[10]		Range: 30-60		
				Dictyostelium[71]		Range: 50-150		
		FF-TEM	Biofluid/ Cell type	Erythrocytes[72]		Range: 50-300		
		Liquid cell AFM	Biofluid/ Cell type	Saliva[48]	Control	Mean=67.4	std=2.9	
					Oral cancer	Mean=98.3	std=4.6	
				Malaria infected red blood cells[11]		Mean=70.6	std=3.92	
				MDA-MB-231 cells[70]		Range: 110-561		
				Saliva[47]		Lateral: 120	Height: 4	
	Desiccated	SEM	Cell Culture	HEK-293T, ECFC, MSC[55]		Range: 30-50		
		TEM	Biofluid/ Cell type	Urine[22]		Mode=45	Range:20-440	
				Placental vesicles[73]		Range: 20-60		
				Serum[74]		Range: 30-100		
			Cell culture	B16-F10[75]		Range: 50-100		
				Swan-71[76]		Range: 95-118		
		AFM	Cell culture	P12[77]		Images with no size quantification		
				MDA-MB-231 cells[70]		Mean = 38	std = 9	
				U87[49]		Lateral=89	Height = 4	
				U251[49]		Lateral=81	Height = 4	
				SKMEL[49]		Lateral=79	Height = 4	
				NHA[49]		Lateral=71	Height = 4	
						Mean	Mode	std
Hydrodynamic		NTA	Biofluid/ Cell type	Serum[17]		126	111	46
				Serum[54]		-	131.3	-
				Plasma[54]		-	134.3	-
				Placental vesicles[73]		250	Range: 40-600	
				Erythrocytes[72]		-	135	-
				Urine[78]	Female	-	134	54
					Female	-	131	51
					Male	-	172	72
					Male	-	144	54
			Cell culture	HEK-293T[55]		116	-	27
				HEK-293T[54]		-	118	-
				ECFC[55]		113	-	15
				MSC[55]		107	-	19
		DLS	Biofluid/ Cell type	Buffy coat[79]		-	54	-
				Erythrocytes[72]		Mode: 123 on-line SEC		
						Mode: 141 off-line		
			Cell culture	HEK-293T[55]		-	212	168
				ECFC[55]		-	226	157
				MSC[55]		-	208	162
				B16-F10[75]		-	74	-
				Swan71[76]		-	165	-
						Mean	Mode	std
Volumetric		Coulter	Biofluid/ Cell type	Serum[74]		120	-	-
				Uterine fluid and dissociated mucus[80]		100	-	-
				Erythrocytes[72]		135	-	-

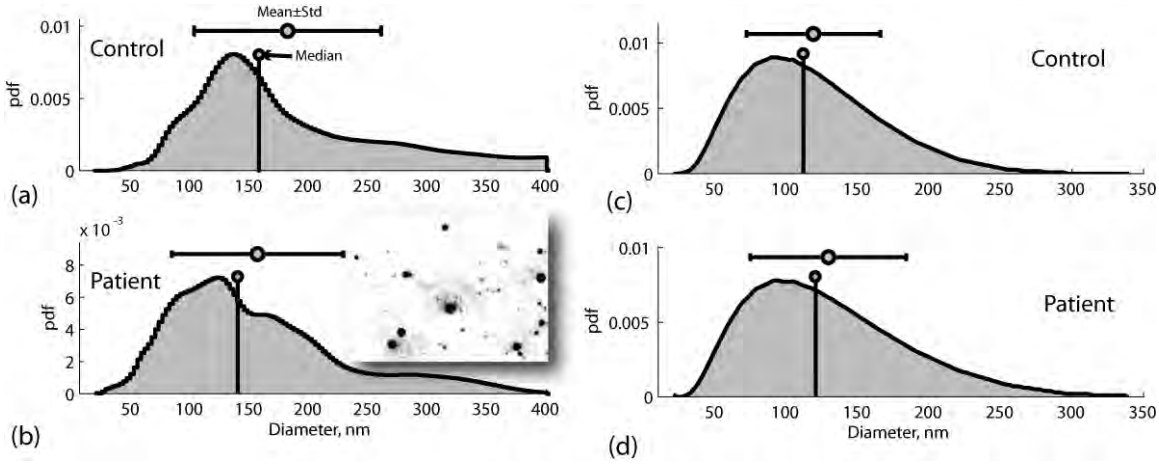

Figure 6.1: Distribution of hydrodynamic sizes (control and patient) measured by nanoparticle tracking (a,b) and dynamic light scattering (c,d).

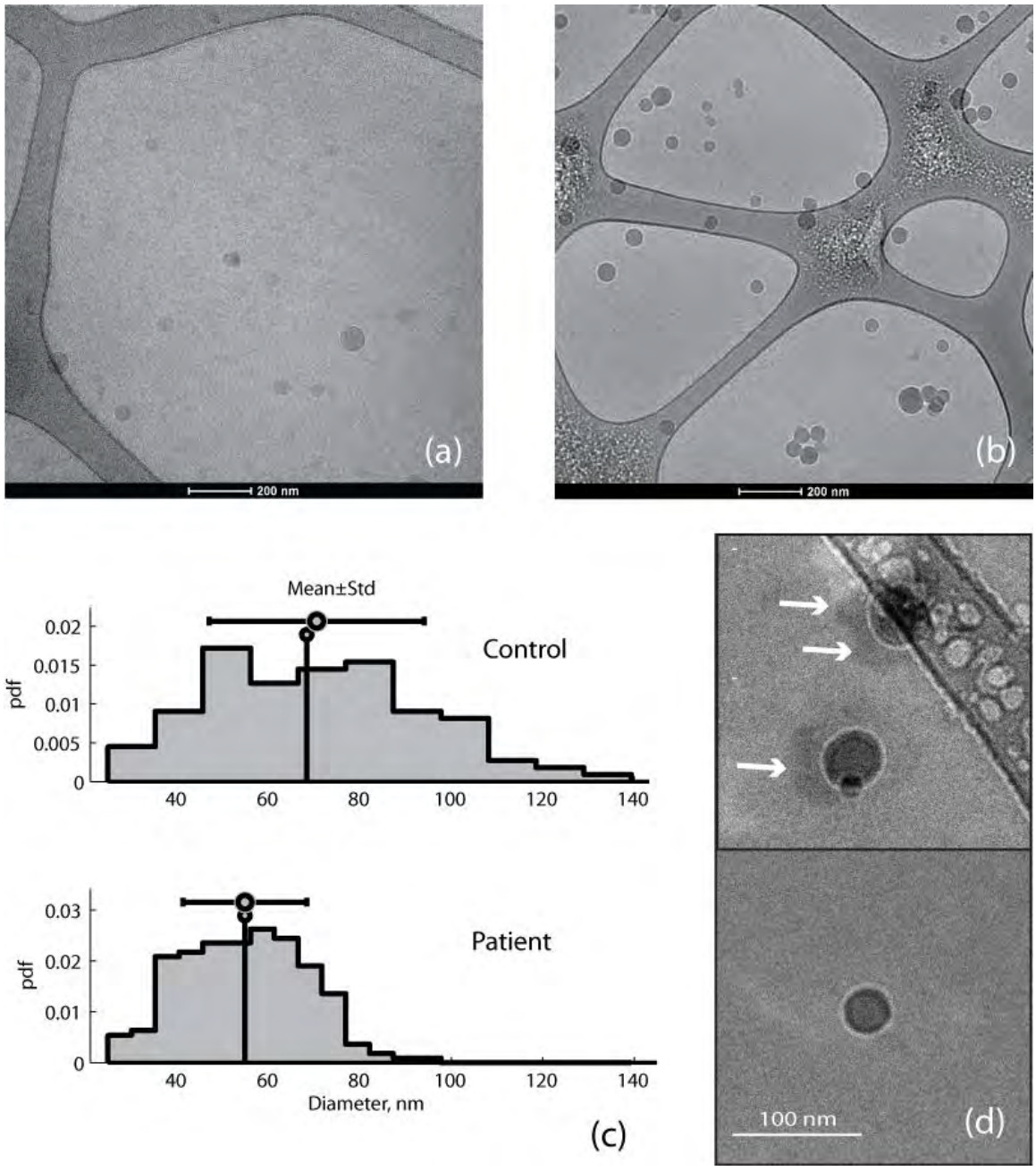

Figure 6.2: Vitrified exosomes in cryo-TEM images were isolated from the control (a) and pancreatic patient (b) samples. The web-like features in panels (a) and (b) are the carbon-support film. Note that exosomes are found on the carbon support or between supports (inside the "holes"). Two clustered groups of exosomes can be seen in the lower right quadrant of panel (b). The exosome size distribution in (c) is based on computer analysis of 106 control and 212 patient exosomes. Exosomes at the highest obtained resolution are shown in (d). Arrows show faint, extra density surrounding some particles, which suggests the presence of macromolecules conjugated to their surface.

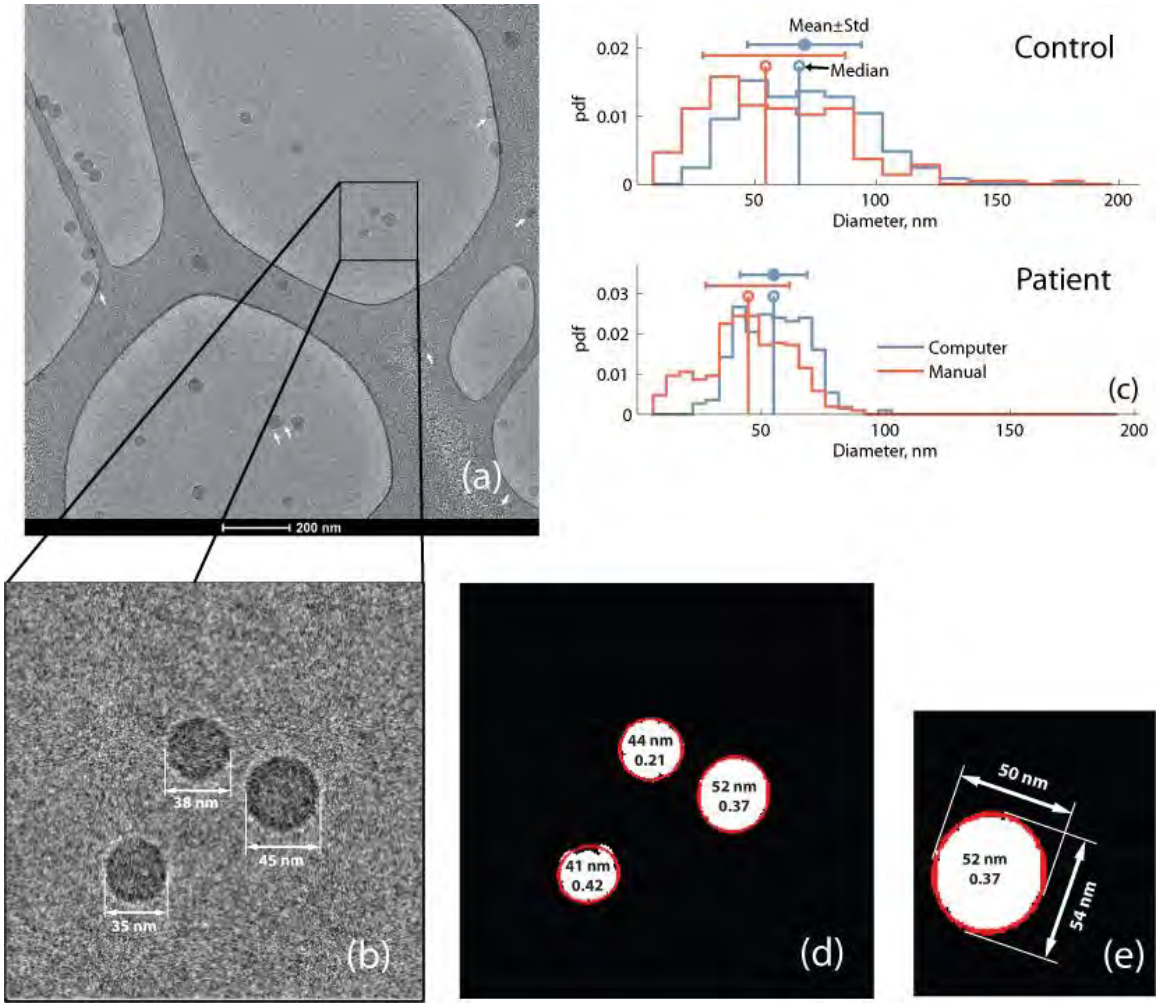

Figure 6.3: Manual sizing of exosomes observed in cryo-TEM images was carried out to validate algorithmic sizing. Exosomes in panel (a) were isolated from the patient sample. White arrows indicate particles counted manually but ignored by computer image analysis because of clustering or location on the carbon support film. Panel (b) illustrates the process used to size exosomes manually. The exosome size distributions in (c) compare the results of manual and algorithmic sizing of exosomes for control and patient samples. Panel (d) shows three ellipses fitted by the computer sizing algorithm to exosomes seen in (b). The diameters determined by the sizing algorithm are equal to the geometric mean of major and minor lengths of the fitted ellipses. These two lengths are shown in (e) for the largest exosome in panel (d). The second number inside exosomes in panels (d) and (e) is the eccentricity of each ellipse calculated by the sizing algorithm.

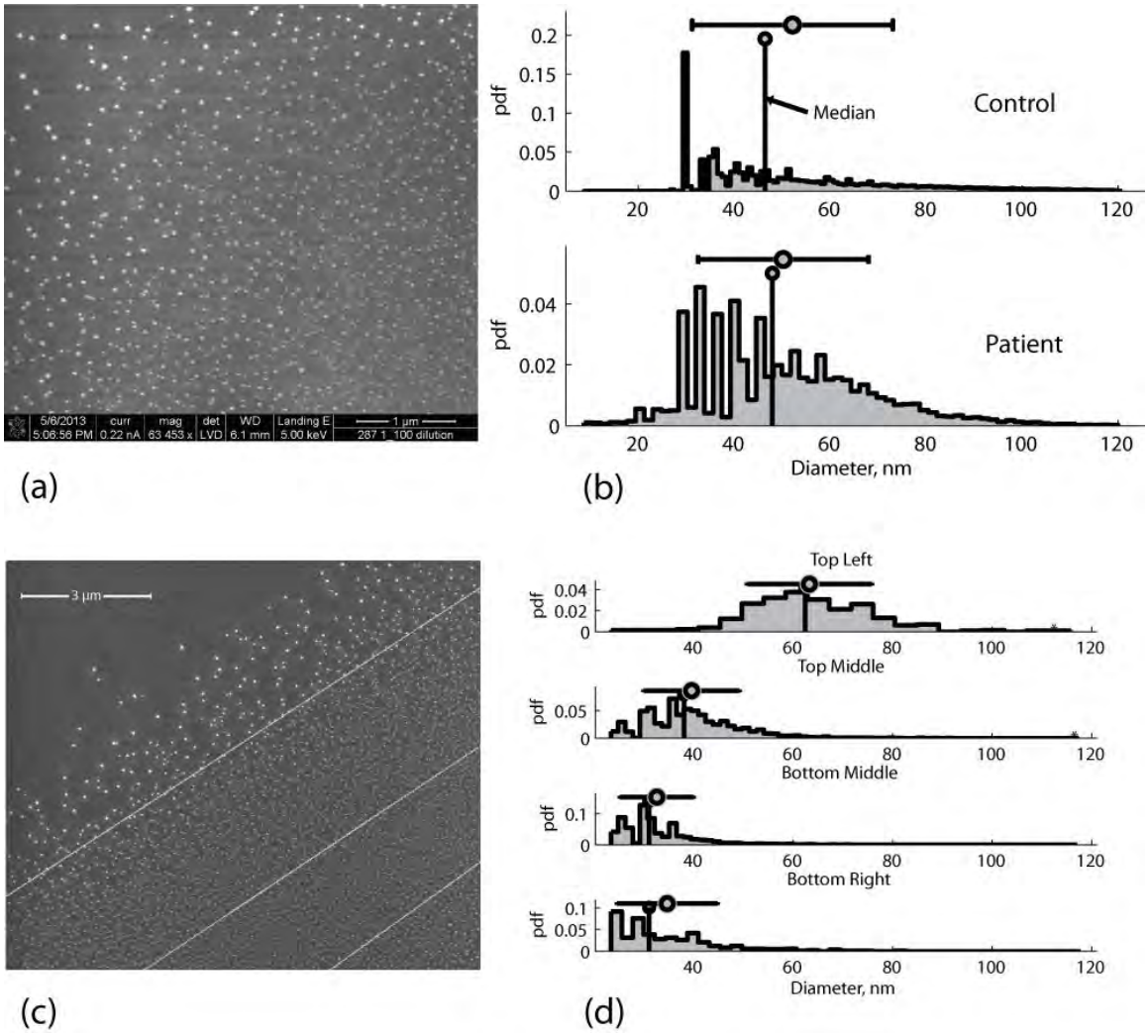

Figure 6.4: SEM results of exosome samples (a) Typical SEM image of desiccated exosomes. (b) The exosome size distribution is based on image analysis of 24,024 and 12,298 exosomes derived from control and patient samples, respectively. Panel (c) shows that the concentration with which the exosomes are deposited on the surface is nonuniform and resembles the coffee ring. We also observe that during the desiccation of the sample, the average size of deposited exosomes may change with spatial position. With reference to four areas in panel (c) delineated by diagonal lines, we see that the largest size is observed in the top left corner of the image and decreases towards its bottom right corner. This size segregation is quantified in panel (d).

Table 6.2: Manual and computer sizing of exosomes imaged by cryo-TEM (in nm).

	Control		Patient	
	Manual	Computer	Manual	Computer
Mean ± standard deviation	58.0±29.2	70.6±23.5	44.5±16.8	54.9±13.5
Median	54.6	68.4	44.7	54.9

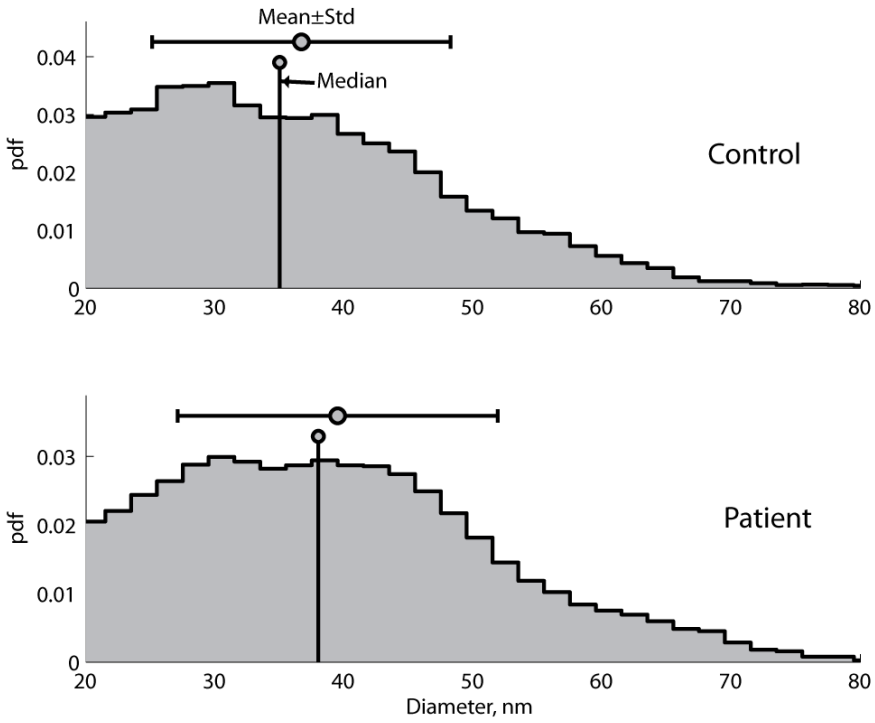

Figure 6.5: Results of the DMA sizing. Diameter less than 20 nm is excluded.

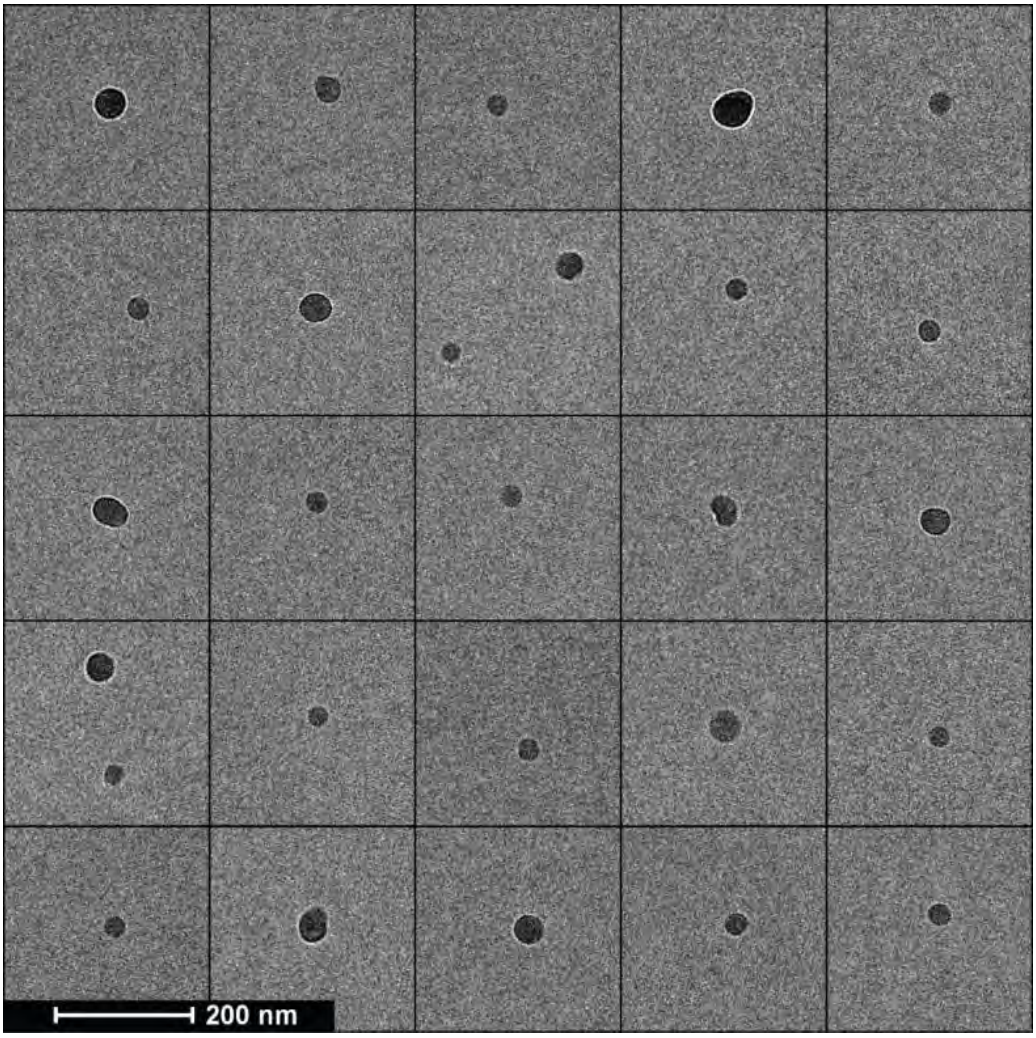

Figure 6.6: TEM images of exosomes desiccated in the aerosol and deposited from the gas phase on the TEM grid. In total, 194 exosomes were imaged. A bimodal particle size distribution (not shown) has peaks at ~30.0 nm and 42.4 nm corresponding to the +1 and +2 charge states, which have equal gas-phase electrical mobility within the DMA.

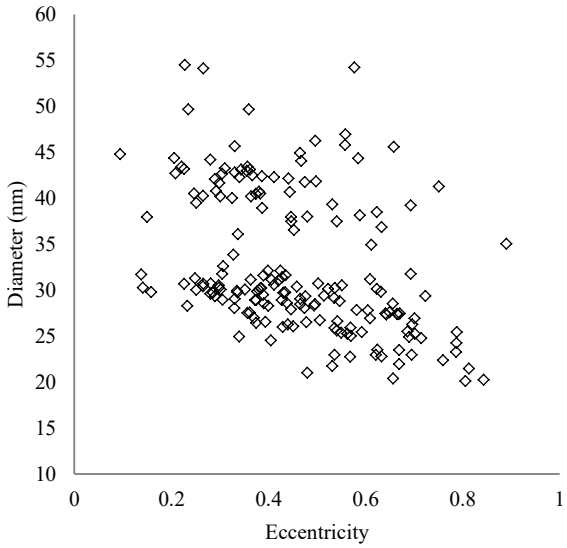

Figure 6.7: Size and eccentricity of DMA-deposited exosomes determined by computer analysis of TEM images.

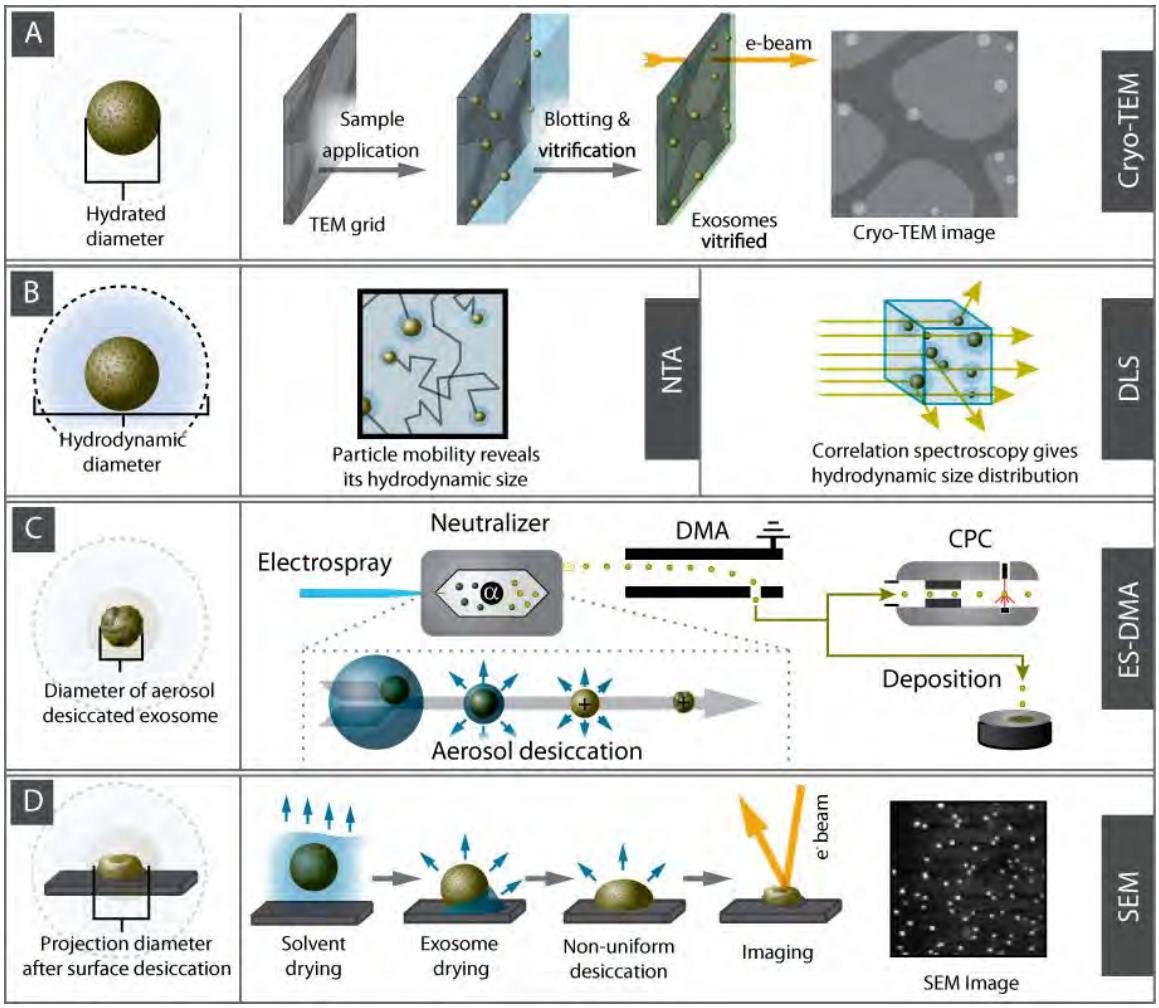

Figure 6.8: Size and shape of hydrated and desiccated exosomes and comparison of methods we used to characterize them. (A) Cryo-TEM images give two-dimensional projections of exosomes' geometry in their hydrated state. Close to circular projections indicate that exosomes are spherical particles. The diameter of the projections characterizes their size in hydrated spherical state. (B) NTA and DLS characterize the mobility of exosomes in the solution and estimate their hydrodynamic sizes, which were found to be substantially larger than their geometric sizes. (C) Electrospray with charge reduction generates desiccated nanoparticles primarily charged to ±1 or 0. A uniform drying front during aerosol desiccation preserves an approximately spherical shape of the exosomes. DMA separates particles based on their charge-to-size ratio. With predominantly identical +1 change of attracted particles, the separation is based on particles sizes. CPC counts particles one-by-one. Instead of directing particles for counting, particles of a selected size can be deposited on a substrate. (D) SEM is used to image exosomes desiccated on a surface. Surface desiccation proceeds with non-uniform drying front, which likely leads to a shape distortion and the formation of previously observed cup-shaped particles.

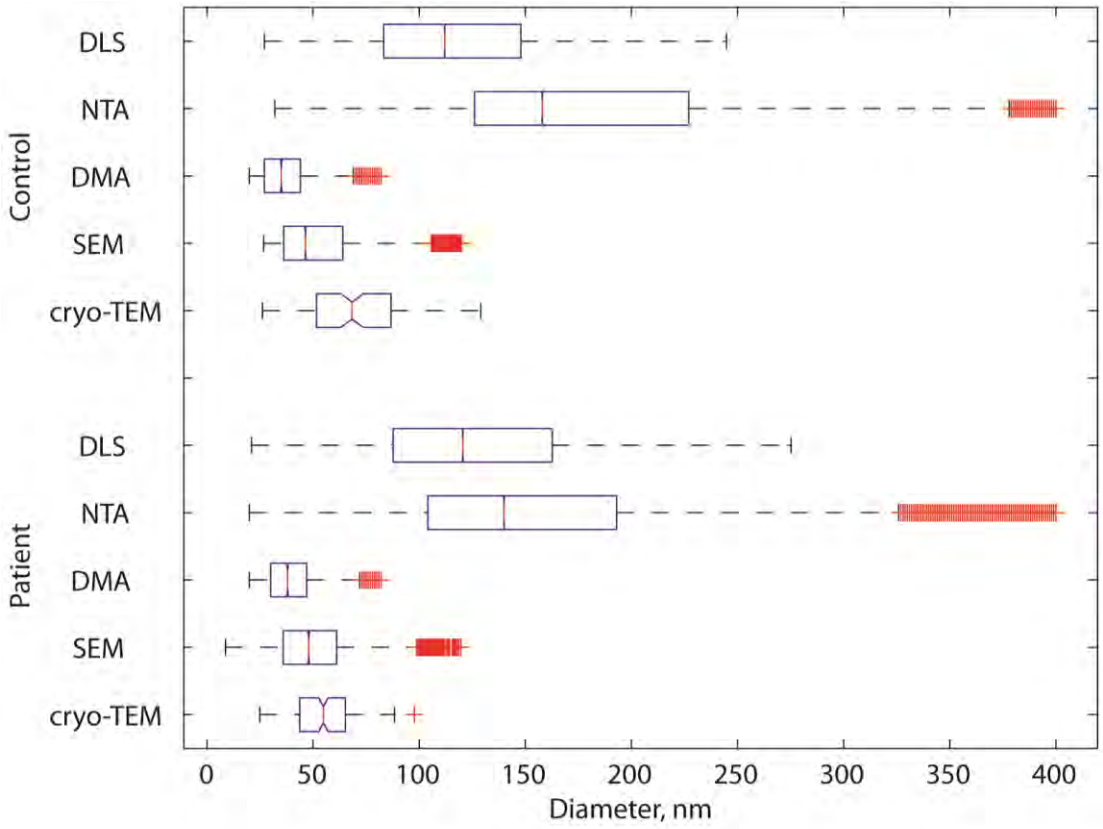

Figure 6.9: Summary of sizing result for control and patient samples by different methods. The box contains data between first (q_1) and third (q_3) quantiles; red line inside the box marks second quantile (median). The notch on the box is used to establish if size medians are significantly different. Assuming normal distribution, non-overlapping notches imply that true medians are different with 95% confidence. Comparison of medians is reasonably robust for other distributions and was tested to produce the same statistical conclusion under the assumption of log-normally distributed measurements of exosome sizes. Whiskers encompass data points larger than ($2.5q_3 - 1.5q_1$) and smaller than ($2.5q_1 - 1.5q_3$); all data points outside this range are marked with +.

Table 6.3: Size characterization of patient and control exosomes.

Size Measured		Method	Source	Size, nm Mean±Std	Size, nm Median	Size, nm 25%–75%	Eccentricity Mean±Std
Geometric	Hydrated	Cryo-TEM	Control	71±24	68	51–87	0.334±0.084
			Patient	55±14	55	44–65	0.290±0.085
	Surface desiccated	SEM	Control	52±21	46	36–64	0.493±0.313
			Patient	50±18	48	36–61	0.540±0.260
	Desiccated in aerosol	DMA	Control	37±12	35	27–44	–
			Patient	40±12	38	30–47	–
Hydrodynamic		NTA	Control	182±79	158	126–227	–
			Patient	157±72	140	104–193	–
		DLS	Control	119±47	112	83–148	–
			Patient	130±55	121	88–163	–

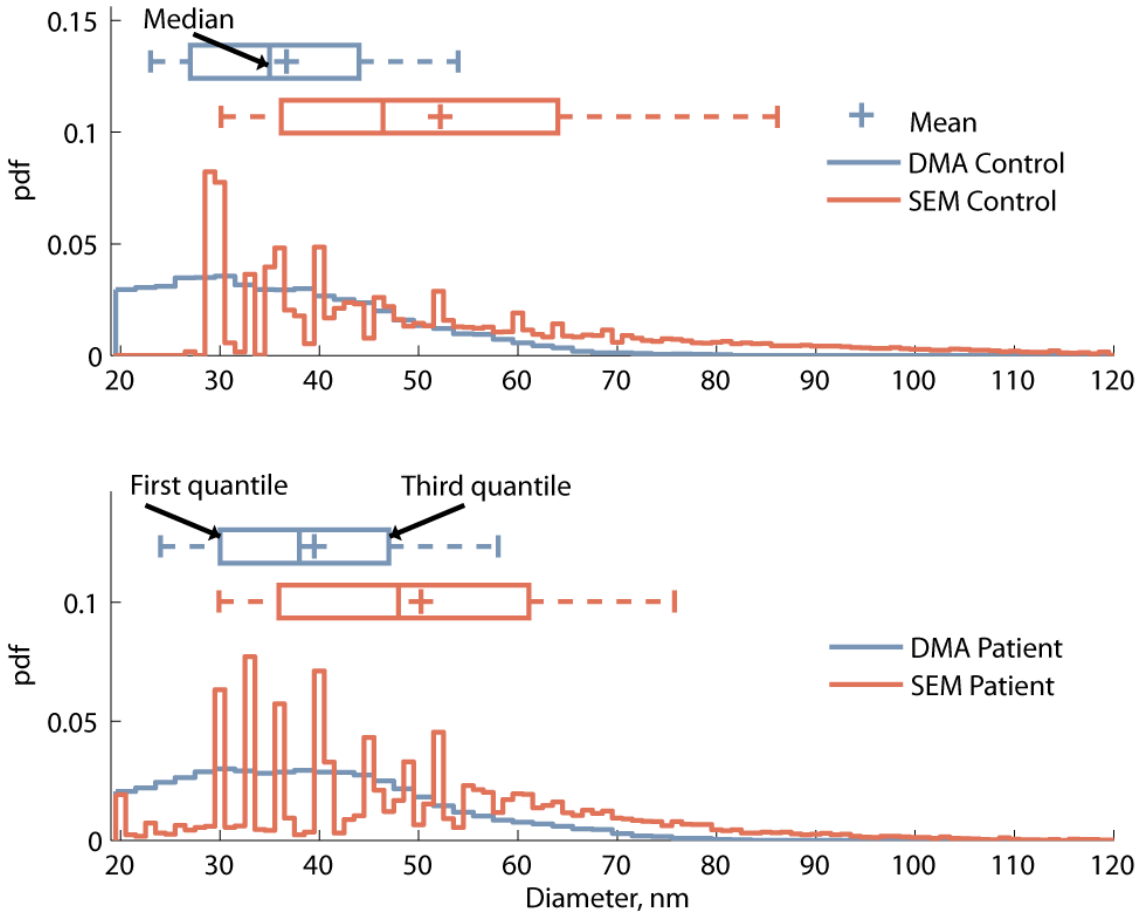

Figure 6.10: Size comparison of exosomes desiccated in aerosol and on the surface. Smaller DMA sizes reflect near spherical shape of exosomes uniformly desiccated in the gas phase. Surface drying prior to SEM imaging creates non-uniform drying front, which causes shape distortion (Figure 8D), and a larger diameter of the area occupied by surface desiccated exosomes.

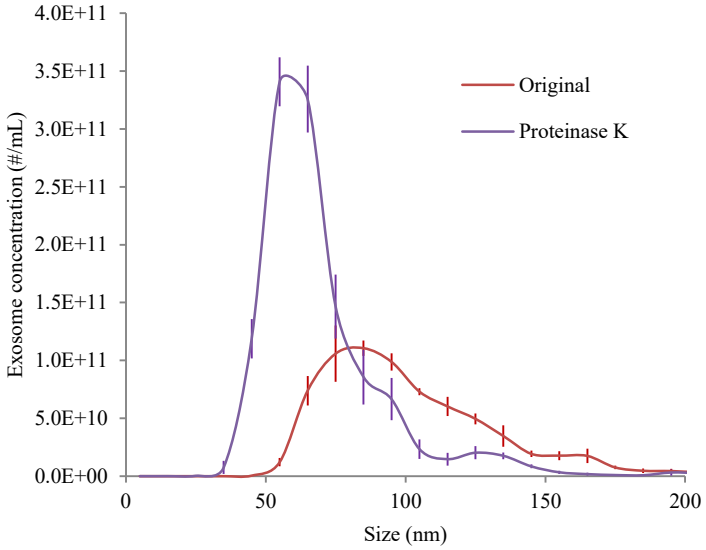

Figure 6.11: Size distribution comparison of exosomes extracted from MCF7 cell line in their original state and after exposed to proteinase K.

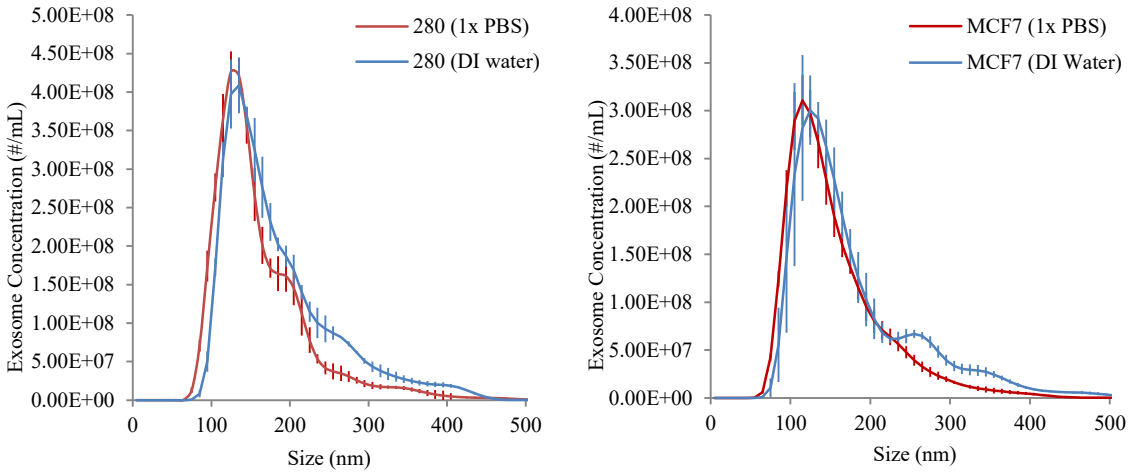

Figure 6.12: Comparison of NTA size results of exosomes diluted in PBS or DI water (a) NTA sizing of serum exosomes suspended in DI water and PBS. (b) NTA sizing of MCF7 cell line in DI water and PBS. The results are shown after equal dilution in the indicated liquid.

Table 6.4: NTA sizing of MCF7 exosomes in the solutions of low and physiological osmolarity. All size measurements give exosome diameter in nm, ± standard error.

	Serum exosomes		**MCF7 exosomes**	
	In DI water	In PBS	In DI water	In PBS
Concentration (#/mL$\times 10^{12}$ ± standard error)	4.27±0.14	3.97±0.15	3.32±0.35	3.05±0.18
Mean	179.9±1.7	157.8±1.3	177.3±11.2	151.3±1.9
Mode	137.1±7.1	127.5±4.7	127.4±7.7	117.5±3.6
Standard deviation of size distribution (relative to mean)	72.3±1.0	63±1.4	81.7±2.9	63.7±2.5
10^{th} percentile	106.3±0.7	94.3±1.0	98.8±7	86±0.1
50^{th} percentile	152.8±2.2	135.5±1.0	147±11.3	129.0±2.0
90^{th} percentile	276.7±5.9	225.9±3.5	286.5±16.2	230.1±5.9

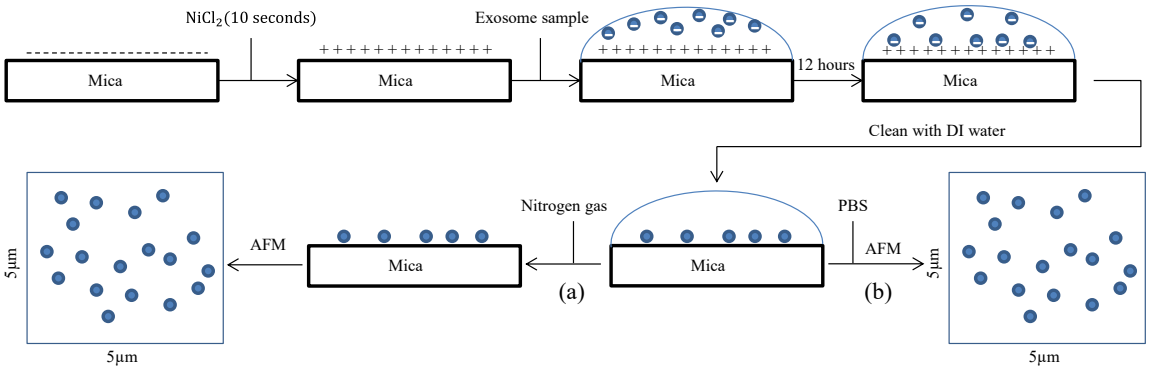

Figure 6.13: Schematic of the method used for AFM imaging. (a) Steps needed for imaging an exosome sample in air. (b) Steps needed for imaging an exosome sample in liquid.

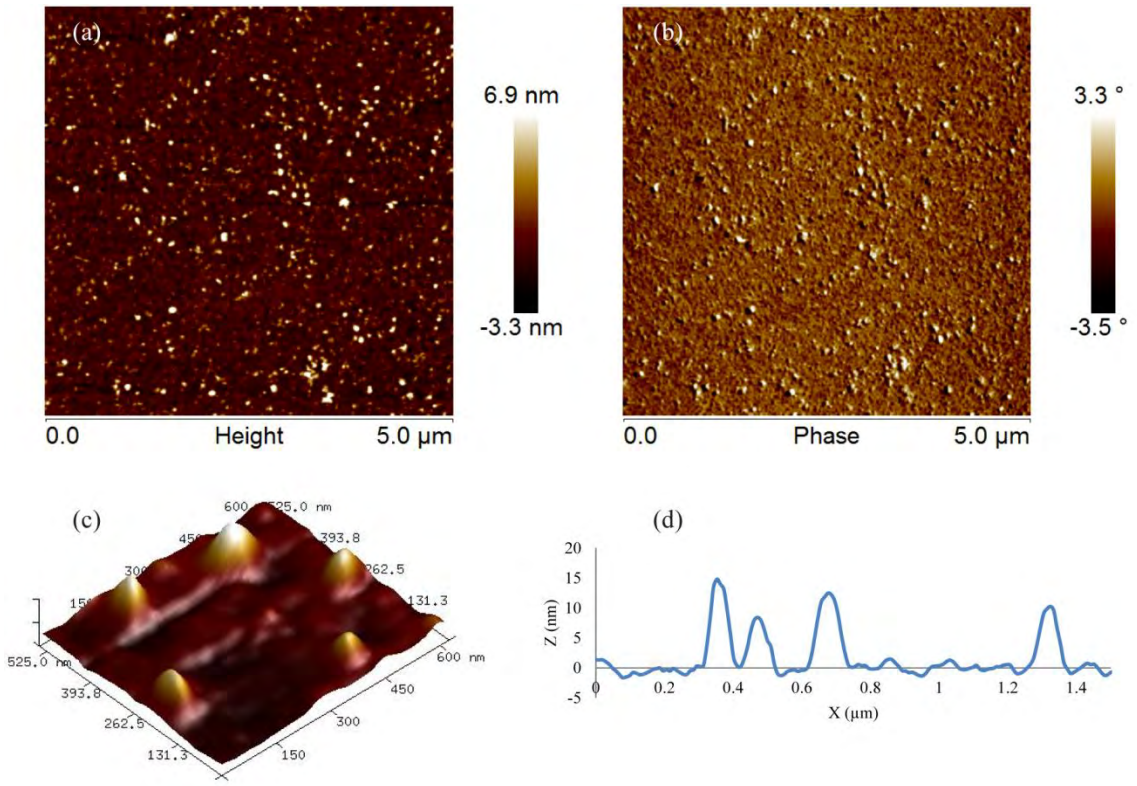

Figure 6.14: Morphology of exosomes in 1x PBS adsorbed to modified mica surface. (a) size (5x5 µm scan) (b) phase (5x5 µm scan) (c) 3 dimensional shape (d) section of an acquired image.

Table 6.5: AFM results presented in terms of exosome diameter, height and diameter of the approximating spherical shape. All measurements give size in nm ± standard error.

	Exosome sample source			
	Serum (1x PBS)	Serum (air)	MCF7 (1x PBS)	MCF7 (air)
Diameter	99±41	78±26	80±24	89±38
Height	3±1	2±1	6±3	5±1
Estimated sphere diameter	31	24	34	34

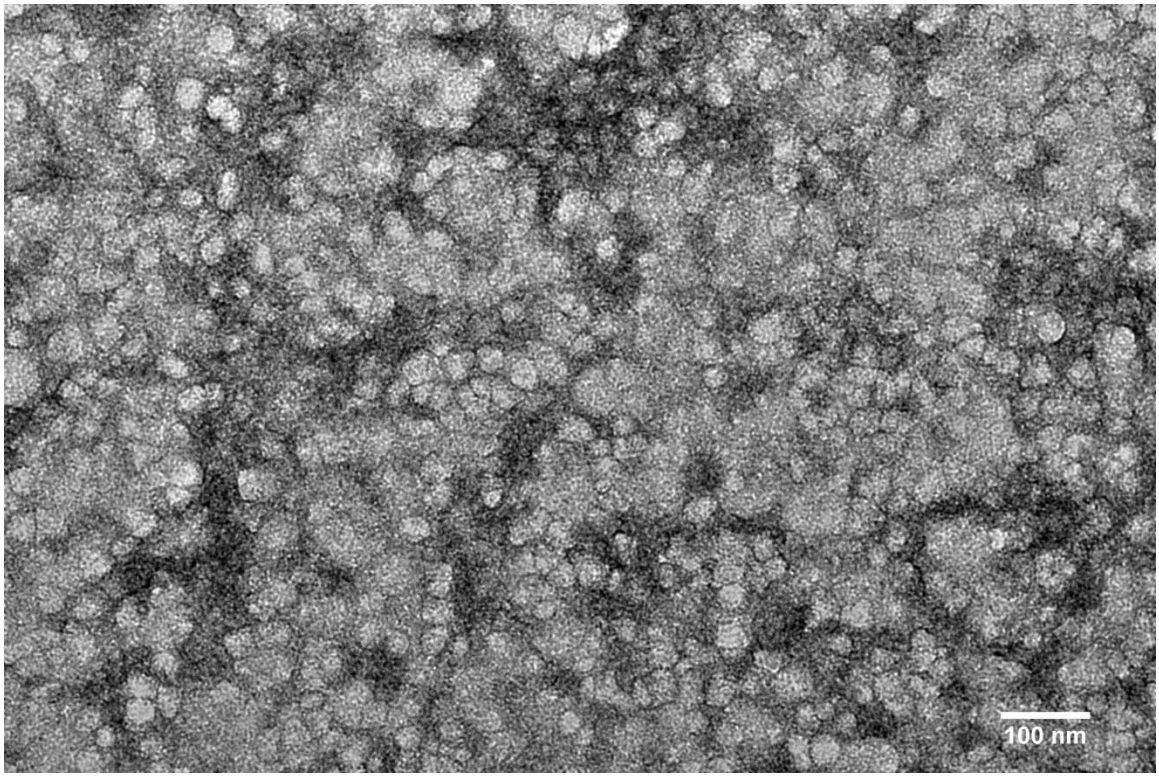

Figure 6.15: TEM image of a negatively stained MCF7 sample.

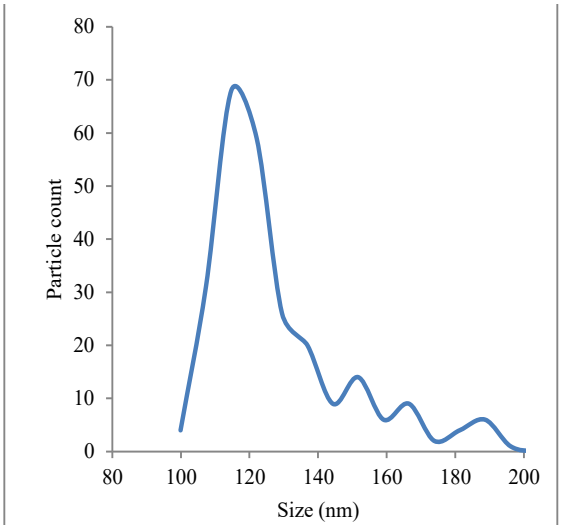

Figure 6.16: Size of exosome determined using tunable resistive pulse sensing (TRPS).

6.7 References

1. Thery, C., Zitvogel, L. & Amigorena, S. Exosomes: composition, biogenesis and function. *Nat. Rev. Immunol.* **2,** 569–579 (2002).

2. Trams, E. G., Lauter, C. J., Salem Jr., N. & Heine, U. Exfoliation of membrane ecto-enzymes in the form of micro-vesicles. *Biochim. Biophys. Acta.* **645,** 63–70 (1981).

3. Palma, J. *et al.* MicroRNAs are exported from malignant cells in customized particles. *Nucleic Acids Res.* **40,** 9125–38 (2012).

4. King, H. W., Michael, M. Z. & Gleadle, J. M. Hypoxic enhancement of exosome release by breast cancer cells. *BMC Cancer* **12,** 421 (2012).

5. Kucharzewska, P. & Belting, M. Emerging roles of extracellular vesicles in the adaptive response of tumour cells to microenvironmental stress. *J. Extracell. Vesicles* **2,** 20304 (2013).

6. Chevillet, J. R. *et al.* Quantitative and stoichiometric analysis of the microRNA content of exosomes. *Proc. Natl. Acad. Sci. U. S. A.* **111,** 14888–14893 (2014).

7. Gallo, A., Tandon, M., Alevizos, I. & Illei, G. G. The majority of microRNAs detectable in serum and saliva is concentrated in exosomes. *PLoS One* **7,** e30679 (2012).

8. Pucci, F. & Pittet, M. J. Molecular Pathways: tumor-derived microvesicles and their interactions with immune cells in vivo. *Clin. Cancer Res.* 1078–0432.CCR–12–0962– (2013). doi:10.1158/1078-0432.CCR-12-0962

9. Ge, R., Tan, E., Sharghi-Namini, S. & Asada, H. H. Exosomes in cancer microenvironment and beyond: have we overlooked these extracellular Messengers? *Cancer Microenviron.* **5,** 323–332 (2012).

10. Zhang, Y. *et al.* Secreted monocytic miR-150 enhances targeted endothelial cell migration. *Mol. Cell* **39,** 133–44 (2010).

11. Regev-Rudzki, N. *et al.* Cell-cell communication between malaria-infected red blood cells via exosome-like vesicles. *Cell* **153,** 1120–33 (2013).

12. Théry, C., Amigorena, S., Raposo, G. & Clayton, A. Isolation and characterization of exosomes from cell culture supernatants and biological fluids. *Curr. Protoc. Cell Biol.* **Chapter 3,** Unit 3.22 (2006).

13. Taylor, D. D., Zacharias, W. & Gercel-Taylor, C. Exosome isolation for proteomic analyses and RNA profiling. *Methods Mol. Biol.* **728,** 235–46 (2011).

14. Witwer, K. W. *et al.* Standardization of sample collection, isolation and analysis methods in extracellular vesicle research. *J. Extracell. Vesicles* **2,** 1–25 (2013).

15. Tauro, B. J. *et al.* Comparison of ultracentrifugation, density gradient separation, and immunoaffinity capture methods for isolating human colon cancer cell line LIM1863-derived exosomes. *Methods* **56,** 293–304 (2012).

16. Chen, C. *et al.* Microfluidic isolation and transcriptome analysis of serum microvesicles. *Lab Chip* **10,** 505–11 (2010).

17. Vlassov, A. V., Magdaleno, S., Setterquist, R. & Conrad, R. Exosomes: current knowledge of their composition, biological functions, and diagnostic and therapeutic potentials. *Biochim. Biophys. Acta* **1820,** 940–8 (2012).

18. Rekker, K. *et al.* Comparison of serum exosome isolation methods for microRNA profiling. *Clin. Biochem.* **47,** 135–8 (2014).

19. Alvarez, M. L., Khosroheidari, M., Kanchi Ravi, R. & DiStefano, J. K. Comparison of protein, microRNA, and mRNA yields using different methods of urinary exosome isolation for the discovery of kidney disease biomarkers. *Kidney Int.* **82,** 1024–32 (2012).

20. György, B. *et al.* Membrane vesicles, current state-of-the-art: emerging role of extracellular vesicles. *Cell. Mol. Life Sci.* **68,** 2667–88 (2011).

21. Van der Pol, E., Coumans, F., Varga, Z., Krumrey, M. & Nieuwland, R. Innovation in detection of microparticles and exosomes. *J. Thromb. Haemost.* **11 Suppl 1,** 36–45 (2013).

22. Van der Pol, E. *et al.* Optical and non-optical methods for detection and characterization of microparticles and exosomes. *J. Thromb. Haemost.* **8,** 2596–607 (2010).

23. Thery, C. *et al.* Membrane vesicles as conveyors of immune responses. *Nat. Rev. Immunol.* **9,** 581–593 (2009).

24. Bacher, G. *et al.* Charge-reduced nano electrospray ionization combined with differential mobility analysis of peptides, proteins, glycoproteins, noncovalent protein complexes and viruses. *J. Mass Spectrom.* **36,** 1038–52 (2001).

25. Caulfield, M. P. *et al.* Direct determination of lipoprotein particle sizes and concentrations by ion mobility analysis. *Clin. Chem.* **54,** 1307–16 (2008).

26. Guha, S., Pease, L. F., Brorson, K. a, Tarlov, M. J. & Zachariah, M. R. Evaluation of electrospray differential mobility analysis for virus particle analysis: potential applications for biomanufacturing. *J. Virol. Methods* **178,** 201–8 (2011).

27. Guha, S., Li, M., Tarlov, M. J. & Zachariah, M. R. Electrospray-differential mobility analysis of bionanoparticles. *Trends Biotechnol.* **30,** 291–300 (2012).

28. Pease, L. F. *et al.* Packing and size determination of colloidal nanoclusters. *Langmuir* **26,** 11384–90 (2010).

29. Wiedensohler, A. An approximation of the bipolar charge distribution for particles in the submicron size range. *J. Aerosol Sci.* **19,** 387–389 (1988).

30. Flagan, R. C. Differential mobility analysis of aerosols: a tutorial. *KONA Powder Part. J.* **26,** 254–268 (2008).

31. Lattin, J. R., Belnap, D. M. & Pitt, W. G. Formation of eLiposomes as a drug delivery vehicle. *Colloids Surf. B. Biointerfaces* **89,** 93–100 (2012).

32. Deegan, R. D. *et al.* Capillary flow as the cause of ring stains from dried liquid drops. *Nature* **389,** 827–829 (1997).

33. Nguyen, T. A. H., Hampton, M. A. & Nguyen, A. V. Evaporation of nanoparticle droplets on smooth hydrophobic surfaces: the inner coffee ring deposits. *J. Phys. Chem. C* **117,** 4707–4716 (2013).

34. Yunker, P. J., Still, T., Lohr, M. A. & Yodh, A. G. Suppression of the coffee-ring effect by shape-dependent capillary interactions. *Nature* **476,** 308–11 (2011).

35. Still, T., Yunker, P. J. & Yodh, A. G. Surfactant-induced Marangoni eddies alter the coffee-rings of evaporating colloidal drops. *Langmuir* **28,** 4984–8 (2012).

36. Kaufman, S. L., Skogen, J. W., Dorman, F. D., Zarrin, F. & Lewis, K. C. Macromolecule analysis based on electrophoretic mobility in air: globular proteins. *Anal. Chem.* **68,** 1895–904 (1996).

37. György, B. *et al.* Detection and isolation of cell-derived microparticles are compromised by protein complexes resulting from shared biophysical parameters. *Blood* **117,** e39–48 (2011).

38. Van Deun, J. *et al.* The impact of disparate isolation methods for extracellular vesicles on downstream RNA profiling. *J. Extracell. Vesicles* **3,** (2014).

39. Caradec, J. *et al.* Reproducibility and efficiency of serum-derived exosome extraction methods. *Clin. Biochem.* **47,** 1286–92 (2014).

40. Jeppesen, D. K. *et al.* Comparative analysis of discrete exosome fractions obtained by differential centrifugation. *J. Extracell. Vesicles* **3,** 25011 (2014).

41. Mathivanan, S. & Simpson, R. J. ExoCarta: A compendium of exosomal proteins and RNA. *Proteomics* **9,** 4997–5000 (2009).

42. Laulagnier, K. *et al.* Characterization of exosome subpopulations from RBL-2H3 cells using fluorescent lipids. *Blood Cells. Mol. Dis.* **35,** 116–21 (2005).

43. Bobrie, A., Colombo, M., Krumeich, S., Raposo, G. & Théry, C. Diverse subpopulations of vesicles secreted by different intracellular mechanisms are present in exosome preparations obtained by differential ultracentrifugation. *J. Extracell. Vesicles* **1,** 18397 (2012).

44. Yellon, D. M. & Davidson, S. M. Exosomes: nanoparticles involved in cardioprotection? *Circ. Res.* **114,** 325–32 (2014).

45. Kobayashi, M. *et al.* Ovarian cancer cell invasiveness is associated with discordant exosomal sequestration of Let-7 miRNA and miR-200. *J. Transl. Med.* **12,** 4 (2014).

46. Petersen, K. E. *et al.* A review of exosome separation techniques and characterization of B16-F10 mouse melanoma exosomes with AF4-UV-MALS-DLS-TEM. *Anal. Bioanal. Chem.* **406,** 7855–66 (2014).

47. Sharma, S. *et al.* Structural-mechanical characterization of nanoparticle exosomes in human saliva, using correlative AFM, FESEM, and force spectroscopy. *ACS Nano* **4,** 1921–6 (2010).

48. Sharma, S., Gillespie, B. M., Palanisamy, V. & Gimzewski, J. K. Quantitative nanostructural and single-molecule force spectroscopy biomolecular analysis of human-saliva-derived exosomes. *Langmuir* **27,** 14394–400 (2011).

49. Sharma, S., Das, K., Woo, J. & Gimzewski, J. K. Nanofilaments on glioblastoma exosomes revealed by peak force microscopy. *J. R. Soc. Interface* **11,** 20131150 (2014).

50. Conde-Vancells, J. *et al.* Characterization and comprehensive proteome profiling of exosomes secreted by hepatocytes. *J. Proteome Res.* **7,** 5157–5166 (2008).

51. Zhou, Y. *et al.* Exosomes released by human umbilical cord mesenchymal stem cells protect against cisplatin-induced renal oxidative stress and apoptosis in vivo and in vitro. *Stem Cell Res. Ther.* **4,** 34 (2013).

52. Coleman, B. M., Hanssen, E., Lawson, V. a & Hill, A. F. Prion-infected cells regulate the release of exosomes with distinct ultrastructural features. *FASEB J.* **26,** 4160–73 (2012).

53. Van der Pol, E., Böing, A. N., Harrison, P., Sturk, A. & Nieuwland, R. Classification, functions, and clinical relevance of extracellular vesicles. *Pharmacol. Rev.* **64,** 676–705 (2012).

54. Momen-Heravi, F. *et al.* Impact of biofluid viscosity on size and sedimentation efficiency of the isolated microvesicles. *Front. Physiol.* **3,** 162 (2012).

55. Sokolova, V. *et al.* Characterisation of exosomes derived from human cells by nanoparticle tracking analysis and scanning electron microscopy. *Colloids Surf. B. Biointerfaces* **87,** 146–50 (2011).

56. Tscharnuter, W. T. in *Encycl. Anal. Chem.* (Meyers, R. A.) 1–16 John Wiley & Sons, Ltd, 2006. doi:10.1002/9780470027318.a1512

57. Besseling, N. A. M. Theory of hydration forces between surfaces. *Langmuir* **13,** 2113–2122 (1997).

58. He, L., Hu, Y., Wang, M. & Yin, Y. Determination of solvation layer thickness by a magnetophotonic approach. *ACS Nano* **6,** 4196–202 (2012).

59. Tathireddy, P., Choi, Y.-H. & Skliar, M. Particle AC electrokinetics in planar interdigitated microelectrode geometry. *J. Electrostat.* **66,** 609–619 (2008).

60. Iyer, S., Gaikwad, R. M., Subba-Rao, V., Woodworth, C. D. & Sokolov, I. Atomic force microscopy detects differences in the surface brush of normal and cancerous cells. *Nat. Nanotechnol.* **4,** 389–93 (2009).

61. Frank, J. Single-particle imaging of macromolecules by cryo-electron microscopy. *Annu. Rev. Biophys. Biomol. Struct.* **31,** 303–19 (2002).

62. Oh, E. *et al.* Cellular uptake and fate of PEGylated gold nanoparticles is dependent on both cell-penetration peptides and particle size. *ACS Nano* **5,** 6434–48 (2011).

63. Shoemaker, S. D. & Vanderlick, T. K. Stress-induced leakage from phospholipid vesicles: effect of membrane composition. *Ind. Eng. Chem. Res.* **41,** 324–329 (2002).

64. Hull, M. C., Sauer, D. B. & Hovis, J. S. Influence of lipid chemistry on the osmotic response of cell membranes: effect of non-bilayer forming lipids. *J. Phys. Chem. B* **108,** 15890–15895 (2004).

65. Taupin, C., Dvolaitzky, M. & Sauterey, C. Osmotic pressure induced pores in phospholipid vesicles. *Biochemistry* **14,** 4771–4775 (1975).

66. Hardij, J. *et al.* Characterisation of tissue factor-bearing extracellular vesicles with AFM: comparison of air-tapping-mode AFM and liquid Peak Force AFM. *J. Extracell. Vesicles* **2,** 1–9 (2013).

67. Palanisamy, V. *et al.* Nanostructural and transcriptomic analyses of human saliva derived exosomes. *PLoS One* **5,** e8577 (2010).

68. Bezanilla, M., Manne, S., Laney, D. E., Lyubchenko, Y. L. & Hansma, H. G. Adsorption of DNA to mica, silylated mica, and minerals: characterization by atomic force microscopy. *Langmuir* **11,** 655–659 (1995).

69. Hsueh, C., Chen, H., Gimzewski, J. K., Reed, J. & Abdel-Fattah, T. M. Localized nanoscopic surface measurements of nickel-modified mica for single-molecule DNA sequence sampling. *ACS Appl. Mater. Interfaces* **2,** 3249–3256 (2010).

70. Hardij, J. *et al.* Characterisation of tissue factor-bearing extracellular vesicles with AFM: comparison of air-tapping-mode AFM and liquid peak force AFM. *J. Extracell. Vesicles* **2,** 1–9 (2013).

71. Lavialle, F. *et al.* Nanovesicles released by Dictyostelium cells: A potential carrier for drug delivery. *Int. J. Pharm.* **380,** 206–215 (2009).

72. Varga, Z. *et al.* Towards traceable size determination of extracellular vesicles. *J. Extracell. Vesicles* **3,** 23298 (2014).

73. Dragovic, R. a. *et al.* Sizing and phenotyping of cellular vesicles using Nanoparticle Tracking Analysis. *Nanomedicine* **7,** 780–8 (2011).

74. Momen-Heravi, F. *et al.* Alternative methods for characterization of extracellular vesicles. *Front. Physiol.* **3,** 354 (2012).

75. Hood, J. L., Pan, H., Lanza, G. M. & Wickline, S. A. Paracrine induction of endothelium by tumor exosomes. *Lab. Invest.* **89,** 1317–28 (2009).

76. Atay, S., Gercel-Taylor, C., Kesimer, M. & Taylor, D. D. Morphologic and proteomic characterization of exosomes released by cultured extravillous trophoblast cells. *Exp. Cell Res.* **317,** 1192–202 (2011).

77. Tian, T., Wang, Y., Wang, H., Zhu, Z. & Xiao, Z. Visualizing of the cellular uptake and intracellular trafficking of exosomes by live-cell microscopy. *J. Cell. Biochem.* **111,** 488–96 (2010).

78. Tatischeff, I., Larquet, E., Falcón-Pérez, J. M., Turpin, P.-Y. & Kruglik, S. G. Fast characterisation of cell-derived extracellular vesicles by nanoparticles tracking analysis, cryo-electron microscopy, and Raman tweezers microspectroscopy. *J. Extracell. Vesicles* **1,** 19179 (2012).

79. Wahlgren, J., Karlson, T. D. L., Glader, P., Telemo, E. & Valadi, H. Activated human T cells secrete exosomes that participate in IL-2 mediated immune response signaling. *PLoS One* **7,** e49723 (2012).

80. Ng, Y. H. *et al.* Endometrial exosomes/microvesicles in the uterine microenvironment: a new paradigm for embryo-endometrial cross talk at implantation. *PLoS One* **8,** e58502 (2013).

CHAPTER 7

DETERMINATION OF EXOSOME CONCENTRATION AND MASS BASED ON QUARTZ CRYSTAL MICROBALANCE

7.1 Abstract

Exosomes are endogenous nanoparticles secreted by cells into blood circulation. Characterizing their properties, especially concentration and mass, is difficult and limited only to a few methods. Here we introduce a new method taking advantage of quartz crystal microbalance (QCM) that can be used for quantifying exosomes and provide measure of exosome mass. The method presented is simple and inexpensive, using a QCM instrument and software for data analysis. We apply this method for exosomes secreted by cell lines modeling breast and prostate cancer. Limitations of this method will also be presented.

7.2 Introduction

Exosomes are stable membrane-bound nanoparticles (20-120nm) that are released into the circulation by many cell types, including cancer cells.[1,2] These small vesicles are produced by inward budding of the late endosomal membrane of the multivesicular bodies (MVBs)[3], and contain membrane and cargo (nucleic acids and proteins) derived from the cell of origin.[4,5] Although the physiological function(s) of exosomes are not well

understood, they have been shown to be important in immune response and may play a role in short and long-range intercellular signaling.[6,7] A potential mechanism for this cell communication is through exosomes fusing with target cells and releasing their contents. It is known that exosomes carry small noncoding RNAs, including microRNAs (miRNAs) that vary in abundance in the blood between normal individuals and those with cancer.[8–10] Also, it has been shown that relevant cancer miRNAs are enriched in the serum exosome pellet.[11] Furthermore, breast cancer cells in vitro increase their release of exosomes and contain miRNAs specific to their environment (e.g., hypoxia).[12] Taken together, we can make a reasonable assumption that different tumor subtypes (aggressive vs. indolent) will release exosomes with different biophysical properties and different amounts of small RNAs. Such difference in content may affect the mass of exosomes – knowledge of which will be useful for differentiating those secreted by cancerous cells from those secreted by normal cells. However, at this time there are only a few methods that can estimate concentration and density or mass of exosomes. The most common method for density measurement is a sucrose gradient, where exosomes are layered on top of a sucrose gradient with set density range and centrifuged for a period of time. Fractions are then collected and sucrose gradient is measured.[13] Also, the only available methods for measuring concentration are the nanoparticle tracking analysis (NTA), ELISA and tunable resistive pulse sensing (TRPS) requiring expensive instrumentation or kits.

The QCM method started with a thorough investigation done by Jacques and Pierre Curie in 1880, and later quartz piezoelectricity pioneered by Raleigh in 1885.[14–16] QCM is made of a thin, perfectly cut quartz disk with electrodes plated on it. Applying

external electrical potential to the piezoelectric material produces internal mechanical stress. A resonant oscillation is achieved by using a quartz crystal in the oscillation circuit where the electric and mechanical oscillations are near the fundamental frequency of the crystal.[14] The change in the frequency was found to be directly proportional to the mass change on the crystal, described by the Sauerbrey equation that was developed by Günter Sauerbrey in 1959:

$$\Delta f = -C_f \Delta m \quad (1)$$

where Δf is change in frequency, Δm is change in mass per unit area and C_f is the sensitivity factor of the crystal.[17] This method includes a broad range of applications such as gas phase detection,[18] immunosensors,[19] DNA biosensors[20] and deposition.[14,21] However, to our knowledge, no one has applied QCM for measuring concentration and mass of exosomes as well as other extracellular vesicles (EV). This report will introduce the QCM for exosome sample analysis and application for exosomes isolated from specific cell lines.

7.3 Proposed Method and Implementation

The method for estimating concentration of exosomes and mass will consist of two main steps. First, the mass of a sample containing only $10^6 - 10^{10}$ exosomes will be measured using an instrument that will allow working with small sample volumes. The second step is determination, if unknown, of the number of exosomes and size in the sample. Combining information about concentration and mass change will allow estimating the exosome concentration and average exosome mass.

QCM will be used for the first step of the method due to its high sensitivity to mass change. A small volume ($5\mu L$) of the sample will be pipetted to the center of the

quartz crystal and the frequency of oscillation will be recorded including the time before the sample is introduced and the time after the solvent (e.g., water) evaporates completely, leaving only the particles on the quartz crystal surface. To determine exosome concentration and size in a sample, nanoparticle tracking analysis (NTA) method will be used although other methods such as surface tensiometry presented in Chapter 5 may also be applied.

7.4 Materials and Instrumentation

7.4.1 Cell Line Preparation and Exosome Extraction

MDA-MB-231, MCF7 and MCF10a breast cancer cell lines, PC3, PCS, LNCap and 22Rv1 human prostate cancer cell lines prior to cell culture were stored in liquid nitrogen. For cell culture the cell line was thawed and plated on 150 mm plates. Table 7.1 provides the growth media used for each cell line. Once the cells settled down, the media was changed (approximately 24 hours after plating). The plate was then split at 1:10 ratio and 10 plates were cultured. Each plate contained 20 mL of media. Media from 9 of these plates (180mL) was harvested and pooled. Media was then split into 30 ml/tube and centrifuged at 3000×g for 15 minutes. Each supernatant was then transferred to a new sterile 50 mL tube. Exosomes were isolated by using the ExoQuick TC technique (System Bioschiences, Mountain View, CA, USA). In short, 6mL of ExoQuick TC reagent was added to each 30 mL supernatant and left for overnight incubation at 4°C. On the next day, the mixture was centrifuged at 1500×g for 30 minutes at room temperature. After centrifugation, the exosomes would appear as a beige pellet. The obtained pellet was resuspended in 2mM ammonium acetate (AA). The resuspended exosomes were then separated into 100 µL aliquots and stored in 1 mL tubes at -80°C until use.

7.4.2 Scanning Electron Microscopy (SEM)

Prior to SEM imaging, the PC3 exosomes sample was diluted 1:10 in 2mM AA. A glass slide was gently cleaned with nitrogen gas and placed on the specimen stage of the SEM (FEI NanoNova 630 High Resolution SEM). Five microliters of the sample was then placed on the glass slide and allowed to dry at room temperature and pressure. The sample was then imaged at 0.98 Torr using a low vacuum secondary electron detector at magnifications in the 15,000-55,000× range. The acquired 1024×943 pixel images were then observed using MATLAB software (MathWorks, Natick, MA).

7.4.3 Concentration and Size Measurement

Concentration was determined using the Nanosight instrument (model LM10; Salisbury, United Kingdom) by illuminating the sample with a 40 mW violet laser (405 nm wavelength), capturing the light scatted by exosomes with a high-sensitivity sCMOS camera (OrcaFlash2.8, Hamamatsu C11440), and analyzing the results using the software provided by the manufacturer (Nanosight Version 2.3). The minimal track length was set to auto, and blur size was set to 1 pass, gain set to 1, brightness to 12, and detection threshold set to 5. The viscosity of 2mM AA was assumed to be equal to viscosity of water which depends on temperature and was adjusted automatically based on the temperature measurements. Temperature of the cell was measured manually and remained at 20°C with a maximum of 0.1 degree fluctuation throughout the nanoparticle tracking. Viscosity of water at these temperatures is nearly constant and equal to 1cP. Prior to analysis, the exosome samples were diluted to appropriate concentration (e.g., 1:100 and 1:1,000) in 2mM AA and allowed to equilibrate to room temperature (20°C). Samples were analyzed within 5 minutes of the initial dilution. Using a 1mL sterile

syringe, each sample was injected into the test cell. Approximately 30-100 particles were observed in the field of view and the typical concentration was approximately $1 - 10 \times 10^8$ particles/mL for each measurement. Five 60-second videos were recorded for each sample at 24.99 frames per second with 11.25 millisecond shutter speed and analyzed using NTA software with the described settings. Each video consisted of more than 1400 frames and the total of completed particle tracks for each 60-second video was more than 20,000. The video data characterizing hydrodynamic mobility of particles in the field of view were analyzed with the NTA software which reported the exosome concentration, size distribution, its mode, mean and the standard deviation. Each sample was measured once using five videos with updated sample volume in the NTA cell.

7.4.4 Centrifugal Field Flow Fractionation

CF2000 (Postnova, Salt Lake City, UT) was used for fractionating the MCF7 sample. A solution consisting of 2mM ammonium acetate with 0.0025% w/v Tween 20 was used as the channel fluid. The flow rate was set to 1 ml/min and rotation speed to 4900rpm. The relaxation time was set to 7 minutes and detection set to record at 219nm wavelength. Injection of 10uL of the original MCF7 sample with no dilution into CF2000 injection port was then done. The first fraction of MCF7 was collected at 1.5 minutes after relaxation and collection finished at 4 minutes. All other fractions were collected approximately every minute leading to a total of 9 fractions.

7.4.5 Quartz Crystal Microbalance

A 5 MHz QCM200 (Stanford Research Systems, Inc, Sunnyvale, CA) instrument was used for mass measurements. Specific for 5 MHz frequency, polished quartz crystals

with 1 inch diameter and titanium/gold electrodes were used for the QCM instrument. The RS-232 port was connected to a desktop computer (HP Z400 Work-station) and LabVIEW stand-alone application was used for data acquisition. The compensation switch of QCM200 was set to hold and ten-turn dial to 8.0 (dry operation setting). Prior to an experiment the frequency of oscillation was given 15 minutes to equilibrate.

7.5 Results

The concentration and hydrodynamic size distribution of exosomes in solution were analyzed by nanoparticle tracking analysis. Figure 7.1 and Table 7.1 show the size distribution and concentration of exosomes from each cell line as well as mode and mean with standard deviation. Figure 7.2a shows an example frequency change due to introduction of a 5μL sessile drop containing exosomes. During the initial evaporation of the sessile drop, no significant change in frequency was observed. However, after a longer time (~1,500 seconds) there was a distinct drop in frequency. This is due to the negative correlation between mass per unit area and decreasing surface area of the drop over time. After complete evaporation of the solvent, the frequency would clearly reach a steady state. The steady state values appeared consistent from run to run with a maximum of 5% error.

Figure 7.2b shows an image of a dry sample obtained using an optical microscope. This image was processed using a custom MATLAB code to find the initial boundary of the sessile drop. To determine the location of exosomes and how they were distributed after complete evaporation of the solvent, the procedure was repeated using a glass slide on which the sessile drop was placed and allowed to dry. SEM images were then obtained from the bottom to the top edge of the dry sample. It was observed that

exosomes are present at the edge of the sample (Figure 7.2c). Aggregated particles or ammonium acetate crystals were also observed (Figure 7.2c and d) but they were not present in all locations. Nonuniform particle concentration in multiple locations was noticed (Figure 7.2d, e and f), as well as some locations where no particles were present. This asymmetry can be due to the roughness of the glass slide as well as size difference of the particles, leading to the coffee ring effect.[22] Overall the exosomes appeared to be distributed throughout the entire area initially occupied by the sessile drop which was concluded based on observing all SEM images obtained from the bottom edge to the top edge of the dry sample. This observation allowed us to assume an even exosome distribution in the area initially occupied by the solvent. Therefore, by converting the frequency given by the QCM to mass per unit area (using the Sauerbrey equation), one can calculate the mass of the sample because the area is known. This assumption appeared to be relevant and Sauerbrey equation applicable, since the effect of dry sample relative to the dry quartz surface is analyzed. Figure 7.3 shows a linear correlation between frequency change and exosome number present in the volume used. The (0,0) intercept was expected when no background particles or contaminants were present, but in this case it is not observed due to the presence of residue that was independently measured to contribute ~15-20 Hz decrease in frequency. This linear relation now allows one to measure exosome concentration in a sample.

Exosomes in this study are considered to be spherical, which is a good assumption as it was previously shown by us (Chapter 6) and others.[23–25] The average volume occupied by each exosome was estimated by using mode size data obtained by NTA and determined to be $8.39 \pm 2.3 \times 10^{-22}$ m^3. Combining mass data obtained from QCM with

exosome number obtained from NTA, the average mass for each particle in all cell lines was determined to be 3.24 femtograms (fg) with 0.37 fg standard deviation (Table 7.3). The QCM and NTA result leads to an unrealistic density estimate of exosomes, $3.43\ \mathrm{g/mL}$, if mode size from each cell line is applied while the average density is expected to be ~1.25 g/mL as reported by others.[13,26–28] On the other hand, the use of mean size of exosomes from all cell lines (183 nm) instead of mode size leads to volume of $3.72 \pm 2.5 \times 10^{-21}\ \mathrm{m}^3$ and gives a density estimation closer to the one expected, 1.30 g/mL. Third-order sensitivity of exosome volume estimation to exosome diameter has a substantial impact on the density result. Density estimation method by applying the complete size distribution data along with mass obtained using QCM will be further investigated in the future.

This technique was also tested by conducting cFFF on 10 μL of undiluted MCF7 sample. Fractions were collected and analyzed using NTA (Figure 7.4). Out of them, 6 fractions were chosen for QCM analysis. The presence of Tween 20 contributed significantly to the frequency change by a constant value of ~285 Hz; data was adjusted accordingly. Figure 7.5 shows the results obtained from QCM and it can be clearly seen that mass increases with elution time as expected with cFFF. The average mass of exosomes in fractions determined by QCM was calculated to be 1.95±0.59 fg.

7.6 Discussion

Determination of exosome concentration and mass by using the QCM method was studied and presented in this work due to the limited number of methods available today. The method takes advantage of the high QCM sensitivity to mass change, and the correlation of the frequency change to the change in mass per area. Exosome

concentration was shown to be easily estimated by the presented correlation. The average mass of exosomes in a sample was also determined by applying area that is occupied by the sample on the quartz crystal. Although the average mass results for each cell line appeared close, there was still some variability. It was shown that exosomes were distributed throughout the area occupied by the introduced sessile drop including its boundary. However, nonuniformity of the number of exosomes per unit area was clearly observed (Figure 7.2d, e and f) on the microscale, which could contribute to error of the average mass estimation.

The standard deviation that was observed for concentration and mass estimation can also be due to the error of the 10 μL pipette that was used to manually place the sample volume on the quartz crystal. Since this variation in volume will introduce a different number of particles for each measurement, the reported mass determined by the QCM will vary in proportion to the change in volume. This can be avoided by automating introduction of the sample with high precision. The error could also be contributed by the area estimation due to the difficulty of accurately defining the boundary of the dry drop. A factor that could also contribute to the error of estimation is the presence of background particles – surfactants or salts as shown in Figure 7.7. The nonuniformity of their distribution and difficulty in reproducing such nonuniformity from run to run will make their contribution to frequency change difficult to include in the calculation of mass that was of interest. An adjustment had to be made when working with ammonium acetate and Tween 20, but because their contribution to frequency change was consistent it was more easily accounted for. Like most methods, the presented method has a limit of

detection (LOD). The minimum number of exosomes that QCM200 can measure was estimated to be 1.5×10^6 exosomes, when they occupy $7 - 8\ \mathrm{mm}^2$ area.

Shape of exosomes is more complex than standard polystyrene beads or gold nanoparticles. It is has been shown that the structure of exosomes is in the form of nanovesicles, enclosed by a double membrane having surface decorations with various cargo molecules present inside. For instance, it was determined by us (see Chapter 6) that the hydrodynamic size of exosomes is substantially larger than geometric size due to surface decorations. Such differences bring more complexity for exosome density estimation.

7.7 Conclusion

A novel method for determining concentration and average exosome mass of exosomes in a sample was presented. The technique takes advantage of high sensitivity to a mass change by QCM. The procedure is simple and involves an exosome sample introduced to the surface of the quartz crystal, followed by determination of the difference in its frequency before introduction of the sample and after the solvent present in the sample evaporates, leaving only exosomes on the surface of the crystal. The QCM results were then coupled with concentration of exosomes in the sample which allowed determination of their mass. Future work will be focused on introducing an algorithm of determining exosome density by using their mass and size.

Table 7.1: Medium used for each cell line.

Cell line	LNCap	22Rv1	PC3	PCS	MCF7	MCF10a	MDA-MB-231
Medium	RPMI-1650 Medium	RPMI-1650 Medium	F-12K Medium	SteCM Medium	Eagle's Minimum Essential Medium	Mammary Epithelial Cell Growth (MEGM)	Leibovitz's L15 Medium (grown without CO2)

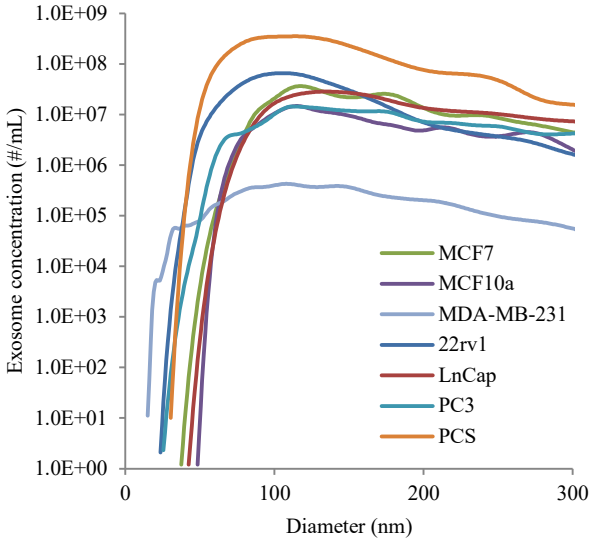

Figure 7.1: Concentration and size distribution obtained using NTA.

Table 7.2: Size data and original concentration obtained using NTA.

Sample	MCF10a	MCF7	MDA-MB 231	LNCap	22Rv1	PC3	PCS
Mode (nm)	115	117	123	135	106	115	102
Mean (nm)	205	183	147	251	131	220	146
SD (nm)	117	84	74	141	63	119	77
NTA Original Conc (#/mL)	1.81E11 ±1.06E10	4.01E11 ±7.79E9	6.31E9 ±3.47E9	4.99E11 ±4.81E10	5.72E11 ±3.55E10	3.66E11 ±1.46E10	2.23E12 ±1.19E11

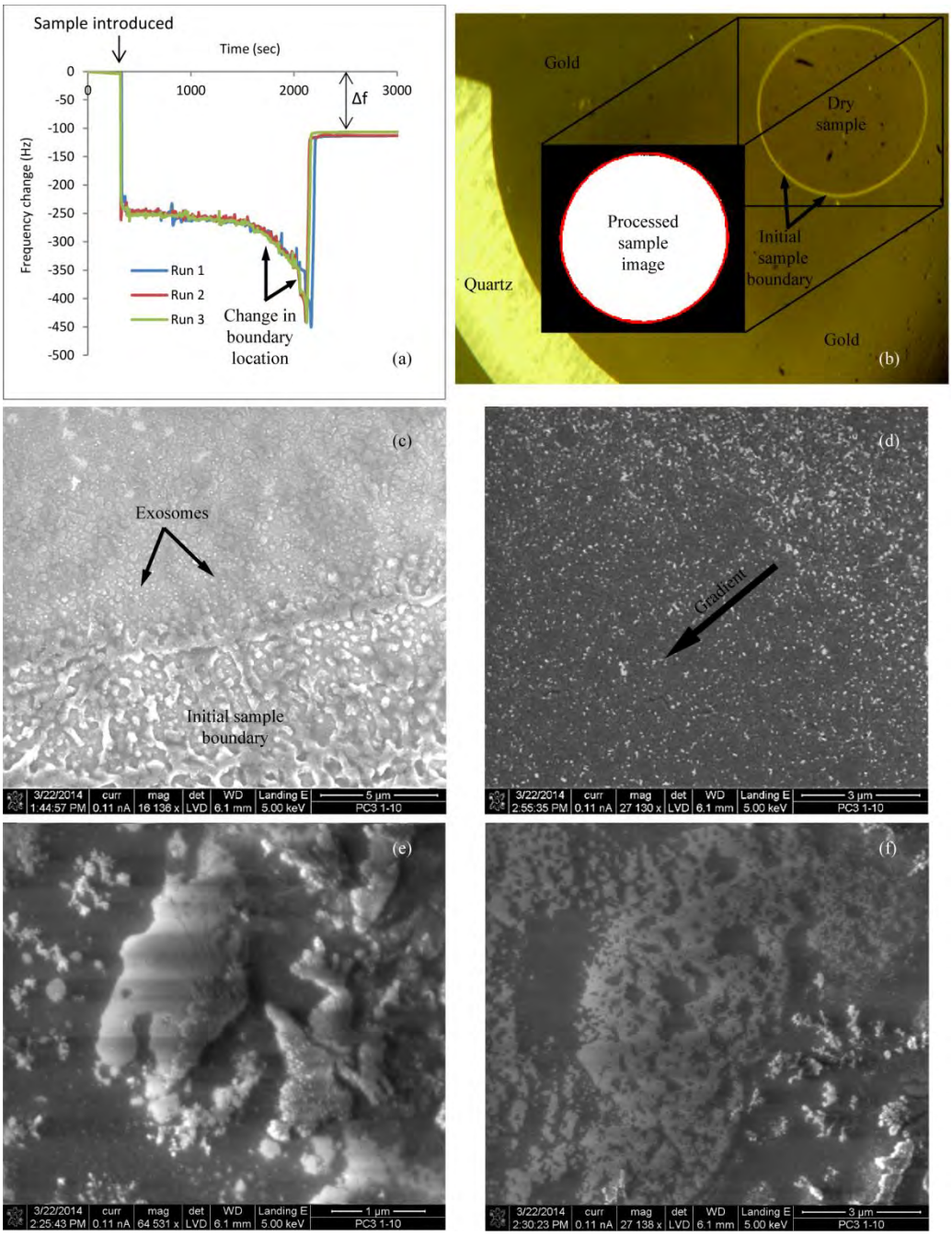

Figure 7.2: Example of QCM results and images of the analyzed sample (a) QCM data for one of the cell line samples repeated after 3 repetitions; (b) an evaporated sessile drop with a clearly defined boundary (c) SEM image showing the edge of the dried drop and the presence of the PC3 exosomes (d, e and f) SEM images showing nonuniformity of PC3 exosomes and presence of aggregates.

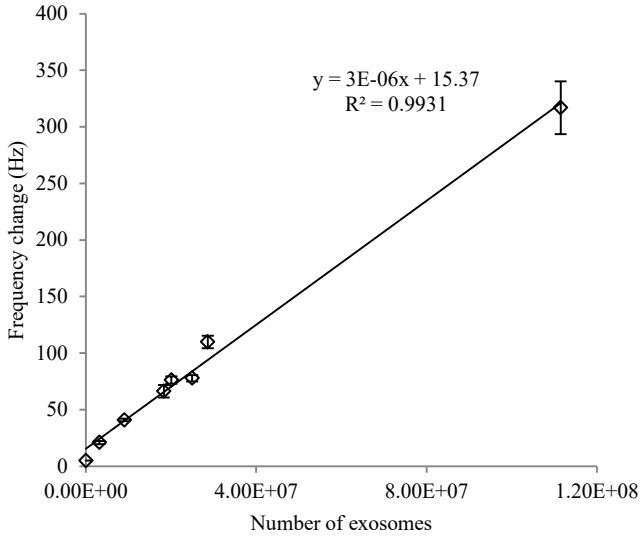

Figure 7.3: Correlation of frequency change to the number of exosomes.

Table 7.3: Exosome mass estimated by QCM combined with NTA.

Sample	MCF10a	MCF7	MDA-MB 231	LNCap	22Rv1	PC3	PCS
Average Mass (fg)	3.11	3.29	2.77	3.04	3.97	3.16	3.33
STD (fg)	0.0895	0.228	0.463	0.174	0.113	0.0764	0.164

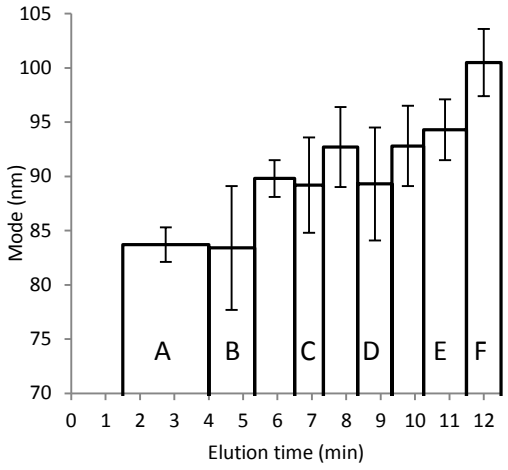

Figure 7.4: Mode diameter of each MCF7 fraction obtained using cFFF. A-F represent fractions used for QCM analysis.

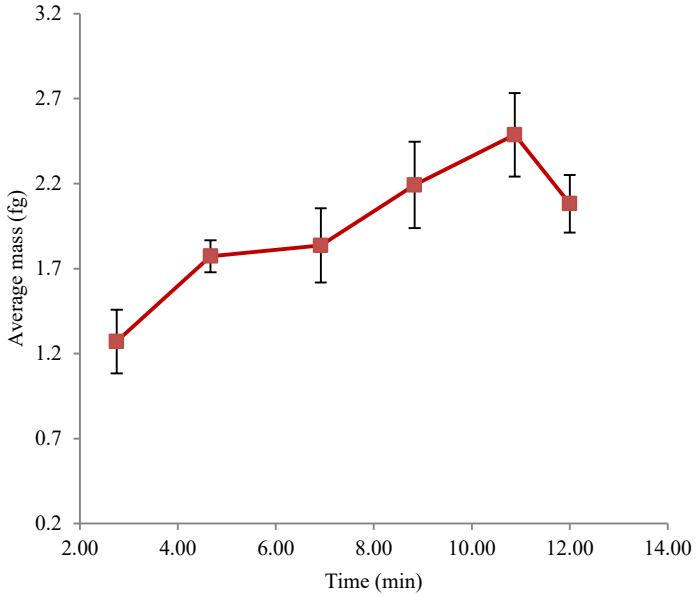

Figure 7.5: Centrifugal Field-Flow Fractionation (cFFF) of the MCF7 sample with exosome mass estimated by the QCM method.

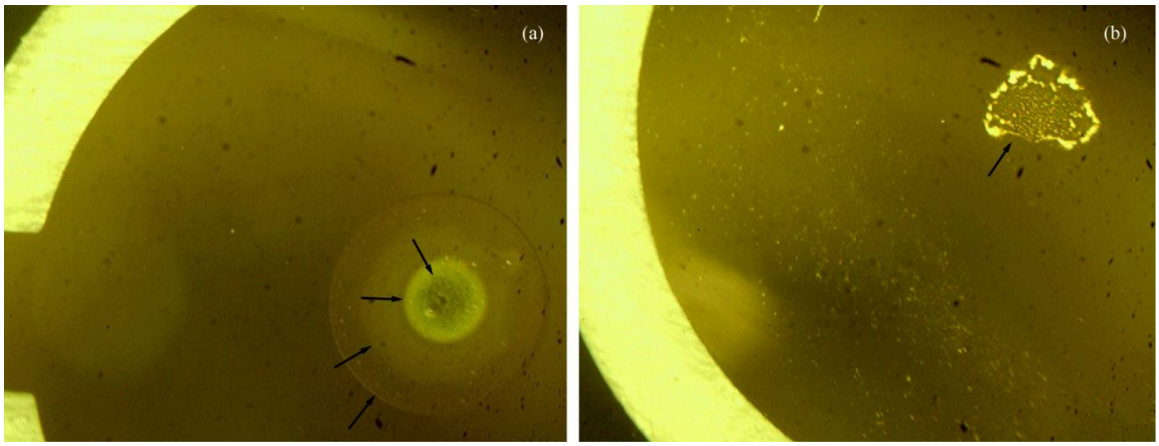

Figure 7.6: Limitations of QCM application for mass and density measurement. (a) Nonuniformity of a dry sample (b) Salt crystals after evaporation of the solvent.

7.8 References

1. Trams, E. G., Lauter, C. J., Salem Jr., N. & Heine, U. Exfoliation of membrane ecto-enzymes in the form of micro-vesicles. *Biochim. Biophys. Acta.* **645,** 63–70 (1981).

2. Palma, J. *et al.* MicroRNAs are exported from malignant cells in customized particles. *Nucleic Acids Res.* **40,** 9125–38 (2012).

3. Thery, C., Zitvogel, L. & Amigorena, S. Exosomes: composition, biogenesis and function. *Nat. Rev. Immunol.* **2,** 569–579 (2002).

4. Kharaziha, P., Ceder, S., Li, Q. & Panaretakis, T. Tumor cell-derived exosomes: a message in a bottle. *Biochim. Biophys. Acta.* **1826,** 103–111 (2012).

5. Raposo, G. & Stoorvogel, W. Extracellular vesicles: exosomes, microvesicles, and friends. *J. Cell Biol.* **200,** 373–383 (2013).

6. Pucci, F. & Pittet, M. J. Molecular pathways: Tumor-derived microvesicles and their interactions with immune cells in vivo. *Clin. Cancer Res.* **19,** 2598–604 (2013).

7. Ge, R., Tan, E., Sharghi-Namini, S. & Asada, H. H. Exosomes in cancer microenvironment and beyond: have we overlooked these extracellular messengers? *Cancer Microenviron.* **5,** 323–332 (2012).

8. Chen, X. *et al.* Characterization of microRNAs in serum: a novel class of biomarkers for diagnosis of cancer and other diseases. *Cell Res.* **18,** 997–1006 (2008).

9. Taylor, D. D. & Gercel-Taylor, C. MicroRNA signatures of tumor-derived exosomes as diagnostic biomarkers of ovarian cancer. *Gynecol. Oncol.* **110,** 13–21 (2008).

10. Lee, Y. S. & Dutta, A. MicroRNAs in cancer. *Annu. Rev. Pathol.* **4,** 199–227 (2009).

11. Gallo, A., Tandon, M., Alevizos, I. & Illei, G. G. The majority of microRNAs detectable in serum and saliva is concentrated in exosomes. *PLoS One* **7,** e30679 (2012).

12. King, H. W., Michael, M. Z. & Gleadle, J. M. Hypoxic enhancement of exosome release by breast cancer cells. *BMC Cancer* **12,** 421 (2012).

13. Skogberg, G. *et al.* Characterization of human thymic exosomes. *PLoS One* **8,** e67554 (2013).

14. O'Sullivan, C. K. & Guilbault, G. G. Commercial quartz crystal microbalances - Theory and applications. *Biosens. Bioelectron.* **14,** 663–670 (1999).

15. Curie, J. & Curie, P. An oscillating quartz crystal mass detector. *Comp. Rend.* **91,** 294–297 (1880).

16. Raleigh, L. Quartz piezoelectric. *Pacy DJ Vac. 1960* **9,** 261–270 (1885).

17. Sauerbrey, G. The use of quartz oscillators for weighing thin layers and for microweighing. *Zeitschrift fuer Phys.* **155,** 206–222 (1959).

18. King, W. H. Piezoelectric Sorption Detector. *Anal. Chem.* **36,** 1735–1739 (1964).

19. Shons, A., Dorman, F. & Najarian, J. The piezoelectric quartz immunosensor. *J. Biomed. Mater. Res.* **6,** 565–570 (1972).

20. Fawcett, N. C., Evans, J. A., Chen, L. C., Drozda, K. A. & Flowers, N. A quartz crystal detector for DNA. *Anal. Lett.* **21,** 1099–1110 (1988).

21. Guleryuz, H. *et al.* Deposition of silica nanoparticles onto alumina measured by optical reflectometry and quartz crystal microbalance with dissipation techniques. *Colloids Surfaces A Physicochem. Eng. Asp.* **443,** 384–390 (2014).

22. Deegan, R. D. *et al.* Capillary flow as the cause of ring stains from dried liquid drops. *Nature* **389,** 827–829 (1997).

23. Conde-Vancells, J. *et al.* Characterization and comprehensive proteome profiling of exosomes secreted by hepatocytes. *J. Proteome Res.* **7,** 5157–5166 (2008).

24. Zhou, Y. *et al.* Exosomes released by human umbilical cord mesenchymal stem cells protect against cisplatin-induced renal oxidative stress and apoptosis in vivo and in vitro. *Stem Cell Res. Ther.* **4,** 34 (2013).

25. Coleman, B. M., Hanssen, E., Lawson, V. a & Hill, A. F. Prion-infected cells regulate the release of exosomes with distinct ultrastructural features. *FASEB J.* **26,** 4160–73 (2012).

26. Théry, C. *et al.* Proteomic analysis of dendritic cell-derived exosomes: a secreted subcellular compartment distinct from apoptotic vesicles. *J. Immunol.* **166,** 7309–7318 (2001).

27. Miranda, K. C. *et al.* Nucleic acids within urinary exosomes/microvesicles are potential biomarkers for renal disease. *Kidney Int.* **78,** 191–199 (2010).

28. Mignot, G., Roux, S., Thery, C., Ségura, E. & Zitvogel, L. Prospects for exosomes in immunotherapy of cancer. *J. Cell. Mol. Med.* **10,** 376–388 (2006).

CHAPTER 8

CONCLUSIONS AND FUTURE DIRECTIONS

8.1 Conclusions

The motivation behind this research was to explore existing methods and develop new methods to determine physical and chemical properties of analytes, more specifically short-chain molecules and biological nanoparticles. This is important since only a handful of methods are available to characterize analytes with a size range of only 0.1-100 nm. For example, determining the concentration of the biological nanoparticles called exosomes in a sample is already a difficult task, and only a few expensive commercial instruments are available for such analysis. Estimating the stability or half-life of nanobubbles that are used as contrast agents or vehicles for drug delivery in medicine is also limited by conventional methods which are time consuming and often inaccurate. Having new methods available to do such measurements will allow research in these areas to progress.

To better understand behavior of nanobubbles in liquid (e.g., coalescence), a study was conducted by looking at surface tension dynamics when water is exposed to air with perfluorocarbon vapors, simulating interface of a single nanobubble and was presented in Chapter 2. We found a substantial decrease in surface tension of water when perfluoropentane and perfluorohexane vapors are present in air. A similar effect was seen

when methanol was used for the pendant drop. For the first time, linear correlations between surface tension of a fluid in which perfluorocarbons are immiscible (e.g., methanol) and concentration of perfluorocarbons in the gas phase were found. This technique can be used to estimate stability of microbubbles in liquid by monitoring surface tension and finding surfactants that can decrease surface tension by the requisite amount.

The linear relation found in Chapter 2 was expanded and applied to solve a different problem presented in Chapter 3. Determining diffusion coefficients of vapors in air is a difficult task, having a limited amount of methods most of which are time consuming and expensive. Applying the linear relation between surface tension and concentration of the solute in the vapor, presented previously, allows determination of the diffusion coefficient of that solute by using the dynamic surface tension data. The pendant drop surface tension, which is affected by the change in solute concentration in the vapor phase at that location, is used as the complementary fluid (sensor). Although such linear relation should only be applied to nearly immiscible fluids, we were able to expand the presented method to compounds that are miscible in the complementary fluid by accounting for solute absorption. This method can be applied not only to solutes in the vapor phase but also in the liquid, such as short-chain molecules and nanoparticles. A further investigation of the effect of perfluorocarbon vapor on surface tension of water was conducted and the results presented in Chapter 4. Exposure of a pendant drop of water to perfluorocarbon vapor for long periods of time led to formation of a lens at the water drop apex. To understand this phenomenon further, a set of experiments were conducted. It was confirmed that solubility of perfluorocarbons in water is negligible as

no signal was observed when using Fourier transform infrared spectroscopy (FT-IR). An experiment was then conducted to model a thin layer of water exposed to perfluoropentane vapor. We were able to show that perfluoropentane does adsorb to the water surface by using a sensitive to mass change quartz crystal microbalance (QCM) method. This was not surprising as previous studies reported hydrocarbon adsorption to the water surface. Formation of the lens is most likely due to formation of multiple layers of perfluoropentane on the water surface which later accumulate at the apex simply due to gravity and weak molecular interactions.

The second half of the dissertation started with a continuation of dynamic surface tension application but for biological nanoparticles and their surface activity was studied in Chapter 5. Surprisingly, exosomes were found to be surface active, showing a significant decrease in surface tension with time. Exosomes appeared to act as surfactants and a linear relation between the logarithm of exosome concentration and surface tension was found for a specific concentration range. This can be applied for easily measuring the concentration of exosomes in a given sample. In addition, it has potential to estimate the average size of the particles. Furthermore, we found that exosome adsorption to the interface is thermodynamically favored and is irreversible. This finding provides better understanding of how exosomes adsorb to a cell's surface, fuse and release their content into the cytoplasm. Development of a microfluidic device that will miniaturize the presented method and quickly determine exosome concentration in a sample is foreseeable in the future.

Size determination methods of extracellular vesicles (exosomes) were then explored in Chapter 6. Until now, no group has compared the advantages and

disadvantages of each existing method, as well as noticed useful information other than size that each method can provide. It was found that hydrodynamic size of exosomes is substantially larger than geometric size and is the main reason for variability in exosome sizes reported by others. Such difference is most likely due to exosome composition that includes various surface decorations such as proteins and glycolipids. We were able to show this by shaving surface proteins with proteinase K and conducting size measurements before and after. Since exosomes are elastic, imaging them dry or wet also makes a significant difference in the size distribution results. Even factors such as fixation or drying exosomes on a surface instead of analyzing them in the gas phase or frozen also impact size and shape results. Finally, it was clearly shown that the natural shape of exosomes is spherical and not cup shaped as reported by other authors previously. In addition to existing methods, a novel AFM method for imaging exosomes was developed and presented. Our results now provide a critical reference on what size determination method is the most appropriate for the given study.

Finally, Chapter 7 was focused on the development of another method that can measure concentration and average mass of exosomes. The motivation for this project was the availability of only one reliable method, sucrose density gradient, that can estimate density of exosomes. Quartz crystal microbalance (QCM) coupled with nanoparticle tracking analysis (NTA) was implemented for such measurements. It was shown that exosome concentration can be easily determined by simply measuring the mass of the sample. The developed method was also applied to determine mass of exosome sample fractions obtained using centrifugal field-flow fractionation (cFFF). The correlation between mass and elution time was as expected. Such a method can not only

be used for exosomes but also to measure the concentration and mass of other types of nanoparticles (e.g., gold and polymers).

8.2 Future Directions

Development of new methods to determine biophysical properties of nanoparticles is a difficult but important task in order for areas such as nanotechnology and medicine to move forward. Currently, there are only a few methods available to characterize molecules and nanosized particles, and each method has significant drawbacks. Careful analysis of available methods as well as development of new methods presented in Chapters 2-7 contribute to the progression of these fields. However, there are still many tasks that must be done in future research:

1) Develop a method able to quickly and easily determine size and shape of exosomes in a liquid;
2) Miniaturize the surface tension method for monitoring concentration of exosomes and determine average size;
3) Make a more complete and accurate model of microbubbles by inclusion of surfactants and scaling down from mm to micro/nanometer scale;
4) Apply the developed method for measuring diffusion coefficients of solutes in the gas phase to molecules and nanoparticles in the liquid phase.

Accomplishing these tasks will take this from ideas to products. Such products (e.g., exosome sensors) will allow progression of other research areas as well as improve the fields of medicine and nanotechnology.